Interface Effects in Antiferromagnetic-Ferromagnetic Hybrid Systems

Dissertation zur Erlangung des Grades
"Doktor der Naturwissenschaften"
am Fachbereich Physik, Mathematik und Informatik
der Johannes Gutenberg-Universität
in Mainz

Tobias Marcel Wagner
geb. in Wiesbaden
Mainz, der 12. November 2024

JOHANNES GUTENBERG
UNIVERSITÄT MAINZ

Berichterstatter: Removed due to data privacy.

Removed due to data privacy.

Anhänge gemäß Prüfungsordnung

I hereby declare that the thesis submitted is my own unaided work. All direct or indirect sources used are acknowledged as references. The thesis, in whole or in part, has never been submitted to any other examination committee that is able to admit a doctoral degree.

Ich versichere, dass ich meine Dissertation selbstständig verfasst und keine anderen als die angegebenen Quellen und Hilfsmittel benutzt sowie Zitate kenntlich gemacht habe. Die Doktorarbeit ist weder abschnittsweise, noch in der vorliegender Form bei einer anderen Prüfungsbehörde zur Erlangung eines Doktorgrades eingereicht worden.

Mainz, der 12. November 2024

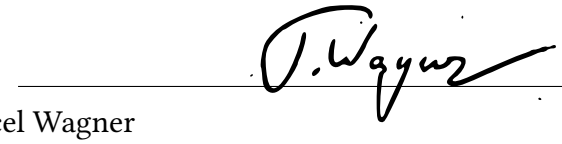

Tobias Marcel Wagner
INSPIRE Group
Institut für Physik – FB 08

Staudingerweg 7
Johannes Gutenberg University
D-55128 Mainz

Acknowledgements

Removed due to data privacy.

Tobias

12. November 2024

Abstract

Recent advances in artificial intelligence algorithms have led to a widespread adoption of artificial intelligence-driven applications in industry and research. However, increasingly powerful algorithms require large amounts of energy. In combination with a proliferation of use cases the feasibility of energy production and cost to meet demands in the future is in doubt.

In an attempt to sustainably meet the needs of developing artificial intelligence systems and reduce power consumption, the emulation of biological systems is extended from the software level to the hardware level. Because the physical description of magnetization reversal aligns with the non-linear dynamics of neural networks, magnetic materials are suitable for a material-based approach.

Spintronics, which utilizes both the spin and charge degree of freedom of electrons, shows great promise for overcoming the limitations of conventional semiconductor circuits. Antiferromagnets possess ultra-fast dynamics, optimal downscaling and increased stability. The roadblock that hinders their utilization is the challenging readout of their magnetic state. The next step is to combine the known manipulability of ferromagnets with the advantageous properties of antiferromagnets in antiferromagnetic-ferromagnetic hybrid systems. This thesis focusses on studying the interface effects on magnetization ground state and dynamics in antiferromagnetic-ferromagnetic bilayers.

Because magnetic phenomena root in quantum mechanics, while their manifestation also takes place in classical physics, their study requires a multiscale approach. In this thesis we use phenomenological descriptions and numerical methods. The computational approaches employed throughout this thesis are micromagnetic and atomistic spin dynamics simulations.

First, it is demonstrated that ferromagnetic vortex textures can be imprinted into

the adjacent antiferromagnetic layer via interface exchange coupling. In particular, the antiferromagnetic Néel vector can be controlled via the ferromagnetic state, thereby providing read-out options. In this collaborative project, the role of the author was to lead and execute the theoretical modeling of the experimental data and coordinate the exchange between theory and experiment. A model was provided, which describes the stability of the imprinted antiferromagnetic vortex state. Both a phenomenological model and micromagnetic simulations succeed at supporting experimental results from the NiO(111)-Fe (110) (6 nm) model system. Hence, it was shown that NiO-Fe hybrid systems are suitable for hosting magnetic vortices as fundamental logical units for computing that benefit from antiferromagnetic properties, while, at the same time, the ferromagnetic layer facilitates the readout.

Furthermore, the coupled magnetization statics and dynamics of Mn_2Au-$Ni_{80}Fe_{20}$ (Py, Permalloy) thin film hybrids are explored as part of the German Research Foundation (DFG) project - TRR 173 Spin + X: spin in its collective environment (project B12 and A05). The author's task was to coordinate the exchange with the collaborators, model experimental results that were obtained within the collaboration and extract the observed interface exchange coupling strength from the experimental data. A phenomenological model reveals that interface exchange coupling in Mn_2Au-Py causes an imprinting of the antiferromagnetic domain texture on the ferromagnetic layer. This alignment, that enables the readout of the antiferromagnetic state, is shown not only analytically, but also using atomistic spin simulations. Interface exchange coupling leads to coupled spin dynamics in Mn_2Au-Py and a frequency enhancement and a frequency splitting of the ferromagnetic resonance mode in the Py. Such dynamic effects have their origin in the exceptionally strong interface exchange coupling, which so far was only observed in the material system presented here. Experimental data from ferromagnetic resonance and Brillouin light scattering experiments on Mn_2Au-Py thin films agrees well with the theoretical model. Finally, atomistic spin dynamics simulations demonstrate that domain wall motion with a high domain wall velocity can be initiated by acting on the ferromagnetic magnetization with magnetic fields. In summary it was shown that by combining antiferromagnets and ferromagnets in hybrid systems, the dynamics of the ferromagnet can be significantly enhanced through the presence of the antiferromagnet while retaining their conventional accessibility. Additionally the emergence of a split mode shows that the antiferromagnet's intrinsic properties have been successfully synergized with the ferromagnetic dynamics.

Kurzzusammenfassung

Auf Grund aktueller Fortschritte wird künstliche Intelligenz in einer Vielzahl von Anwendungsmöglichkeiten, sowohl in der Wirtschaft, als auch in der Forschung, eingesetzt. Die zunehmende Leistungsfähigkeit der künstlichen Intelligenz geht jedoch mit einem ansteigenden Energiebedarf der Rechnerinfrastruktur einher. In Kombination führen der steigende Energieverbrauch und die stark zunehmende Anzahl von Anwendungsfälle langfristig zu enormen Kosten und letztendlich zur Frage, wie ausreichend Energie zu einem wirtschaftlichen Preis zur Verfügung gestellt werden kann.

Um die Nachfrage nach künstlicher Intelligenz langfristig zu bedienen und deren Energiebedarf nachhaltig zu senken, bietet es sich daher an, nicht nur die Software an biologischen Konzepten zu orientieren, sondern auch ein ähnliches Schema auf der Hardware-Ebene anzuwenden. Ein Ansatz zur Restrukturierung der Hardware nach biologischem Vorbild kann materialbasiert mit magnetischen Materialien erfolgen, denn die physikalische Beschreibung von magnetischen Materialien gleicht der nicht-linearen Dynamik neuronaler Netzwerke.

Die Spintronik verwendet sowohl das magnetische Moment, also den Spin, als auch die Ladung von Elektronen um Informationen zu speichern und zu berechnen. Antiferromagnete weisen schnellere Dynamik auf, ermöglichen kleinere Speicherelementen und besitzen erhöhte Stabilität im Vergleich zu Ferromagneten. Dennoch steht die nur schwer mögliche Auslese des antiferromagnetischen Zustandes der Verwendung von Antiferromagneten als aktive Komponente in revolutionären Datenspeichern im Wege. Somit zeichnet sich das Zusammenführen der bewährten Manipulierbarkeit von Ferromagneten mit den vorteilhaften Eigenschaften von Antiferromagneten in antiferromagnetisch-ferromagnetischen Hybridsystemen als nächster Schritt ab.

Diese Doktorarbeit widmet sich der Untersuchung von Grenzflächenphänomenen im Kontext des magnetischen Grundzustandes und der magnetischen Dynamik in antiferromagnetisch-ferromagnetischen Hybridsystemen.
Auf Grund der quantenmechanischen Natur magnetischer Phänomene, deren Manifestation aber auch in der klassischen Physik geschieht, ist ein Multiskalenansatz zu deren Beschreibung notwendig. In dieser Arbeit verwenden wir sowohl phänomenologische, als auch numerische Methoden. Es werden sowohl atomistische, als auch mikromagnetische Simulationen angewendet.
Zunächst wird demonstriert, dass mit Hilfe der Schnittstellenaustauschwechselwirkung ferromagnetische Strudeltexturen auf eine angrenzende antiferromagnetische Schicht geprägt werden können. Insbesondere kann der antiferromagnetische Néel Vektor durch den ferromagnetischen Zustand beeinflusst werden, wodurch das Auslesen des antiferromagnetischen Zustandes ermöglicht wird. In diesem kollaborativen Projekt bestand die Aufgabe des Autors darin, sowohl die theoretische Modellierung experimenteller Daten zu leiten und auszuführen, als auch den Austausch zwischen Experiment und Theorie zu koordinieren. Es wurde ein Modell entwickelt, welches die Stabilität des eingeprägten antiferromagnetischen Strudelzustands beschreibt. Sowohl ein phänomenologisches Modell, als auch mikromagnetische Simulationen werden zur Hand genommen, um damit erfolgreich experimentelle Ergebnisse im NiO(111)-Fe(110) Modellsystem zu nachzubilden. Damit wurde gezeigt, dass NiO-Fe Hybridsysteme dazu geeignet sind, magnetische Strudel als fundamentale logische Einheiten für Rechnungszwecke aufzuweisen. Dabei werden nicht nur die Vorteile antiferromagnetischer Dynamik integriert, sondern auch das konventionelle Auslesen des magnetischen Zustandes über den Ferromagneten ermöglicht.
Weiterhin wird der gekoppelte magnetische Grundzustand und die gekoppelte Magnetisierungsdynamik in hybriden Mn_2Au-$Ni_{80}Fe_{20}$ (Py, Permalloy) Dünnschichtfilmen analysiert. Dieses Projekt fand statt im Rahmen des Transregio Sonderforschungsbereiches der Deutschen Forschungsgesellschaft (DFG) Projekt-TRR 173 Spin + X: spin in its collective environment (Projekt B12 und A05). Die Rolle des Autors gestaltete sich darin, dass er den Austausch mit den Kollaborateuren koordinierte, die experimentellen Daten modellierte und daraus die gemessene Stärke der Schnittstellenaustauschwechselwirkung berechnete. Mit Hilfe eines phänomenologischen Modells wird gezeigt, dass die Schnittstellenaustauschwechselwirkung in Mn_2Au-Py zu einer Einprägung der antiferromagnetischen Domänenstruktur auf die ferromagnetische Schicht führt. Diese Ausrichtung ermöglicht das

Auslesen des antiferromagnetischen Zustandes und wird nicht nur mittels Analytik, sondern auch mit atomistischen Spin-Simulationen belegt. Im dynamischen Regime führt die Schnittstellenaustauschwechselwirkung zur gekoppelten Spindynamik und hat zur Folge, dass die ferromagnetische Resonanzmode des Py nicht nur mit höherer Frequenz auftritt, sondern auch in zwei Moden geteilt wird. Diese dynamischen Effekte, die aus einer sehr stark ausgeprägten Schnittstellenaustauschwechselwirkung herrühren, sind einzigartig und wurden bisher nur in dem gezeigten Materialsystem nachgewiesen. Dies ist belegt durch die Übereinstimmung experimenteller Daten aus ferromagnetischen Resonanz und Brillouin Lichtstreuexperimenten mit der theoretischen Modellierung. Schließlich werden atomistische Spin-Simulationen angewandt um zu demonstrieren, dass eine gekoppelte Domänenwandbewegung mit hoher Geschwindigkeit durch Anwendung eines Magnetfeldes an die ferromagnetische Komponente des Hybridsystemes initiiert werden kann.

Zusammenfassend wurde gezeigt, dass durch die Kombination von Antiferromagneten und Ferromagneten in Hybridsystemen die Dynamik des Ferromagneten durch die Präsenz der antiferromagnetischen Schicht signifikant beschleunigt werden kann, während die konventionelle Manipulierbarkeit erhalten bleibt. Zusäztlich zeigt die Aufspaltung der ferromagnetischen Resonanzmode, dass eine Synergie mit den intrinsischen Eigenschaften des Antiferromagneten und der ferromagnetischen Dynamik geschaffen wurde.

Contents

List of Abbreviations

AFM Antiferromagnetic, antiferromagnet

AI Artificial Intelligence

ANN Artificial neural network

BLS Brillouin light scattering

CMOS Complementary metal oxide semiconductor

DMI Dzyaloshinskii-Moriya interaction

DW Domain wall

FM Ferromagnetic, ferromagnet

FMR Ferromagnetic resonance

GMR Giant magneto resistance

GPU Graphical processing unit

IoT Internet of things

LLG Landau-Lifshitz-Gilbert (equation)

MRAM Magnetic random access memory

MTJ Magnetic tunnel junction

NN Neural Network

NSOT Néel spin orbit torque

PEEM Polarized electron emission microscope

SOT Spin-orbit torque

SRAM Static random access memory

STT Spin-transfer torque

TMR Tunneling magneto resistance

TPU Tensor processing unit

VNA-FMR Vector network analyzer ferromagnetic resonance

XMCD X-ray magnetic circular dichroism

XMLD X-ray magnetic linear dichroism

1 Preface

While depictions of sentient beings created by humans reach back to 700 BC, when Hesiod described his Talos, our current understanding of artificial intelligence (AI) is strongly rooted in ideas conceived during the twentieth century [1]. In 1950 Alan Turing published his seminal work on "Computing Machines and Intelligence" in which he defines how to test the cognitive capabilities of human-made objects and Isaac Asimov wrote his novel "I, Robot" in which he coined the three laws of robotics. AI gained traction through the 1956's conference "Dartmouth Summer Research Project on Artificial Intelligence", hosted by John McCarthy and Marvin Minsky, in which the feasibility of AI algorithms as we know them today was laid out [2]. Contributing significantly to the public perception of AI, Marvin Minsky was also the lead designer of the HAL 9000 sentient computer in the 1968 science fiction movie "2001: A Space Odyssey" by Stanley Kubrick [3].

The capability to compute has been a catalyst to human development. Already in ancient times the first cornerstones for the development of Mathematics were laid out in Mesopotamia, India and China, which later significantly drove the development of the hellenic society of ancient Greece [4]. Since the founding of modern universities in the late medieval period in Europe, the influence of the scientific method on society and the accompanying necessity to compute has become indispensable.

Today we witness another revolution: our society transitions from being information driven to being intelligence driven. For the first time in history, humans have access to enough computing power to shape a new kind of intelligence, AI.

AI enables new possibilities, that can be harnessed most efficiently when many components to which we are in contact in our lives are interconnected in the internet of things (IoT). In doing so, large amounts of data are generated and need to be processed - this is what is called big data. AI, IoT and big data herald a digital revolution that will influence the life of everybody in a digital society.

1.1 The Rise of Artificial Intelligence and its Challenges

Studying and mimicking perceptual and cognitive intelligence requires intelligent computing. Understanding of human intelligence is crucial to drive the development of autonomous intelligence and human-machine synergy. Key areas of application for AI lie in drug discovery, medical research and treatment, defense, education and finance [5–7].

Despite recent successes of AI also challenges loom ahead. AI needs to improve its interpretability, generality, evolvability and autonomy [7]. Simultaneously, advances in AI have been accompanied by increasing power consumption. For example, ChatGPT consumes 500 000 kWh per day (200 million requests) [8] and the training of OpenAI's GPT-4 has cost $100 million in electricity alone [9]. In order to sustain AI's current rate of development, available power needs to double every 100 days [10]. The annual growth rate of the energy demand is projected to be 26%-36% [5].

Actually, AI requires 80% of its lifecycle resource demand not during the initial training phase, but during the inference phase [5]. As the number of applications of AI steadily increases, this share will also grow. At the same time, computers do not only need to become more energy efficient, but also more computationally powerful. In 2018 OpenAI conducted a study to track the growth of the largest neural networks (NNs) based on computing power, shown in Fig. 1.1 [11]. What they found is that the amount of computing power required for a breakthrough model scaled with Moore's law until 2015; that is the doubling of computing power every two years. And the rate of change drastically increased since then.

One reason for the struggle of modern computers to keep up with the increasing demands of more powerful AI algorithms is the von-Neumann architecture they employ: data is processed and stored in different devices [12]. Whenever an algorithm executes a computation, data is transferred between the memory device and the processor. The limited bandwidth of the memory-processor interconnec-

tion is called von-Neumann bottleneck [13]. As the performance gap between the processor and the memory widens, the need for in-memory computing becomes conspicuous.
Software inspired by biological NNs has significantly contributed to recent advances in AI using conventional computing hardware [6] and it can help make in-memory computing a reality. However, today's heavily parallelized graphical processing units (GPU), still operate using orders of magnitude more power than the human brain per operation and require supervised training [6]. So a solution is to extend the approach driven by biological concepts from the software level to the hardware level. An alternative to the von-Neumann architecture of today's computers is neuromorphic computing, that utilizes neurons and synapses to control memory and processing, akin to the human brain [6, 7, 11].
Mitigation of the performance gap between biological and computational systems can follow in the form of a material-based approach. Dynamically, the components of a NN follow the same non-linear physical description as that of the magnetization reversal in magnetic materials [6]. In order to describe magnetic systems, the spin degree of freedom of the electron has to be taken into account. In combination, the revolution in terms of computing architecture and the evolution of computing devices in terms of computing efficiency fosters a hybrid approach to tackle today's AI and computing challenges.

1.2 Spintronics - A Tool for Progress

Spintronics describes the study of the spin degree of freedom of the electron and the connected magnetic moment in solid state systems [14]. The history of spintronics has been written by several key breakthroughs. Commonly the discovery of the giant magnetoresistance effect (GMR) simultaneously by A. Fert and P. A. Grünberg, that describes a large change in the electrical resistance of metallic layer systems upon magnetization reorientation in the ferromagnetic (FM) layers with respect to one another using a magnetic field, marks the beginning of the field of spintronics in 1988 [15, 16]. They were awarded the 2007 Nobel Prize in Physics for their discovery [17–19]. Thanks to commercialization studies and material optimization by S. Parkin, GMR became the industry standard technology for magnetic sensing in hard disk drive read heads by 1996 [20, 21].
Another success of spintronics was the wide adoption of magnetic tunnel junctions (MTJs) using tunneling magnetoresistance (TMR) as the basic unit of magnetic storage and sensing in the early 2000s [22, 23]. In an MTJ the tunneling current

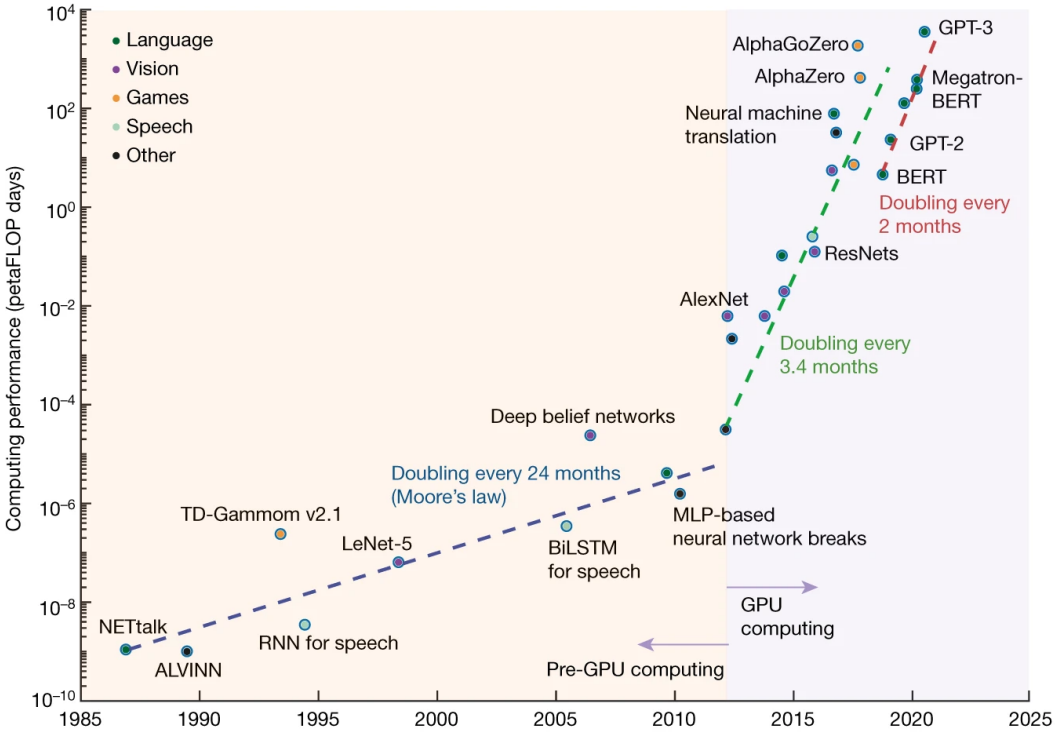

Figure 1.1: Increasing computing power demand. The computing performance (in the number of petaFLOP operations performed in a day) required for the realization of a breakthrough AI model has doubled every two years until 2015, akin to Moore's law for the number of transistors on a chip. This rate of progress has increased to a doubling approximately every two months today. This figure was taken from [11].

between two FM electrodes separated by a thin oxide layer is controlled by an external magnetic field and it can be used as a non-volatile storage element. M. Julliére first discovered the TMR effect in 1975 [24] and J. Moodera and T. Miyazaki confirmed its existence in 1991 and 1994, respectively [25, 26]. In many fields such as automotive, consumer electronics, healthcare and industry magnetic sensors based on the GMR effect are used [27], while magnetic random access memory (MRAM) based on the TMR effect has long replaced embedded flash and static RAM (SRAM) [14, 28].

Writing information in MRAMs has been achieved using magnetic fields, electric currents and through the conversion of the electronic spin and charge degrees of freedom in spin transfer torque MRAM (STT-MRAM) [29]. STT-MRAM provides storage that is non-volatile, because power to the device is only required during operation and the saved memory state is stable without applied power in standby.

STT-MRAM does not need as much power and, as a side effect, less power distribution infrastructure, such that devices shrink by up to 80% in size compared to non-STT-MRAM technology [30]. Smaller devices revolutionized standalone memory in wearable electronics, IoT, always-on processors and AI computing [14]. Industry acceptance of STT-MRAM has been quick because the materials used in the devices can be manufactured using known complementary metal oxide semiconductor (CMOS) techniques [30].
Moreover, the applicability of STTs reaches beyond STT-MRAM. In racetrack memory devices, magnetic domain walls (DWs), vortices and skyrmions represent fundamental logical units and are driven by STT or its orbital sibling, spin orbit torque (SOT) [14, 31–33]. And the non-linear spiking behavior of STT nano-oscillators suits well the leaky integrate-and-fire statistics of neuromorphic computing [34].
In fact, more than one approach within spintronics is set to realize neuromorphic computing. In magnonics, information is encoded within the amplitude and phase of a fundamental excitation, also called a magnon or a spin wave, of the magnetic metal or insulator [14]. Then, signals between neurons propagate as spin waves. As spin waves possess intrinsically non-linear dynamics, their interactions can naturally represent the weighted signal processing in neuromorphic computing and perform pattern recognition [14]. Additionally, spin waves propagate without Joule-heating losses, making them very energy efficient [14].
In neuromorphic computing, artificial neural networks (ANNs) are the computational realization of NNs designed to model the human brain [6]. Neurons in these networks are units that aggregate incoming signals before generating an output signal based on their activation function [6]. Neurons are arranged in layers and interconnected by synapses, which modulate signals according to trained weights that update with every revision of the NN [6]. Because of this structure, the synapses in NNs represent multilevel memory and the NN itsself intermixes logic and storage. These properties make NNs incompatible with the von-Neumann architecture.
One way to tackle the incompatibility issues is the manufacturing of dedicated CMOS circuits that perform only one specific kind of computational task, e.g. a tensor processing unit (TPU) which calculates high volume, low precision matrix calculations during synaptic weight training [6].
Memory cells, whose stable state can be used as memory, i.e. which are non-volatile, and which have more than two stable states, which makes them ideal for storing synaptic weights, are called memristors [6]. Memristors change their

conductance based on their magnetic texture. In similarity to synapses, memristors modulate the electrical current between neurons [6]. Multilevel, progressive current-driven switching by SOT of the FM layer has been observed in antiferromagnetic-ferromagnetic (AFM-FM) bilayer systems [6]. On the contrary, a FM alone does not exhibit memristive behavior, which arises due to exchange bias and is, thus, rooted deeply within the presence of the antiferromagnet (AFM) [6, 35]. Hence, the AFM part of the bilayer is responsible for non-volatile, multilevel switching. Based on the performance of AFM-FM hybrid systems the question arises whether AFMs alone could be used as memristors, or in other words, whether AFMs could be used as the active component in spintronic devices.

1.2.1 Antiferromagnetic Spintronics

AFMs provide natural, ultra-fast dynamics in the THz regime, and they are very energy efficient [36]. In equilibrium their magnetic state is compensated. As a result, AFMs provide optimal spatial downscaling potential due to the absence of stray fields [37]. Finally, they are impervious to external magnetic fields, which reduces crosstalk between devices [14].
In today's spintronics devices, FMs are the active components. Magnetic fields and electric currents are used to manipulate the FM state. However, the FM state can also influence the AFM state, for instance through exchange bias [35]. Still, the readout of the compensated AFM state with no net magnetization remains challenging.
AFM-FM bilayers aim to unify the intrinsic benefits of AFMs with the known manipulability of FMs. While the AFM can be the source of a spin current and of interface exchange coupling, the readout could be facilitated by the FM by conventional means. At the same time, the intrinsic properties of AFM dynamics could be made accessible through the manipulability of the FM. In order to harness the potential of both FMs and AFMs in hybrid systems, a thorough understanding of the interface effects taking place between the AFM and the FM layers is key. This emphasis on interface effects is ubiquitous in spintronics, as many functionalities are obtained from interfaces and hybrid systems [14]. As an example, interfacial effects dominate the GMR and TMR effects [14]. This thesis covers the study of the static and dynamic effects of interface exchange coupling between AFM and FM layers in AFM-FM hybrid bilayer systems.

1.3 Outline of the Thesis

In this thesis we present four primary chapters, a conclusion chapter and the appendix. Chapters 3 and 4 present our key findings, which have been published as described in Sec. B.1. The thesis is organized as follows.

In Chapter 2 we introduce the fundamental concepts behind the work presented in this thesis. First, we discuss the concept of magnetic order and a phenomenological model is introduced to describe both static and dynamic effects. Within this framework we derive the Landau-Lifshitz-Gilbert (LLG) equation. We continue with the description of AFMs, magnetic excitations and interface exchange coupling. The computational approaches employed throughout this thesis are micromagnetic and atomistic spin dynamics simulations. We address the transition between the continuum description of a magnetization field in the micromagnetic model and the discrete atomistic spins in the atomistic spin model. Finally, we consider the limitations of each of the models.

We start presenting our research results in Chap. 3. In this chapter we demonstrate how a FM vortex texture can be imprinted onto the adjacent AFM layer via interface exchange coupling in AFM-FM hybrid bilayer systems. In particular, we report a change of the AFM ground state configuration. We phenomenologically calculate the conditions under which the AFM transitions from its homogeneously oriented ground state into a vortex state as a function of the interface exchange coupling strength and the AFM layer thickness. Using micromagnetic simulations, we analyze the stability of the imprinted AFM vortex state. Finally, we report good agreement of our results with experimental data from the NiO(111) (4 nm) - Fe (110) (6 nm) model system.

In Chap. 4 we report our key research findings for the AFM-FM bilayer system Mn_2Au-Py. We explore the coupled magnetic statics and dynamics of Mn_2Au-Py thin film hybrids. We utilize a phenomenological model to reveal that interface exchange coupling in Mn_2Au-Py causes an imprinting of the AFM domain texture on the FM layer. Furthermore, we find that interface exchange coupling leads to coupled spin dynamics in Mn_2Au-Py, a frequency enhancement and a frequency splitting of the FM resonance (FMR) mode in the Py. Changing of the FM layer thickness enables control over the FMR frequency and dispersion of Py. We report good agreement of our results with experimental data from FMR and Brillouin light scattering (BLS) experiments on Mn_2Au-Py thin films. Moreover, we consider the coupled DW motion in Mn_2Au-Py. Our atomistic spin dynamics simulations

demonstrate that DW motion can be initiated by acting on the FM magnetization with magnetic fields and find a limiting DW velocity of 8.5 km/s.
Finally, we summarize our key findings in Chap. 4.5 and give a short perspective on the future prospects of this field of research.

2 Fundamentals and Methods

This chapter introduces the fundamental concepts behind the work presented in this thesis. After exploring the fundamental concepts of magnetic order, a phenomenological model is used to describe both static and dynamic effects. Within this framework we derive the LLG equation. Special emphasis will be given to the description of AFMs, magnetic excitations and interface exchange coupling. The computational approaches employed throughout this thesis are micromagnetic and atomistic spin dynamics simulations. The transition between the continuum description of a magnetization field in the micromagnetic model and the discrete atomistic spins in the atomistic spin model is addressed. Finally, the limitations of each of the models are considered. [1]

2.1 Magnetic Order

Some materials possess an intrinsic magnetic order below an ordering temperature and in absence of an external magnetic field. In the ordered phase microscopic magnetic moments align to form a net magnetization. Going through the ordering temperature the system looses its magnetic order in the high temperature phase. The magnetic order is called collective magnetism.

In the classical description an electric current in a closed loop generates a magnetic moment [40, 41]. Analogously, the atomic magnetic moments result from the orbiting electron. This is the Rutherford-Bohr model [42, 43]. Simultaneously, the mass of the electron generates an angular momentum. The theoretical description was

[1] For this chapter inspiration was taken from the theses of Severin Selzer [38] and Marijan Beg [39].

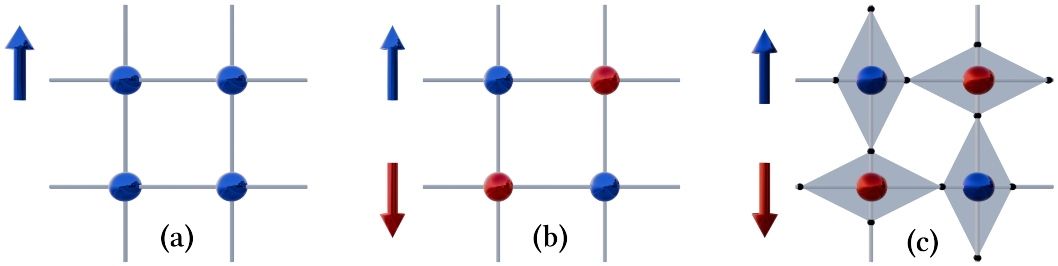

Figure 2.1: Magnetic Ordering. (a) Magnetic moments (blue dots) on a lattice, which order ferromagnetically (arrow). (b) Magnetic moments of two magnetic sublattices (blue and red dots) on a lattice, which order antiferromagnetically (arrows). The color is associated with the orientation of the spin. (c) Altermagnetic order. Additionally to (a) and (b), the local crystallographic environment of the two magnetic sublattices (red, blue) is not isotropic (non-magnetic atoms shown in black).

confirmed through the Einstein-de-Haas experiment, which found the existence of an associated angular momentum and first uncovered that the electron's magnetic moment and its angular momentum are always antiparallel [44–46]. However, the fundamental fault of the theoretical description lies therein, that the electron's velocity vector continually changes its direction as the electron orbits the nucleus. This change in direction would result in electromagnetic radiation, thereby violating energy conservation.

In order to explain intrinsic magnetic moments and very short range magnetic interactions one needs to apply a quantum mechanical description. Bohr first postulated the quantization of angular momentum [42]. Thereby, the smallest unit of angular magnetic moment came to be known as the Bohr magneton. Bohr stated that the angular momentum results from the electron's wave function in the central potential of the nucleus. The Stern-Gerlach experiment discovered an additional kind of angular momentum: the intrinsic spin [47]. Hence, the total atomic angular momentum is composed of both the orbital angular momentum generated by the orbiting electrons and the electron's intrinsic spin. Developments in the emerging field of orbitronics have shown that the orbital degrees of freedom can play an important role for transport phenomena [48]. However, for many effects in magnetism the orbital degrees of freedom are suppressed such that only the spin is considered. Henceforth, a single atomic magnetic moment is usually referred to as a spin. This description is valid for isolated atoms. Embedding the atom into a crystal lattice leads to modifications, which can be incorporated in effective descriptions.

The interaction of spins and the associated static and dynamic effects can be described by the exchange interaction. It results from the overlap of the electron's wave functions in combination with the Pauli exclusion principle [49]. For the relation between the spin alignment and the energy two conflicting pictures can be chosen: the Heisenberg picture [50], that considers localized electrons and the Stoner picture [51], that considers delocalized electrons.
For elevated temperatures thermal fluctuations lead to disorder. The Curie temperature is the the ordering temperature of a FM, above which no net magnetization is formed, or in other words, the alignment of the magnetic moments that characterized the ordered state is lost [52]. On the one hand, in the Heisenberg picture in the high temperature regime, the magnetic moments remain, but their orientation is disordered. In the Heisenberg picture, magnetic excitations are transverse spin waves, which we will discuss later.
On the other hand, the Stoner picture considers magnetic excitations as spin flips. But the Stoner model overestimates the Curie temperature and fails to accurately resemble the temperature dependence of the FM ground state, also called the Curie-Weiss law [53]. Thus, the Stoner model is suited more to the description of the electronic structure of delocalized electronic systems at low temperatures. The Heisenberg model succeeds at describing magnetic insulators, but also works well for some systems with delocalized electrons, like 3-d transition metals and localized f-electron systems [54, 55]. Henceforth, in this thesis we work with the Heisenberg picture.
Depending on the local environment and the exchange interactions of the magnetic moments in a material, different forms of magnetic order can arise. Each kind of magnetic order is a phase described by an order parameter. In collinear FM materials the magnetic moments align in parallel, such that below the Curie temperature, a net magnetization is formed [50]. We show the FM alignment schematically in Fig. 2.1. The magnetization is the order parameter. Going through the Curie temperature the FM undergoes a phase transition and the net magnetization vanishes. Above the Curie temperature, the FM enters a paramagnetic phase. In this phase, the material still exhibits magnetic moments, but their orientation is disordered, such that no net magnetization arises [40].
Because a FM possesses a net magnetic moment it couples efficiently with an applied field. In order to reduce the Zeeman energy, which we will introduce below, the magnetic moments rotate until all magnetic moments align with the applied magnetic field and the magnetization is saturated. The magnetization value of the

material is called the saturation magnetization.
After an applied field is withdrawn, the FM magnetization reduces to its nonzero remanent magnetization. Only when the applied magnetic field is subsequently applied in the opposite direction and its magnitude surpasses a threshold called the coercive field does the FM magnetization flip into the opposite direction and into alignment with the external field. The existence of a remanent magnetization is due to magnetic hysteresis [40]. If the external field is applied perpendicular to the magnetization it induces a rotation.
AFMs on the other hand possess magnetic ordering, but no net magnetization in equilibrium. The magnetic moments are organized into magnetic sublattices. Inside these magnetic sublattices, the magnetic moments interact ferromagnetically and assume parallel alignment. However, in AFMs two exchange interactions are at play. Additionally to the intra-sublattice exchange interaction, that orders ferromagnetically ($\mathcal{O}(100\,\mathrm{T})$) [56], the much stronger inter-sublattice exchange interaction orders spins of different sublattices ($\mathcal{O}(1000\,\mathrm{T})$) [56] such that the magnetic moments compensate in equilibrium and the net magnetization vanishes. In principle an AFM material can have more than two magnetic sublattices, but in this thesis we concentrate on collinear AFMs with two magnetic sublattices. Thus, the inter-sublattice exchange interaction orients spins of different sublattices antiparallel, as shown in Fig. 2.1. Because the net magnetization vanishes in equilibrium, we use the difference of the sublattice magnetizations, called the Néel vector, as the order parameter for the state of the AFM [57].
Above the Néel temperature the magnetic moments loose their alignment, the Néel vector vanishes and the AFM enters the paramagnetic phase. Treatment of AFM dynamics can be complicated. Out of equilibrium the variation of the Néel vector in time gives rise to a finite, dynamic magnetization that results from the temporal misalignment of the magnetic sublattices. The presence of a net magnetization in the other wise compensated AFM leads to a rich spectrum of phenomena. Since the strong inter-sublattice exchange interaction wants to mitigate the net magnetization in order to restore compensation, it induces dynamics in the THz range. This phenomenon is called exchange enhancement [56, 58] and defines AFM dynamics, see Sec. 2.3.3.
Altermagnets are magnetically compensated like AFMs, because their spins alternate in orientation for neighboring atomic sites. However, their electronic bands are not Kramers degenerate [59, 60]. This particular set of properties stems from the crystal environment of each atomic site, where atoms with opposing magnetic

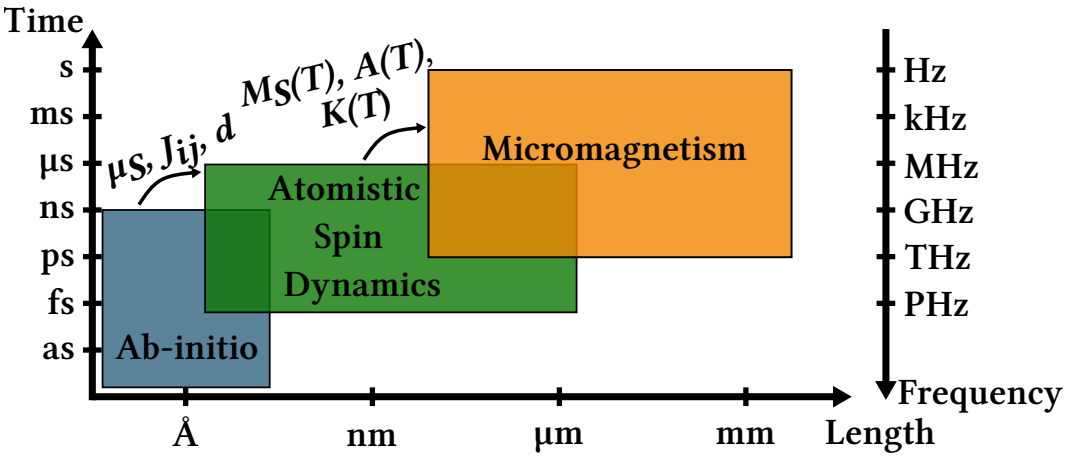

Figure 2.2: Multiscale modeling methods used in computational magnetism. For each method the applicable time, frequency and space scales are shown. The flow of parameters from one model to the next is indicated. Figure recreated from [61].

moment can be transformed into one another by a crystal rotation, see Fig. 2.1. In the case of AFMs, the transformation is either by translation or inversion.
Ferrimagnets differ from AFMs by having different magnetization magnitudes in the sublattices, such that they are not fully compensated. Both altermagnets and ferrimagnets exhibit a unique blend of properties from both FMs and AFMs, while at the same time introducing proprietary phenomena.
There are also non-collinear forms of magnetic order. But in this thesis we concentrate on collinear FMs and AFMs. In every magnetic phase, lattice defects, material structures and magnetostatic interactions induce magnetic domains. These domains are regions in which the magnetic order parameter orients homogeneously. Such magnetic domains are separated by magnetic DWs, that are excitations over the homogeneous magnetic ground state, as we show in Sec. 2.3.2. Treatment of such excitations, as well as magnetization dynamics and the influence on transport phenomena are the main tasks of computational magnetism.

2.2 Computational Magnetism

The description of magnetic phenomena is a multiscale problem: The interactions between magnetic moments that give rise to interaction strengths and anisotropies are of relativistic and of quantum origin and take place on a subatomic level. Microscopic magnetic spins interact on the atomic level and domains lead to magnetization dynamics on macroscopic length scales.
Ab-initio calculations within the frame work of density functional theory are used

to examine the electronic band structure of materials and to estimate exchange interactions and crystal anisotropies, as well as transport coefficients. Taking the material parameters from ab-initio calculations, the magnetization dynamics can be simulated in the nano meter range using atomistic spin dynamics simulations. Larger areas and collective phenomena require a coarse grained ansatz, which is called the micromagnetic framework. We display the time, frequency and spatial scale of each approach in Fig. 2.2. We indicate in Fig. 2.2 how parameters can flow from one method to the next in order to form a multiscale modeling of magnetic phenomena. In this thesis we concentrate on atomistic spin dynamics and micromagnetic simulations.

In atomistic spin dynamics simulations each magnetic atom is associated with a magnetic moment of fixed length. The interaction of the magnetic moments is described by the LLG equation for spin dynamics, which we will present in Sec. 2.3.2. Thermal effects can be included using the Landau-Lifshitz-Bloch equation [62]. The parameters for this theory are taken from ab-initio calculations or fitted phenomenologically to experimental data. This approach is used for the description of magnetic phenomena in the nano meter range and on pico to nano second time scales, as shown in Fig. 2.2. Atomistic spin dynamics simulations are especially suited for the simulation of temperature dependent response functions, like the magnetic susceptibility, or non-equilibrium phenomena, like magnetic phase transitions [61]. Another unique advantage is the implementation of the internal properties of the material, like the crystal structure, into the model. Likewise, combinations of different materials into heterostructures can be replicated realistically.

The major drawback for atomistic spin dynamics simulations is that the temperature dependence of the magnetization is estimated incorrectly due to the classical statistics of the thermal bath [63]. In reality the spin is quantized and does not vary continuously on the unit sphere. Furthermore, the fixed length requirement for the spin makes atomistic spin models not apt for describing induced magnetic moments in heavy metals like Pt or materials with Stoner-like excitations like in Ni, in which the length of the magnetic moments changes significantly [64]. Small ensembles suffer most from these effects, as for larger systems these influences can be averaged out. Furthermore, the degeneracy of the AFM ground state can lead to paramagnetic behavior even at low temperature if the simulated ensemble is too small. Finally, atomistic spin simulations have a high computational cost that stems most of all from the computation of the long range magnetostatic interactions. Most simulations are limited to $N < 10^8$ spins.

In order to simulate larger systems a coarse graining approach can be used, in which the magnetization is averaged over a finite volume element. In the macrospin approximation all magnetic moments in a volume element are reduced to a single spin with constant moment, the macrospin. Then, the interactions and dynamics of several macrospins can be studied.
In the micromagnetic approach, the magnetization is a continuous vector field that varies in time and space. Subsequently, the magnetization field is discretized into cells for the numerical evaluation of the equation of motion. For both the macrospin and the micromagnetic models the LLG equation in its continuum formulation, see Sec. 2.3.3, is used to describe the magnetization dynamics. Some parameters that were obtained through ab-initio calculations and used for atomistic spin dynamics simulation can be converted into a continuum formulation. However, this translation is only possible in general for bcc crystal lattices, see Sec. 2.3.3 [65]. In most cases, effective parameters are obtained through phenomenological models that fit experimental or simulation data.
Due to the averaging process, we loose the information about all influences that occur on length scales below the averaging length, like for instance the crystal structure. Furthermore, the micromagnetic approach requires the magnetization field to vary slowly in time and space. This is problematic, especially in the case of AFM dynamics, where the inter-sublattice exchange plays a dominating role or in multilayer systems with atomically thin layers. Furthermore, the description of thermal effects is challenging. Near the phase transition point the correlation length diverges and thereby exceeds the averaging length. Thus, near phase transitions and when large thermal fluctuations occur the micromagnetic model loses its validity.
Like for atomistic spin dynamics simulations, the Landau-Lifshitz-Bloch equation can be used. In this frame work also the longitudinal relaxation of the average moment is included [62]. However, micromagnetic simulations are much more efficient compared to atomistic spin dynamics simulations and they can be used to model systems in the micro meter to milli meter range at nano second to milli second time scales [61]. Their unique use case is the modeling of experimental results at controlled temperatures and in large, multi domain systems. Also the dynamics of magnetic excitations like DWs and skyrmions can be understood from a micromagnetic approach, as we will see in Sec. 2.3.2. The limits of micromagnetic simulations stem from the coarse graining towards smaller scales and shorter times and from computational cost toward larger scales and longer times.

2.3 Methods

In the previous sections we have seen the fundamental concepts of magnetic order. Furthermore, the multiscale approach of computational magnetism was outlined. In the following sections we will present the methods that were applied throughout this thesis. First, in Sec. 2.3.1 we will consider the phenomenological theory of classical atomistic spins that is based on the work of Landau and Lifshitz [66]. The resulting LLG equation is used for both the atomistic spin dynamics model in Sec. 2.3.2 and the micromagnetic model in Sec. 2.3.3.

2.3.1 Phenomenological Model

In Sec. 2.1 we have seen that the motion of magnetic moments in the presence of an external magnetic field is associated with angular momentum. The equation of motion is the LLG equation, that we will derive now.
In the Heisenberg picture the time evolution of a time-dependent quantum mechanical operator $A(t)$ is [41]

$$\frac{\mathrm{d}}{\mathrm{d}t} A(t) \;=\; \frac{i}{\hbar} [\mathcal{H},\, A(t)], \tag{2.1}$$

where $\mathcal{H}$ is the system's Hamiltonian. Consider now the rate of change of the x component of the angular momentum operator

$$\begin{aligned}
\frac{\mathrm{d}}{\mathrm{d}t} J_x \;&= \frac{i}{\hbar} [\mathcal{H},\, J_x] && (2.2)\\
&= \frac{i}{\hbar} \left(\frac{\partial \mathcal{H}}{\partial J_x} [J_x,\, J_x] \;+\; \frac{\partial \mathcal{H}}{\partial J_y} [J_y,\, J_x] \;+\; \frac{\partial \mathcal{H}}{\partial J_z} [J_z,\, J_x] \right) && (2.3)\\
&= \frac{\partial \mathcal{H}}{\partial J_y} J_z \;-\; \frac{\partial \mathcal{H}}{\partial J_z} J_y. && (2.4)
\end{aligned}$$

In Eqn. (2.3) we used the quantum mechanical identity $[f(A),\, B] \;=\; \partial f / \partial A\, [A,\, B]$, and in Eqn. (2.4) we used the commutation relation for the angular momentum operator $[J_i,\, J_j] \;=\; i\hbar\, \epsilon_{ijk}\, J_k$ [41]. Proceeding analogously for the other components we find

$$\frac{\mathrm{d}}{\mathrm{d}t} \mathbf{J} \;=\; -\mathbf{J} \times \frac{\partial \mathcal{H}}{\partial \mathbf{J}}, \tag{2.5}$$

where $\partial \mathcal{H} / \partial \mathbf{J} \;=\; (\partial \mathcal{H} / \partial J_x,\, \partial \mathcal{H} / \partial J_y,\, \partial \mathcal{H} / \partial J_z)^{\mathrm{T}}$. We remember from Sec. 2.1 that the magnetic moment of the electron $\boldsymbol{\mu}$ is antiparallel to its angular momen-

tum $\mathbf{J}$, such that we can write $\boldsymbol{\mu} = -\gamma \mathbf{J}$, where γ is the gyromagnetic moment of the electron. As stated in Sec. 2.1 we refer to a single atomic magnetic moment of magnitude μ_S as a spin $\mathbf{S}$. Hence, we can write

$$\frac{\mathrm{d}}{\mathrm{d}t}\mathbf{S} = \frac{\gamma}{\mu_S}\mathbf{S} \times \frac{\partial \mathcal{H}}{\partial \mathbf{S}}. \tag{2.6}$$

We define the effective field $\mathbf{H}_{\text{eff}}$, $\mathbf{B}_{\text{eff}} := \mu_0 \mathbf{H}_{\text{eff}}$ such that

$$\frac{\mathrm{d}}{\mathrm{d}t}\mathbf{S} = \frac{\gamma\,\mu_0}{\mu_S}\mathbf{S} \times \mathbf{H}_{\text{eff}}. \tag{2.7}$$

The right-hand-side of Eqn. (2.7) describes the torque acting on the spin. This equation is called the Bloch equation and describes the precessive motion of a spin around the effective field vector [67]. By multiplying Eqn. (2.7) by $\mathbf{S}$ we find that it is spin conserving $\mathrm{d}^2/\mathrm{d}t^2\,\mathbf{S} = 0$.
When we consider a system of spins, we obtain a system of coupled equations, where each spin is described by one equation

$$\frac{\mathrm{d}}{\mathrm{d}t}\mathbf{S}_i - \frac{\gamma}{\mu_S}\left(\mathbf{S}_i \times \mathbf{B}_{\text{eff}}(\{\mathbf{S}_i\})\right) = \mathbf{T}_i, \tag{2.8}$$

where the interaction of the spins (internal torques) is given by the second term on the left-hand-side of the equation and the right-hand-side represents external torques that are generated by external stimuli, like applied fields and currents.
In Sec. 2.3.2 we will use the atomistic spin dynamics model and show that the LLG equation Eqn. (2.9) for discrete spins results from the Bloch equation

$$\frac{\mathrm{d}}{\mathrm{d}t}\mathbf{S}_i = \frac{\gamma}{\left(1 + \alpha_G^2\right)\mu_S}\left(\mathbf{S}_i \times \left(\mathbf{B}_i + \alpha_G\,\mathbf{S}_i \times \mathbf{B}_i\right)\right), \tag{2.9}$$

where α_G is the Gilbert damping and $\mathbf{B}_i = -\partial\mathcal{H}/\partial\mathbf{S}_i + \boldsymbol{\eta}_i(t)$ is the effective field for spin $\mathbf{S}_i$. Within the Landau-Lifshitz-Bloch model, thermal noise $\boldsymbol{\eta}_i(t)$ can be incorporated into the model [62].
In Sec. 2.3.3 we apply a continuum transformation $\mathbf{S}_i \rightarrow \mathbf{M}(\mathbf{r}, t)$ to translate the LLG equation into a formulation for the magnetization field

$$\frac{\mathrm{d}}{\mathrm{d}t}\mathbf{M} = \frac{\partial}{\partial t}\mathbf{M} - \frac{\gamma}{M_S}\left(\mathbf{M} \times \mathbf{B}_{\text{eff}}\right), \tag{2.10}$$

where we have omitted the dependencies of the magnetization for clarity and M_S is the saturation magnetization. The effective field $\mathbf{B}_{\text{eff}}$ results from the functional variation of the energy density functional.

2.3.2 Atomistic Spin Dynamics Model

The atomistic spin dynamics model makes the following assumptions:

1. Adiabatic approximation: The spin system is independent from the electronic band energies and the crystal lattice. Influences from these sources are treated via effective interactions, e.g. are contained in the interaction constants.

2. Localized magnetic moments: We approximate magnetic moments (spins) or magnetization densities by localized classical atomistic spins. This approximation fits well for 4f states in rare earths and the delocalized, itinerant electronic 3d states in transition metals. Furthermore the length of the classical atomistic spins is assumed to be constant.

The Heisenberg model describes the interaction of classical atomistic spins with the exchange Hamiltonian [68]

$$\mathcal{H}_{\text{exch}} = -\frac{1}{2} \sum_{i \neq j} \mathbf{S}_i^{\mathrm{T}} \mathbf{J}_{ij} \mathbf{S}_j, \tag{2.11}$$

where $\mathbf{S}_i := \mu_i / \mu_S$ is the normalized magnetic moment at site i, $\mathbf{J}_{ij}$ is the exchange tensor and the sum runs over all sites j except site i.
In magnetic multilayer systems, such as the AFM-FM bilayers investigated in this thesis, the exchange interaction can also couple spins of two different materials through an interface. In this case the Spin $\mathbf{S}_i$ would belong to one magnetic material, while all other spins $\mathbf{S}_j$ considered in the summation belong to the other material. Computationally, a cutoff would be used to set how far into the material the interface exchange coupling would be considered, as it is an interface effect.
The exchange tensor has three contributions

$$\mathbf{J}_{ij} = J_{ij} \, \mathbb{1} + \mathbf{J}_{ij}^{S} + \mathbf{J}_{ij}^{A}, \tag{2.12}$$

where the first term is the isotropic exchange $J_{ij} = 1/3 \, \mathrm{Tr}(\mathbf{J}_{ij})$ ($\mathbb{1}$ is the identity matrix), $\mathbf{J}_{ij}^{S} = 1/2 \, (\mathbf{J}_{ij} + \mathbf{J}_{ji}^{\mathrm{T}}) - J_{ij} \, \mathbb{1}$ is the traceless symmetric and $\mathbf{J}_{ij}^{A} = 1/2 \, (\mathbf{J}_{ij} - \mathbf{J}_{ji}^{\mathrm{T}})$ is the antisymmetric part.
The isotropic exchange dominates over the other contributions in most cases, such that the exchange Hamiltonian becomes

$$\mathcal{H}_{\text{exch}} = -\frac{1}{2}\sum_{i\neq j}\mathbf{J}_{ij}\,\mathbf{S}_i\,\mathbf{S}_j \approx -J\sum_{<ij>}\mathbf{S}_i\cdot\mathbf{S}_j. \tag{2.13}$$

The sign of J_{ij} determines the type of magnetic ordering: For $J_{ij} > 0$ the magnetic ground state is FM and for $J_{ij} < 0$ AFM. In the collinear AFM case the ground state will be degenerate and the magnetization compensated. For the AFM case the exchange tensor can be separated into three contributions. The first contribution accounts for $\mathbf{S}_i$ and $\mathbf{S}_j$ belonging to the same sublattice A (intra-sublattice exchange). The second contribution accounts for spins of the same sublattice B (intra-sublattice exchange). Finally, the third contribution considers spins belonging to different sublattices A and B (inter-sublattice exchange). The full exchange matrix can be obtained from ab-initio calculations and used in the atomistic spin dynamics simulation. Oftentimes it is sufficient to consider nearest neighbor exchange, such that only the spin neighbor pairs $< ij >$ are included; the factor $1/2$ is introduced to avoid double counting. The exchange tensor then reduces to an effective exchange constant J.

In systems with broken inversion symmetry the antisymmetric part of the exchange tensor $\mathbf{J}_{ij}^{A}$ is non-zero. The symmetry analysis that revealed the existence of the antisymmetric exchange interaction and the phenomenological description was developed by Dzyaloshinskii [69], while Moriya later found spin-orbit coupling to be the cause of this relativistic interaction [70]. Hence, antisymmetric exchange is known as the Dzyaloshinskii-Moriya interaction (DMI). The DMI leads to chiral magnetic textures, where spins are oriented perpendicularly to each other in equilibrium and we can write the DMI Hamiltonian as

$$\mathcal{H}_{\text{DMI}} = -\frac{1}{2}\sum_{i\neq j}\mathbf{S}_i^{\mathrm{T}}\,\mathbf{J}_{ij}^{A}\,\mathbf{S}_j = -\frac{1}{2}\sum_{i\neq j}\mathbf{D}_{ij}\left(\mathbf{S}_i\times\mathbf{S}_j\right), \tag{2.14}$$

where the components of the DMI vector $\mathbf{D}_{ij}$ are

$$D_{ij}^{x} = \frac{1}{2}\left(J_{ij}^{yz} - J_{ij}^{zy}\right), \tag{2.15}$$

$$D_{ij}^{y} = \frac{1}{2}\left(J_{ij}^{zx} - J_{ij}^{xz}\right), \tag{2.16}$$

$$D_{ij}^{z} = \frac{1}{2}\left(J_{ij}^{xy} - J_{ij}^{yx}\right). \tag{2.17}$$

The traceless symmetric part of the exchange tensor $\mathbf{J}_{ij}^{S}$ is sometimes also re-

ferred to as the twosite anisotropy or anisotropic exchange and can result from interactions of the magnetic atom with its (non-magnetic) neighbors [71, 72]. Terms of the sum, for which $i = j$ are treated as shown as follows.
Relativistic spin orbit coupling leads to magnetic anisotropy, which are written by terms of the kind $\sum_i \mathbf{S}_i^{\mathrm{T}} \mathbf{K}_i \mathbf{S}_i$, where $\mathbf{K}_i$ is the anisotropy tensor at site i. One kind of magnetic anisotropy is the magnetocrystalline anisotropy, which gives the spins a preferred orientation with respect to the crystallographic high symmetry axes. In general, the magnetic anisotropy is given by an expansion in even powers of spin components

$$\mathcal{H}_{\mathrm{anis}} = -\sum_i \left(k_{i,x} \left(S_i^x\right)^2 + k_{i,y} \left(S_i^y\right)^2 + k_{i,z} \left(S_i^z\right)^2 \right) \tag{2.18}$$

$$-\sum_i \left(k_{i,xx} \left(S_i^x\right)^4 + k_{i,yy} \left(S_i^y\right)^4 + k_{i,zz} \left(S_i^z\right)^4 \right) \tag{2.19}$$

$$-\sum_i \left(k_{i,xy} \left(S_i^x S_i^y\right)^2 + k_{i,xz} \left(S_i^x S_i^z\right)^2 + k_{i,yz} \left(S_i^y S_i^z\right)^2 \right) \tag{2.20}$$

$$-\sum_i k_{i,xyz} \left(S_i^x S_i^y S_i^z\right)^2 \ldots, \tag{2.21}$$

Eqn. (2.18) represents systems in which cetrain magnetic *easy axes* are energetically favored (e.g. for $k_{i,x} > 0$, $k_{i,y} = 0$, $k_{i,z} = 0$ the x axis is a magnetic easy axis) and the anisotropy is *uniaxial*. For $k_{i,x} < 0$ the spins lie in the plane perpendicular to the x axis and the anisotropy is *easy plane*. Both Eqns. (2.19) and (2.21) are higher order contributions that can be included depending on the present magnetic symmetries.
Also more complicated crystal structures and their resulting anisotropies can be obtained. For instance, a tetragonal anisotropy is given by

$$\mathcal{H}_{\mathrm{anis}} = -\sum_i k_{i,z} \left(S_i^z\right)^2 - \sum_i k_{i,xy} \left(S_i^x S_i^y\right)^2, \tag{2.22}$$

with $k_{i,z} < 0$ such that the spins lie in the plane and $k_{i,xy} > 0$ such that the easy axes are the diagonals of the xy plane.
The magnetic moments of the spins create stray fields, that are magnetic field lines outside the magnet. Because magnetic moments are dipoles, they interact via the classical dipole-dipole interaction [73]

$$\mathcal{H}_{\text{dipole-dipole}} = -\sum_{i \neq j} \frac{\mu_{ij}}{2} \left(\frac{3 \left(\mathbf{S}_i \cdot \mathbf{r}_{ij} \right) \left(\mathbf{r}_{ij} \cdot \mathbf{S}_j \right)}{\mathbf{r}_{ij}^5} - \frac{\mathbf{S}_i \cdot \mathbf{S}_j}{\mathbf{r}_{ij}^3} \right), \tag{2.23}$$

where $\mu_{ij} := \mu_{S,i}\, \mu_{S,j}\, \mu_0 / (4\,\pi)$ with the vacuum permeability μ_0 and the connecting vector between the positions of site i and j is $\mathbf{r}_{ij}$. The dipole-dipole interaction is weak, but long range, as its sum does not converge. In order to reduce the energy loss through stray fields the magnetic moments at the boundary of the system align in parallel with the border to form a closed loop. If a closed loop configuration is not possible, a DW can be induced. Here, the dipole-dipole energy compensates the energy penalty through the exchange interaction of the DW. Dipole-dipole interactions vanish in systems without net magnetization, like AFMs.
The Zeeman energy gives the interaction of spins with an external magnetic field [73]

$$\mathcal{H}_{\text{Zeeman}} = -\sum_i \mu_{S,i}\, \mathbf{B}_i \cdot \mathbf{S}_i, \tag{2.24}$$

where $\mathbf{B}_i$ is the external field.
The total Hamiltonian of the system is given by the sums of the individual Hamiltonians that were presented in this section

$$\mathcal{H} = \mathcal{H}_{\text{exch}} + \mathcal{H}_{\text{DMI}} + \mathcal{H}_{\text{anis}} + \mathcal{H}_{\text{dipole-dipole}} + \mathcal{H}_{\text{Zeeman}}. \tag{2.25}$$

Atomistic spin dynamics are phenomenologically described by the Landau-Lifshitz equation [66]

$$\dot{\mathbf{S}}_i = -\frac{\gamma_i^*}{\mu_{S,i}} \mathbf{S}_i \times \mathbf{H}_i - \frac{\alpha_{\text{LL}}}{\mu_{S,i}} \mathbf{S}_i \times \mathbf{S}_i \times \mathbf{H}_i, \tag{2.26}$$

where $\mathbf{H}_i = -\partial \mathcal{H} / \partial \mathbf{S}_i$ is the effective field, γ_i is the absolute value of the gyromagnetic ratio and α_{LL} is a damping constant. The first term stems from Bloch equation (2.7), which describes a torque that is perpendicular to the spin and tangential to its precessive motion, as shown in Fig. 2.3. The second term was added phenomenologically by Landau and Lifshitz to account for the dissipation of energy to the electronic and lattice degrees of freedom in an otherwise conservative motion. It creates a torque that is perpendicular to the spin and to its trajectory, as shown in Fig. 2.3. Thereby, the amplitude of the spin's precession is reduced and it eventually relaxes into a state parallel to the effective field $\mathbf{H}_i = -\partial \mathcal{H} / \partial \mathbf{S}_i$. Because both terms create torques that are perpendicular to the spin, the spin length

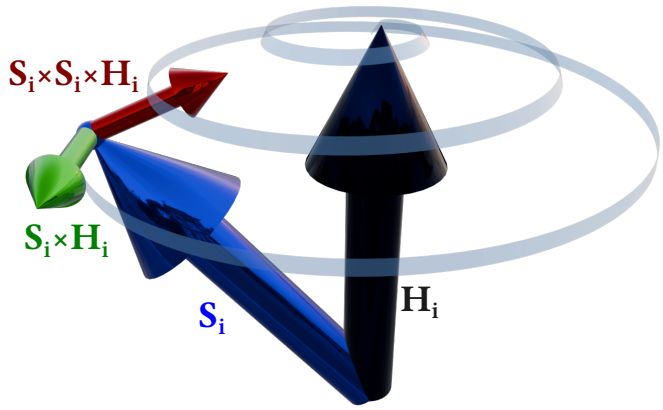

Figure 2.3: Precession of a classical atomistic spin $\mathbf{S}_i$ around the effective field $\mathbf{H}_i$. The field-like (green) and damping-like (red) terms of the LL equation are indicated.

is conserved. However, the Landau-Lifshitz equation leads to unphysical results at high damping [74, 75]. Gilbert introduced another phenomenological damping term in what is known today as the LLG equation [76, 77]

$$\dot{\mathbf{S}}_i = -\frac{\gamma_i}{\mu_{S,i}} \mathbf{S}_i \times \mathbf{H}_i + \alpha \, \mathbf{S}_i \times \dot{\mathbf{S}}_i, \tag{2.27}$$

with typical values of the Gilbert damping constant α being between 0.001 and 0.01. In fact, the Landau-Lifshitz equation can be recovered from the LLG equation by rescaling the gyromagnetic ratio as $\gamma^* = \gamma/(1 + \alpha^2)$ and the damping as $\alpha_{\mathrm{LL}} = \gamma\,\alpha/(1 + \alpha^2)$.

Brown united the LLG model with Langevin temperature-driven dynamics [78] by adding a stochastic noise term to the effective field

$$\mathbf{H}_i = -\frac{\partial \mathcal{H}}{\partial \mathbf{S}_i} + \boldsymbol{\xi}_i, \tag{2.28}$$

$\boldsymbol{\xi}_i$ depends on the type of noise of the system. One popular choice is Gaussian noise, which means that the noise is not correlated in space or time and the first average moment of $\boldsymbol{\xi}_i$ vanishes [73]. Furthermore, the variance of $\boldsymbol{\xi}_i$ has to be adjusted such that the fluctuation dissipation theorem is fulfilled and the resulting spin configuration is Boltzmann distributed.

In this work we use the well tested, open source atomistic simulation software VAMPIRE [79].

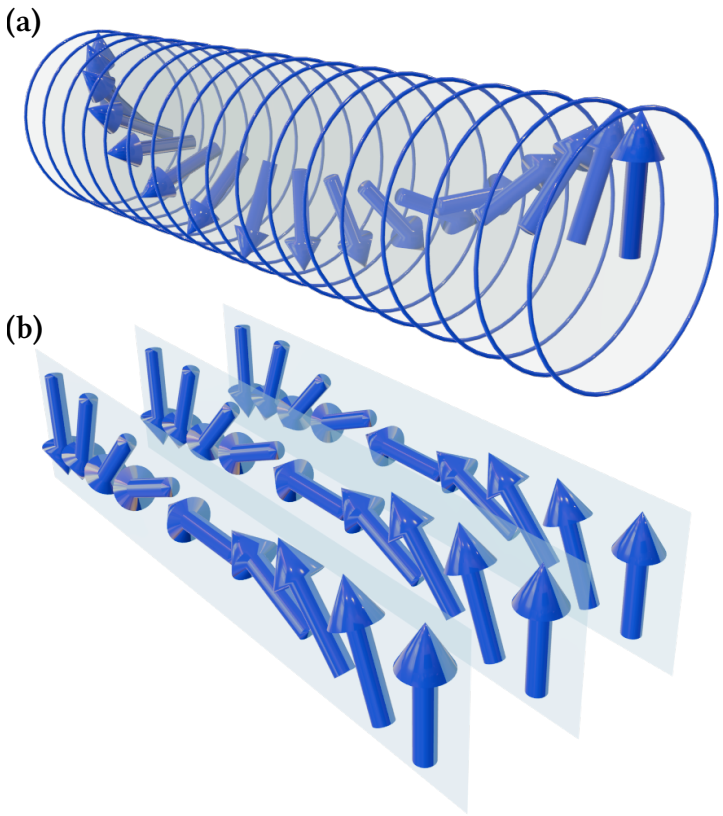

Figure 2.4: (a) Bloch DW. (b) Néel DW.

Magnetic Excitations

As soon as a system exhibits an ordered magnetic ground state, the possibility of magnetic excitation over the ground state arises. We consider two types of excitations: DWs and spin waves.

A magnetic DW is the interface region that connects magnetic domains [40]. In the DW the magnetization performs a gradual reorientation in order to match the magnetization orientation of the adjacent domains. The angle through which the magnetization rotates characterizes the DW. We consider either a rotation with an angle of 90° or 180° that connects the magnetic domains. In addition there are two kinds of rotation of the magnetization. On the one hand, in a Bloch DW the magnetization rotates in a plane parallel to the plane of the DW, as shown in Fig. 2.4 (a). Bloch DWs are found in the bulk of a material, where the system size is considerably larger than the DW width. On the other hand, in a Néel DW the magnetization rotates in a plane perpendicular to the plane of the DW, as shown in Fig. 2.4 (b).

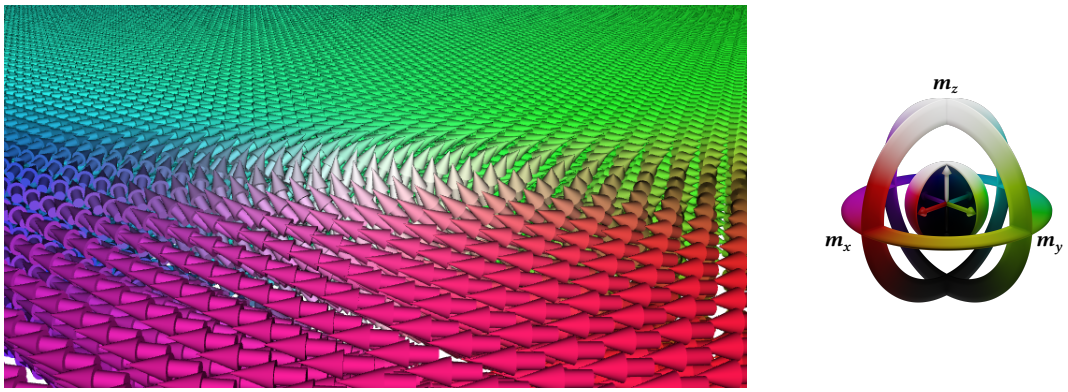

Figure 2.5: View along the profile of a magnetic vortex. The local magnetization is shown by arrows, whose orientation is given by the color code on the right [80, 81].

A DW forms because of defects in the magnetic and crystal lattice system or dipole-dipole interactions. We have discussed before, that the dipole-dipole interaction can favor the formation of domains in order to reduce stray fields in FMs. The DW width is finite because of competing magnetic interactions. The exchange interaction favors parallel alignment of the magnetization and thus drives the DW width towards infinity. However, the magnetocrystalline anisotropy stops the DW from unwinding, because it prefers if the magnetization orients along the magnetic easy axes and favors an atomically sharp DW. That way, the magnetization does not intermittently point along a magnetic hard axis. As a compromise, the DW width for a 90° DW is

$$x_{\mathrm{DW}} = \pi \sqrt{\frac{A}{K}}, \tag{2.29}$$

where A is the exchange stiffness and K is the magnetocrystalline anisotropy constant [40], as they will be defined in Sec. 2.3.3. The energy per unit area of the DW is given by

$$\sigma_{\mathrm{DW}} = \pi \sqrt{AK}. \tag{2.30}$$

DWs also exist in AFMs, where the role of the magnetization is played by the sublattice magnetization. As a result, there are intertwined DWs; one for each sublattice. Collectively, the Néel vector profile is then similar to the magnetization profile of a DW in FMs. Because there are no dipole-dipole interactions in AFMs, AFM DWs nucleate at lattice defects.
If we now consider a square microscopic region that is bounded from four sides, in

a FM dipole-dipole interactions would dictate that the magnetization aligns with each boundary. It becomes evident, that DWs would arise connecting every side with its opposite neighbor. As a consequence, the magnetization direction forms a circle along the edges in either a clockwise or counterclockwise sense of rotation. A problem arises at the center, where the magnetization's in-plane direction is degenerate. Thus, it will point out of the plane, as shown in Fig. 2.5. This magnetic texture is a vortex. Looking at the vortex magnetization texture as a magnetization field, we cannot smoothly translate it into a texture, where the magnetization does not rotate at all other than unwinding the texture. Topological textures are characterized by their winding number. It means that the vortex is a quasiparticle that cannot be annihilated without some energy input. This is called topological protection. Both DWs and vortices are candidates for information carriers in novel computing architectures because of their stability and manipulabilty [34].
Spin waves are elementary excitations of the Heisenberg model, where the spins perform a collective precession with a constant phase shift between neighboring spins [82]. We show an illustration of a spin wave in Fig. 2.6. Spin waves can also be derived in a quantum mechanical picture, where they are spin 1 bosonic quasiparticles, that are quantized. They are also called magnons - in analogy to their lattice-vibrational counterpart - phonons [82]. We can classify spin waves according to their dispersion. In FMs, and for small wave vectors k, the dispersion is quadratic: $\omega \sim k^2$ [82]. This dispersion gives the FM magnon an effective mass, in analogy to real particle excitations. While for AFMs, the dispersion is linear in k: $\omega \sim k$ [58, 82]. The difference stems from the inherently different AFM dynamics, which we will consider in Sec. 2.3.3. The dispersion of magnetic excitations gives an indication for how fast information can be transmitted through the system. When, for instance, magnetic domains are used in data storage devices, the magnetization direction in a domain yields information. In order to access or modify the stored information, the magnetization direction must be switched. The achievable frequency of this switching determines how fast the device can write and read information. This frequency is related to the dispersion of the material [34].

2.3.3 Micromagnetic and Macrospin Models

For computationally expensive simulations of larger magnetic systems on larger time scales, a coarse-grained approach on the atomistic LLG model is used. This model is called the micromagnetic model and contrary to its name, the microscopic

Figure 2.6: Spin wave. The spins perform a collective precession with a constant phase shift between neighboring spins

properties of the system are not taken into account, but rather averaged out. In this model we do not consider spins of individual atomic sites, but rather a continuous magnetization field. Similarly, the macrospin model averages the magnetization over a finite volume element, but then associates a single discrete macro spin with each volume element.
For the micromagnetic model we take the following assumptions:

1. Overdamped Approximation: The magnetization field $\mathbf{M}(\mathbf{r}, t)$ is continuous and slowly changing in both time and space. $\mathbf{M}(\mathbf{r}, t)$ is defined as the density of atomic magnetic moments.

2. The magnitude of magnetization is constant and both time and space invariant. We can write the magnetization as $\mathbf{M}(\mathbf{r}, t) = M_S\,\mathbf{m}(\mathbf{r}, t)$, where M_S is the saturation magnetization that gives the magnitude of the available magnetization and $\mathbf{m}(\mathbf{r}, t)$ the reduced magnetization, which is a unit vector field.

These assumptions can essentially be translated into the requirement that locally the magnetic moments are mostly parallel and, thus, that we are dealing with

a system that is dominated by the exchange interaction on short length scales. The treatment of AFMs will be discussed in more detail in Sec. 2.3.3.
For the numerical solution of the micromagnetic model the vector field has to be discretized into equally spaced volume elements. The cell size should not be below a critical length scale that is given by the system parameters in order to not average out important information. This critical length scale is the exchange length, below which the exchange interaction will dominate over all other interactions. The exchange length is given by $l_{\text{exch}} = \sqrt{A/K}$, where A is the exchange stiffness constant and K is the anisotropy constant [83]. In order to transform the atomistic model into a continuum theory we replace all sums by integrals over the volume of the magnetization vector field. As a consequence, the model parameters become thermodynamic, temperature-dependent densities. While a Hamiltonian describes the energy eigenstates of the atomistic model, the free energy density becomes the energy potential that describes the state of the magnetization field.
We will now proceed by transforming the atomistic Hamiltonian's contributions into micromagnetic free energy densities. We consider nearest neighbor exchange (Eqn. (2.13))

$$\mathcal{H}_{\text{exch}} = -J \sum_{<ij>} \mathrm{S}_i \cdot \mathrm{S}_j = -J \sum_{<ij>} 1 - \frac{(\mathrm{S}_i - \mathrm{S}_j)^2}{2}, \tag{2.31}$$

where we have used $2\,\mathrm{S}_i \cdot \mathrm{S}_j = \mathrm{S}_i^2 + \mathrm{S}_j^2 - (\mathrm{S}_i - \mathrm{S}_j)^2$. We can now replace the atomistic spins by the magnetization field

$$\begin{aligned} \mathbf{m}(\mathbf{r}) \cdot \mathbf{m}(\mathbf{r} + \boldsymbol{\delta}\mathbf{r}) &= 1 - \frac{1}{2} \left(\mathbf{m}(\mathbf{r}) - \mathbf{m}(\mathbf{r} + \boldsymbol{\delta}\mathbf{r})\right)^2 \\ &\approx 1 - \frac{1}{2} \sum_{\alpha = x,y,z} \left(\boldsymbol{\delta}\mathbf{r} \cdot \nabla_\alpha \, \mathbf{m}(\mathbf{r})\right)^2, \end{aligned} \tag{2.32}$$

where we have taken into account that differences in first order expansions can be expressed as spatial derivatives and omitted temporal dependencies for clarity.
The exchange contribution to the free energy density becomes [84, 85]

$$\omega_{\text{exch}} = \sum_{\alpha = x,y,z} A \left(\nabla_\alpha \, \mathbf{m}\right)^2 = \sum_{\alpha = x,y,z} A \left(\frac{\partial \mathbf{m}}{\partial \alpha}\right)^2 = \sum_{\alpha = x,y,z} A \, \mathbf{m} \cdot \frac{\partial^2 \mathbf{m}}{\partial \alpha^2}, \tag{2.33}$$

where A is the magnetic exchange stiffness. More details on the conversion from

the exchange constant to the exchange stiffness are given in Tab. 2.1.
The conversions of the DMI, uniaxial anisotropy (along the unit vector direction $\hat{z}$) and Zeeman contributions give

$$\omega_{\mathrm{DMI}} = d\,\mathbf{m}\cdot(\nabla\times\mathbf{m}), \tag{2.34}$$

$$\omega_{\mathrm{anis}} = -K_z\,(\mathbf{m}\cdot\hat{z})^2 - K_{zz}\,(\mathbf{m}\cdot\hat{z})^4 - \ldots, \tag{2.35}$$

$$\omega_{\mathrm{Zeeman}} = -\mathbf{M}\cdot\mathbf{B}_{\mathrm{ext}}. \tag{2.36}$$

We refer to Tab. 2.1 for the conversion of the parameters d, K_z, K_{zz}. Other anisotropies can be transformed accordingly.
In the micromagnetic model the Zeeman contribution accounts for the interaction of the magnetization field with an external magnetic field. At the same time, the coarse grained contribution of the microscopic dipole-dipole interactions leads to a magnetostatic energy that is generated by the interaction of the magnetization field with their intrinsic magnetic field [65]. Because magnetostatic interactions favor states with reduced stray fields, they lead to a demagnetization field $\mathbf{B}_{\mathrm{demag}}$. The demagnetization field can be found by considering Maxwell's equations [65]

$$\nabla\cdot\mathbf{B}_{\mathrm{demag}} = -\mu_0\,\nabla\cdot\mathbf{M}, \tag{2.37}$$

$$\nabla\times\mathbf{B}_{\mathrm{demag}} = 0. \tag{2.38}$$

The free energy density of the demagnetization field is

$$\omega_{\mathrm{demag}} = -\frac{1}{2}\,\mathbf{M}\cdot\mathbf{B}_{\mathrm{demag}}. \tag{2.39}$$

In the micromagnetic approach the interface exchange coupling of a FM and an AFM layer is described by the coupling of the FM magnetization within one volume element in the FM material with the AFM Néel vector in the adjacent volume element of the other material. We phenomenologically introduce interface exchange coupling such that it favors parallel alignment of the FM magnetization with the AFM Néel vector and vice versa. Such a phenomenological description cannot account for the reason why such an alignment is favored. It was experimentally and theoretically shown, that for Mn_2Au-Py, the very smooth surface morphology at the interface between the two layers contributes to such a strong alignment of the magnetization and the Néel vector [86, 87]. It was further shown experimentally

that such a coupling scales linearly with the thicknesses of the layers in the bilayer system [88], suggesting an interface effect. Thus, we can model interface exchange coupling as an effective interface exchange

$$\omega_{\text{int. exch}} = -J_{\text{exch}}\,\xi\,\mathbf{m}\cdot\mathbf{n}, \tag{2.40}$$

where J_{exch} is the interface exchange coupling strength, ξ is a length parameter that limits the influence of the coupling to the interface region and $\mathbf{n}$ is the AFM Néel vector.
The total free energy of the magnet is a functional in terms of the magnetization vector field, as shown below.

$$W[\mathrm{m}] = \int_V \left(\omega_{\text{exch}} + \omega_{\text{DMI}} + \omega_{\text{anis}} + \omega_{\text{demag}} + \omega_{\text{Zeeman}}\right) \mathrm{d}^3 r + \tag{2.41}$$

$$\int_A \omega_{\text{int. exch}}\,\mathrm{d}^2 r, \tag{2.42}$$

where A is the surface area of the sample and V is the volume. Because interface exchange coupling is a surface effect, it is integrated only over the area of the sample along the surface normal under consideration. Also the contributions from multiple surfaces can be summed up.
The conversion of the atomistic model constants into micromagnetic parameters in general is not straightforward, as it depends on the density of magnetic atoms in the material and is, thereby, dependent on the crystal structure under consideration. Furthermore, the micromagnetic model assumes an even spacing of magnetic moments throughout the system, which can be assumed in many cases, but makes calculation of effective parameters challenging. Oftentimes, the temperature dependence and the value of micromagnetic parameters is obtained from fitting experimental data. In Tab. 2.1 we show the conversion for a cubic lattice structure with FM exchange at zero temperature.
The time evolution of the magnetization vector field is given by the LLG equation [66, 77]

$$\dot{\mathbf{m}} = -\frac{\gamma}{M_S}\,\mathbf{m}\times\mathbf{H}_{\text{eff}} + \alpha\,\mathbf{m}\times\dot{\mathbf{m}}, \tag{2.43}$$

where α is the Gilbert damping parameter [76, 77] and the effective field $\mathbf{H}_{\text{eff}} = \mathbf{B}_{\text{eff}}/\mu_0$ is the functional variation of the free energy density with respect to the magnetization field

Table 2.1: Conversion of atomistic constants and micromagnetic parameters for a cubic lattice structure with FM exchange at zero temperature. a is the lattice constant, c is the number of atoms per unit cell ($c_{\text{sc}} = 1$, $c_{\text{bcc}} = 2$, $c_{\text{fcc}} = 4$) [65].

Atomistic	Micromagnetic	Conversion
Magnetic Moment μ_S in JT^{-1}	Sat. Magn. M_S in Am^{-1}	$M_S = \frac{c\,\mu_S}{a^3}$
Exchange Constant J in J	Exchange Stiffness A in Jm^{-1}	$A = \frac{c\,J}{2\,a}$
DMI Matrix Element D in J	DMI Constant in Jm^{-1}	$d = \frac{D\,c}{a^2}$
Anisotropy Constant k in J	Anisotropy Constant K in Jm^{-3}	$K = \frac{c\,d}{a^3}$

$$\mathbf{H}_{\text{eff}} = -\frac{1}{\mu_0 M_S}\frac{\delta W[\text{m}(\mathbf{r},\, t)]}{\delta \mathbf{m}(\mathbf{r}_0,\, t)}. \tag{2.44}$$

In this work we use the well tested, open source micromagnetic simulation software Mumax^3 [89].

Antiferromagnetic Dynamics

We consider now a two-sublattice collinear AFM. We can write down a set of equations in the micromagnetic model, where each magnetic sublattice is represented by its own magnetization field $\mathbf{m}_\alpha(\mathbf{r}) = \mathbf{M}_\alpha(\mathbf{r})/M_{S,\alpha}$, $\alpha = 1, 2$ [90]

$$\dot{\mathbf{M}}_1 - \gamma\, H_{\text{ex}}\, \mathbf{M}_2 \times \mathbf{M}_1 - \mathbf{M}_1 \times \mathbf{H}_{\text{eff},1} = \mathbf{T}_1, \tag{2.45}$$

$$\dot{\mathbf{M}}_2 - \gamma\, H_{\text{ex}}\, \mathbf{M}_1 \times \mathbf{M}_2 - \mathbf{M}_2 \times \mathbf{H}_{\text{eff},2} = \mathbf{T}_2, \tag{2.46}$$

where $M_{S,1} = M_{S,2}$. Here we introduced the inter-sublattice exchange field H_{ex}, that keeps the magnetic sublattices collinear. $\mathbf{H}_{\text{eff},\alpha}$ are the internal torques that result, e.g., from anisotropies and $\mathbf{T}_\alpha$ are externally applied torques.
At this point it is instructional to consider the hierarchy of interactions. Within the magnetic sublattice act intra-sublattice exchange fields, that have strengths of $\mathcal{O}(1000\,\text{T})$ and are responsible for the Néel temperature [56]. Because we consider an AFM, the two equations (2.45), (2.46) are connected by the exchange field H_{ex}, that acts between the magnetic sublattices. These inter-sublattice exchange fields have strengths of the order of 100 T and determine the susceptibility of the material [56]. In equilibrium, the collinear AFM is compensated. However, torques induced by external fields can cant the sublattice magnetizations out of their collinear

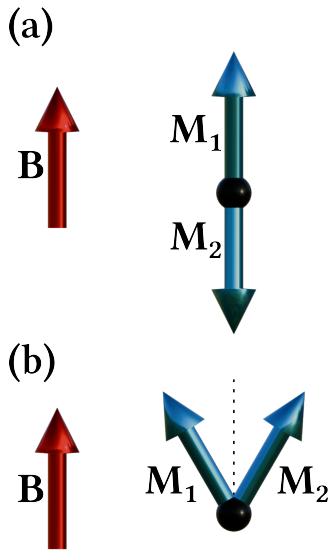

Figure 2.7: Spin flop transition. (a) The external magnetic field is applied collinearly with the magnetic sublattices of the AFM in equilibrium. (b) If the field strength surpasses the spin flop field, the magnetic sublattices flip out of their AFM ordering. For even stronger fields the magnetic sublattices align with the applied field.

alignment. This generates a small net magnetization associated with an angular momentum. In fact, the canting of the sublattice magnetization is connected with a phase transition. If an external magnetic field is applied parallel to one of the sublattice magnetizations, as shown in Fig. 2.7 (a), and its strength surpasses a threshold, the AFM system suddenly snaps into a configuration as shown in Fig. 2.7 (b). This is called a spin-flop transition [40]. The associated spin flop field $H_{\mathrm{sf}} = \sqrt{A\,H_{\mathrm{anis}}}$ (A is the intra-sublattice exchange field and H_{anis} is the anisotropy field) is the smallest of the AFM interaction strengths and is of the order of 1 T. As the external field strength is increased even further, the angle between the two sublattice magnetizations diminishes until the two sublattices are aligned with the external field and AFM order is lost.

Eqns. (2.45) and (2.46) are given in the sublattice representation. But they can also be converted to the symmetry representation. In order to do so, we use two order parameters: the Néel vector $\mathbf{n} = \mathbf{M}_1 - \mathbf{M}_2$ and the net AFM magnetization $\mathbf{m}_{\mathrm{AF}} = \mathbf{M}_1 + \mathbf{M}_2$. Furthermore, we note that both $\mathbf{n}$ and $\mathbf{m}_{\mathrm{AF}}$ do vary in length, but we require $\mathbf{n} \cdot \mathbf{m}_{\mathrm{AF}} = 0$ and $\mathbf{n}^2 + \mathbf{m}_{\mathrm{AF}}^2 = 1$. If one starts from a discrete model and then transforms the atomistic spins into micromagnetic vector fields, the averaging has to take place over cells that contain at least one spin of each sublattice.

As a result we can write

$$\dot{\mathbf{n}} - 2\gamma \mathbf{H}_{\text{ex}} \mathbf{m}_{\text{AF}} \times \mathbf{n} + \gamma \mathbf{n} \times \mathbf{B}_n = 0, \tag{2.47}$$

with $\mathbf{B}_n$ being the internal torques for the Néel vector. The total angular momentum remains conserved.
By taking the cross product of the Néel vector with Eqn. (2.47) we find

$$\mathbf{m}_{\text{AF}} \propto \frac{\mathbf{n} \times \dot{\mathbf{n}} + \gamma \mathbf{B}_n}{\gamma H_{\text{ex}}}. \tag{2.48}$$

In Eqn. (2.48) we can identify that AFM dynamics are intrinsically coupled to a small net magnetization $\mathbf{m}_{\text{AF}}$, which is directly proportional to the net angular momentum generated by canted sublattice magnetizations.
Now we proceed to find a closed equation for the Néel vector. We add Eqns. (2.45) and (2.46) and use the symmetry derived definitions of $\mathbf{n}$ and $\mathbf{m}_{\text{AF}}$ [57, 91] to find

$$\dot{\mathbf{m}}_{\text{AF}} - \frac{\gamma}{2} \mathbf{n} \times \mathbf{B}_n = \mathbf{T}. \tag{2.49}$$

where $\mathbf{T}$ is the sum of the torques $\mathbf{T}_\alpha$. We can now insert Eqn. (2.48) into Eqn. (2.49) and find

$$\mathbf{n} \times \ddot{\mathbf{n}} - H_{\text{ex}} \gamma^2 \mathbf{n} \times \mathbf{B}_n = \gamma H_{\text{ex}} \mathbf{T}. \tag{2.50}$$

By pulling the intra-sublattice exchange term out of the internal Néel vector torques $\mathbf{B}_n$ we can reformulate the equation of motion and find the AFM LLG equation for the Néel vector

$$\mathbf{n} \times \left(\ddot{\mathbf{n}} - c^2 \Delta \mathbf{n} \right) - H_{\text{ex}} \gamma^2 \mathbf{n} \times \mathbf{B}_n = \gamma H_{\text{ex}} \mathbf{T}, \tag{2.51}$$

with the AFM magnon velocity $c = \gamma \sqrt{A H_{\text{ex}}}$.
Eqn. (2.51) and Eqn. (2.43) directly showcase the differences between FM and AFM dynamics. The FM LLG describes the precessional motion of the magnetization. The scale of the frequency of the precession is given by the anisotropy field and the motion is non-relativistic. In contrast, AFM dynamics obey the laws of Newtonian dynamics because, due to the second-order time derivative, an inertia term is present in the equation of motion. Also every torque term is multiplied by the exchange field H_{ex}, and thereby enhanced in frequency. This exchange enhancement is the defining characteristic of AFM dynamics, which is responsible for the THz dynamics that make AFMs so attractive for applications [56, 58]. Lastly we iden-

tify the Lorentz-invariant relativistic dynamics through the term $\mathbf{n} \times \left(\ddot{\mathbf{n}} - c^2 \, \Delta \mathbf{n} \right)$, that fundamentally alter the magnon dynamics in AFMs, as discussed in Sec. 2.3.3. In contrast to the FM LLG equation, the AFM LLG equation has second order derivatives of the order parameter. As a result, it is difficult to solve in general and special cases have to be considered and appropriate approximations have to be taken [91]. In particular AFMs can be simulated micromagnetically in the static case. In equilibrium a collinear AFM is compensated. As a result, the AFM magnetization $\mathbf{m}_{\mathrm{AF}}$ vanishes and Eqn. (2.47) is solvable akin to the FM case [57].

Macrospin Model

There are cases when the micromagnetic description of a system can become unfeasible: for example particle clusters with particle sizes of the order of the exchange length or multilayer systems with very thin layers. In such cases the single-domain approximation leads to a simplification of the model such that the system can be solved analytically. Often such a simplified model already provides enough information such that the physical behavior can be investigated in the limiting cases. In the single-domain approximation, the magnetization of Néel vector order parameter is coarse grained over a finite volume element. Subsequently, a macro spin with constant length is associated with this region. The macrospin $\mathbf{m}$ is connected with the atomistic spin $\mathbf{S}_i$ and the micromagnetic magnetization field $\mathbf{m}(\mathbf{r})$ via

$$\mathbf{m} \, m_0 \;=\; \sum_{i=1}^{N} \mu_{S,\,i} \, \mathbf{S}_i \;=\; M_S \int \mathbf{m}(\mathbf{r},\, t) \, \mathrm{d}V, \tag{2.52}$$

where m_0 is the absolute value of the total magnetic moment.
For a macrospin the intra-sublattice exchange interaction and DMI are averaged out of the model, such that for a FM with uniform order parameter, the free energy consists just of anisotropy and external field terms. For AFMs, additionally the inter-sublattice exchange interaction has to be taken into account. The dynamics of the macrospin are described by the FM and AFM LLG equation, respectively.

3 Interface-Exchange Mediated Vortex Imprinting in NiO-Fe

In this chapter we demonstrate how a FM vortex texture can be imprinted onto the adjacent AFM layer via interface exchange coupling in AFM-FM hybrid bilayer systems. We find that the interplay between the interface exchange coupling and the AFM anisotropy facilitates an alignment of the Néel vector with the FM vortex magnetization texture. In particular, we succeed at locally reorienting the Néel vector out-of-plane at the center of the vortex texture in an in-plane AFM. We phenomenologically calculate the conditions under which the AFM transitions from its homogeneously oriented ground state into a vortex state as a function of the interface exchange coupling strength and the AFM layer thickness. Using micromagnetic simulations, we analyze the stability of the imprinted AFM vortex state. Furthermore, our simulations elucidate the influence of the interplay of the AFM anisotropy and the interface exchange coupling on the size of the vortex core. Specifically, we explain why the AFM vortex core is larger than the FM one. Finally, we report good agreement of our results with experimental data from the NiO(111) (4 nm) - Fe (110) (6 nm) model system.[1]

In Sec. 2.3.2 we have seen that topologically protected vortices show great potential for being the basic elements of unconventional computing [93, 94] and data storage [95, 96]. Therefore, it is desirable to stabilize vortices in magnetic systems.

[1]The following chapter and its sections have been transcribed from [92] and its supplementary material, with the second author of this reference being the author of this thesis. Individual contributions are detailed in Appendix B.1.

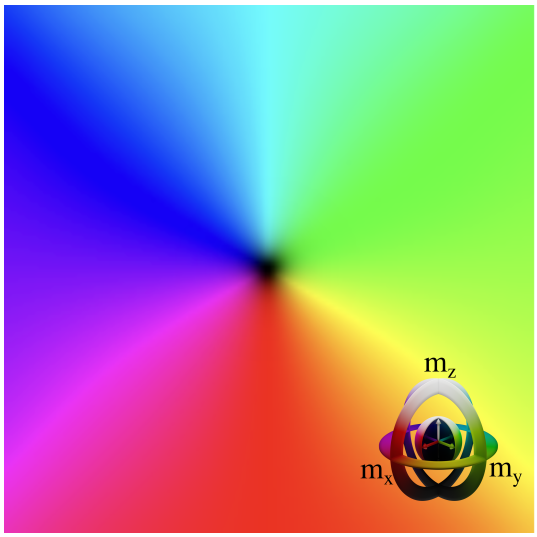

Figure 3.1: Vortex structure of the magnetization texture. The direction of the magnetization is encoded in color, as demonstrated by the color diagram in the bottom right corner (adapted from [80, 81]). The magnetization texture was obtained through micromagnetic simulation of a FM system.

Vortices like the one shown in Fig. 3.1 are commonly observed in FMs [97], while they are challenging to stabilize in AFMs [98]. But not only the creation of AFM vortex states is challenging, also their detection requires advanced methods.
Recently, the characterization of the magnetic properties of AFM materials at the nanoscale has garnered increased momentum through new developments of two experimental techniques: X ray linear magnetic dichroism (XMLD) [99, 100] and photoemission electron microscopy (PEEM) [101–105]. These techniques have made the detection of the topologically protected AFM textures such as vortices possible [106–110] and open up new opportunities to experimentally show the theoretical results we develop in the following chapter.
Our approach to stabilize and tune AFM vortex states is to first create vortices in a FM layer and then imprint the existing magnetization texture onto the AFM Néel vector distribution, where AFM properties such as imperviousness to magnetic fields and THz dynamics [106, 111, 112] add functional value to the vortex state. We use interface exchange coupling of the AFM Néel vector to the FM magnetization in order to transfer the vortex state form the FM to the AFM, as schematically shown in Fig. 3.2.

Interface exchange coupling describes the direct coupling between neighboring spins in the AFM and FM layers, as we discussed in Chap. 2. Both collinear

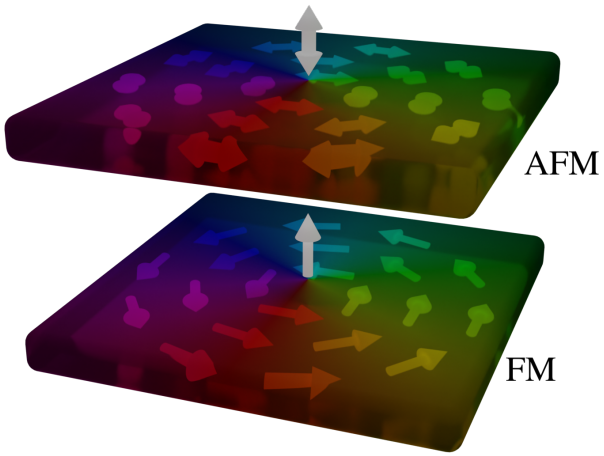

Figure 3.2: AFM-FM vortex imprinting. The bottom layer depicts the FM material, where both the color and the arrows demonstrate the orientation of the magnetization. The top layer is AFM; the color and double-arrows show the direction of the Néel vector [81].

exchange coupling in NiFe-Mn_2Au [86, 88], cf. Chap. 4, and perpendicular spin flop coupling in Co-NiO [113] have been reported. Interestingly, a spin reorientation transition in Fe leads to collinear interlayer exchange coupling for a thin Fe layer (thick NiO layer) and perpendicular spin-flop coupling for a thick Fe layer (thin NiO layer) in NiO-Fe [103, 104, 114]. Similar results were found for complex oxide AFM-FM systems [115] and CoO-Fe [116]. It was also found that strain induced from the substrate can reorient the NiO's Néel vector out-of-plane in NiO-Fe [105, 117]. Interlayer exchange coupling has often been reported in connection with a shift of the out-of-plane hysteresis of the coupled FM, a so called exchange bias [98, 102, 116, 118]. A shift of the hysteresis curve along the field axis occurs because of uncompensated moments in the AFM at the interface to the FM, that give a preferential direction of the FM magnetization in equilibrium. More rarely, also systems without a shifted hysteresis, specifically NiFe-Mn_2Au, can exhibit strong interface exchange coupling. This is due to an especially smooth surface morphology at the interface, such that no uncompensated moments occur and the FM couples to only one AFM sublattice [86, 88], as we will discuss in Chap. 4.

In continuous films it has been shown, that the AFM domain structure can be imprinted onto the magnetization texture of a coupled FM layer [86, 88, 107, 119, 120]. More commonly patterning is used to induce a shape anisotropy that aids the imprinting of a texture. For example, a FM vortex has been transferred to an AFM

in patterned, µm-sized discs of IrMn-NiFe [98, 102, 118] or CoO-Fe [101, 116]. In particular, interface exchange coupling has been used to imprint FM vortices from Fe onto AFM CoO and NiO patterned microstructures [101].
The gap that is left vacant by the previous research is the stabilization of vortex structures in AFM nanoparticles. Also the influence of interface exchange coupling on the properties of the imprinted vortex state has not been studied so far. In the following chapter we will develop a phenomenological model to describe conditions under which the AFM Néel vector follows the magnetization of an existing FM texture. Then, we will use micromagnetic simulations to numerically replicate the imprinting of a FM vortex magnetization texture onto an AFM. We will continue by analyzing the stability of the imprinted AFM vortex phase and provide a phase diagram of the AFM Néel vector orientation. We define the region of a vortex, in which the spins possess an out-of-plane component, as the vortex core. Our model will be extended and used to provide insight on the role of interface exchange coupling on the size of the imprinted AFM vortex core. Finally, we compare our numerical and analytical results to experimental data from NiO-Fe. The experimental data was provided by our collaborators Dr. Michal Ślezak, Dr. Anna Kozioł-Rachwał and Prof. Dr. Tomasz Ślezak from the AGH University of Krakow in Poland.

3.1 Influence on the Antiferromagnetic Ground State

In this section we will analyze the space of parameters of the AFM system spanned by the interface exchange coupling and the thickness of the AFM layer. The phase of the AFM is characterized by the the Néel vector.

We use a phenomenological model and considering an AFM-FM bilayer system with interface exchange coupling, as shown in Fig. 3.3a). The FM material is Fe(110), while the AFM is NiO. NiO is an AFM insulator and has a tetragonal crystal structure, as shown in Fig. 3.3b). The spins lie in the {111} easy planes along the $< 112 >$ symmetry equivalent directions. We assume that the NiO's [111] crystallographic direction is aligned with the vertical stacking axis of the bilayer, such that the ferromagnetically ordered sublattice planes are layered atop the FM. This arrangement facilitates strong FM interface exchange coupling between the Fe atoms and the NiO atoms of the sublattice closest to the interface.
In the FM, the FM exchange interaction energy is minimal for a homogeneously oriented magnetization throughout the sample. However, the magnetostatic inter-

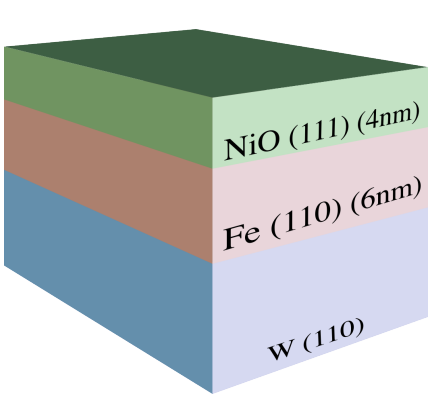

(a)

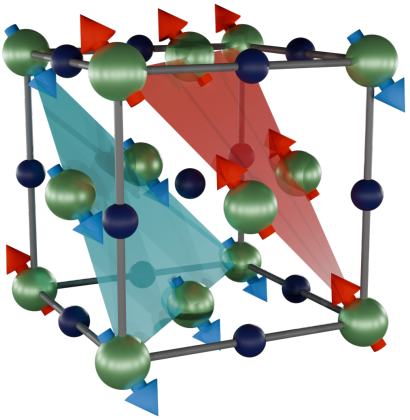

(b)

Figure 3.3: (a) Bilayer structure. Fe nanostructures were prepared on a W substrate. On top a continuous thin film NiO layer was deposited. (b) Crystal structure of NiO. Green atoms represent Ni, while blue atoms show nonmagnetic oxygen. The spins, colored appropriately to their AFM sublattice (red and blue), lie in the {111} easy planes.

action energy becomes smallest, when the magnetization is locally aligned with the edges of the sample, such that stray fields are minimized. As a result from the competition between the exchange interaction and the magnetostatic interaction, vortex states naturally appear in FMs. At the vortex center the FM magnetization points out of the sample plane. We assume that the FM magnetization stays in the vortex state and from now on only consider the AFM. The AFM energy density is given by

$$w_{\mathrm{AFM}} = \left(\frac{1}{2} A_{\mathrm{AFM}} (\nabla \mathbf{n})^2 + \frac{1}{2} K_{\mathrm{AFM}} n_z^2\right) t_{\mathrm{AFM}} - J_{\mathrm{coup}}\, \mathbf{m} \cdot \mathbf{n}, \tag{3.1}$$

where A_{AFM} is the magnetic stiffness, K_{AFM} is the AFM easy (111) plane anisotropy, t_{AFM} is the AFM layer thickness, $\mathbf{n}$ is the Néel vector and $\mathbf{m}$ is given by the structure of the underlying FM vortex.

For now we concentrate on the equilibrium position of the AFM Néel vector near the vortex center. The vortex has radial symmetry in the plane. Thus, we can parametrize the Néel vector in polar coordinates, such that θ is the out-of-plane angle. The energy density simplifies to

$$w_{\mathrm{AFM}} = \frac{1}{2} K_{\mathrm{AFM}}\, t_{\mathrm{AFM}} \cos^2\theta - J_{\mathrm{coup}}\, M_{\mathrm{FM}} \cos\theta, \tag{3.2}$$

where M_{FM} is the FM saturation magnetization. Minimization of the energy den-

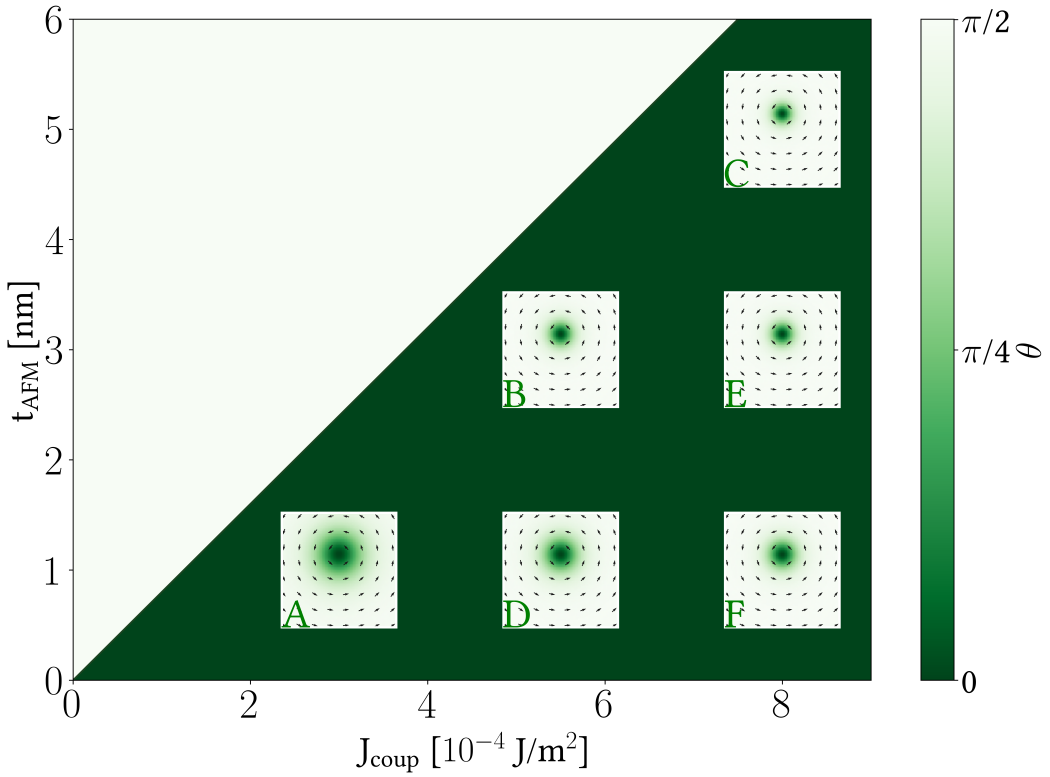

Figure 3.4: Phase diagram for the in-plane AFM that is coupled to a FM vortex texture. The data was obtained through analytical calculations. The color bar shows the Néel vector out-of-plane angle θ. Insets show the n_z component in color and the in-plane Néel vector orientation with arrows from micromagnetic simulations of the imprinted AFM vortex state. The location of the insets in the space of parameters correlates to the material parameters used for each simulation, see Appendix A.1.1.

sity yields two solutions: $\theta = 0$ for $J_{\text{coup}} < K_{\text{AFM}}\, t_{\text{AFM}}$ and $\theta = \pi/2$ for $J_{\text{coup}} > K_{\text{AFM}}\, t_{\text{AFM}}$. We identify the AFM layer thickness as an experimentally accessible parameter to effectively alter the AFM out-of-plane anisotropy. Thus, we map the space of parameters of the AFM ground state, spanned by the AFM layer thickness t_{AFM} and the interface exchange coupling J_{coup} in Fig. 3.4. For the calculation of the phase diagram we use the out-of-plane anisotropy of NiO $K_{\text{AFM}} = 1.25 \times 10^5\,\text{J m}^{-3}$ for an AFM layer thickness of $t_{\text{AFM}} = 4\,\text{nm}$ ($K_{\text{AFM}} = 5 \times 10^5\,\text{J m}^{-3}$ for $t_{\text{AFM}} = 1\,\text{nm}$) [121]. Please refer to Tab. 3.1 in the next section for more details on the magnetic parameters in our calculations.

In the phase diagram Fig. 3.4 we can observe two distinct phases. For large AFM layer thickness, the AFM anisotropy dominates and the Néel vector lies in-plane,

$\theta = 0$. We call this phase the anisotropy-dominated phase, shown in white in Fig. 3.4. However, if the interface exchange coupling strength energy is larger than the anisotropy energy, the AFM transitions into the interface exchange-dominated phase, as shown in green in Fig. 3.4. Accordingly, the Néel vector assumes alignment with the FM magnetization, $\theta = \pi/2$. With increasing AFM layer thickness the relative influence of the AFM anisotropy on the AFM ground state increases and the Néel vector prevails in-plane for larger interface exchange coupling strengths. Accordingly, we observe the phase transition point at $K_{\mathrm{AFM}} \cdot t_{\mathrm{AFM}} \approx J_{\mathrm{coup}}$. For a 4 nm thick AFM layer we calculate a critical interface exchange coupling strength of $J_{\mathrm{coup}} \gtrsim 6 \times 10^{-4}\,\mathrm{J\,m^{-2}}$. We conclude that the transition from the uncoupled AFM to the imprinted phase is mainly determined by the interface exchange coupling strength and the influence of the AFM anisotropy, weighted by the AFM layer thickness.
The insets in Fig. 3.4 show the imprinted AFM vortex state. Each inset was positioned according to the values of the AFM anisotropy and the interface exchange coupling used in the respective micromagnetic simulation. How these micromagnetic simulations were performed and which insights into the stabilization of the imprinted AFM vortex state were gained is subject of the following section.

3.2 Stabilization of Antiferromagnetic Vortex States

In the previous section we used a phenomenological model to characterize the influence of interface exchange coupling on the AFM ground state. In the next step, we would like to look at the full texture of the imprinted vortex state. The tool we employ for this approach is numerical: a micromagnetic simulation.
We aim to investigate the stability of the vortex state in the AFM layer by iteratively varying the effective AFM anisotropy[2] and the interlayer exchange coupling strength and in each case determining the state of the AFM Néel vector. Additionally, we repeat our study for various system sizes in order to stabilize more than one imprinted vortex. For our micromagnetic simulations we use the open source micromagnetic software Mumax[3] [89, 122]. We model the bilayer system as two layers of dimension 128 nm × 128 nm × 1 nm each (for the single vortex case; other cases will be discussed later). The system is discretized with a mesh size

[2]The AFM out-of-plane anisotropy's influence on the bilayer is weighted by the AFM layer thickness. Instead of varying the thickness of the simulated layer, we vary the effective anisotropy constant.

of 1 nm × 1 nm × 1 nm [3] and the boundary conditions are open. For the bottom, FM layer we include the exchange interaction energy (exchange stiffness A_{FM}), demagnetization energy and in-plane uniaxial anisotropy (anisotropy constant K_{FM}). For the AFM layer we include the exchange interaction energy (exchange stiffness A_{AFM}) and in plane uniaxial anisotropy (anisotropy constant K_{AFM}). The two layers couple via interface exchange coupling, which is of the form $J_{\mathrm{coup}}\,\mathbf{m}\cdot\mathbf{n}$, where J_{coup} is the interface exchange coupling, $\mathbf{m}$ is the FM magnetization and $\mathbf{n}$ is the AFM Néel vector. The material and simulation parameters are given in Tab. 3.1 and the Mumax[3] code is given in Appendix A.1.2.

Table 3.1: Values of the micromagnetic parameters and other conditions utilized in the simulations. Note, that the implementation of the out-of-plane anisotropy in Mumax[3] uses the opposite sign from this work. The AFM out-of-plane anisotropy is given for an AFM layer thickness of $t_{\mathrm{AFM}} = 1\,\mathrm{nm}$.

Boundary Conditions	open
Damping	0.01
Demagnetization	FM layer only
Saturation Magnetization (both M_{AFM} and M_{FM})	$5.00 \cdot 10^6$ A/m [121]
Exchange Stiffness (both A_{AFM} and A_{FM})	$2.10 \cdot 10^{-11}$ J/m [121, 123]
Fe out-of-plane anisotropy K_{FM}	$1.25 \cdot 10^5$ J/m^3 [124]
NiO out-of-plane anisotropy K_{AFM}	$5.00 \cdot 10^5$ J/m^3 [121]

We carry out two steps in order to obtain imprinted AFM vortex states. First, we only consider the FM layer and choose a vortex-like magnetization texture as the initial state, as shown in Fig. 3.5. The magnetization is arranged into four triangular domains, such that the domain boundaries form diagonal lines in the xy plane of our system, as we show in Fig. 3.5. For the leftmost vortex, the top domain's magnetization points along -x, in the bottom one along +x, in the left one along -y and in the right one along +y. At the center of the sample, where the domain boundaries cross, we add a circular domain of radius 5 nm, in which the magnetization is oriented along +z. We alternate the sense of rotation for neighboring vortices in accordance with out experimental observations in Sec. 3.4. The magnetization is homogeneous along the z axis throughout the system.

Then we minimize the energy of the FM layer using the *relax()* and *minimize()*

[3] For simulations that were used for visualizations, a mesh size of 0.5 nm × 0.5 nm × 0.5 nm was used.

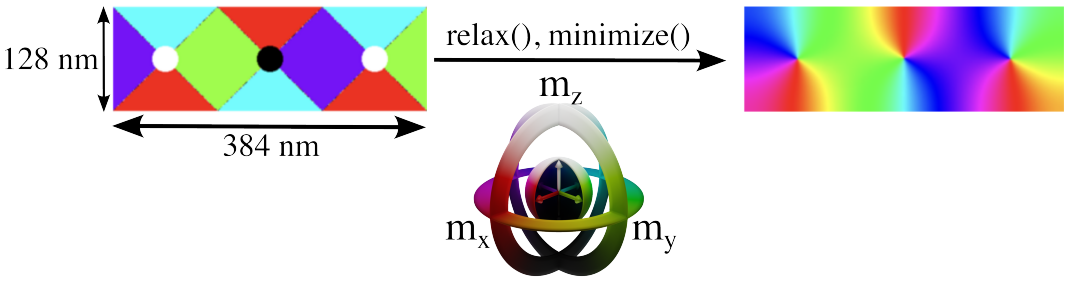

Figure 3.5: Micromagnetic FM initial and final state. The magnetization direction is encoded in color, as depicted in the color diagram (adapted from [80, 81]).

functions provided by Mumax[3]. The magnetization relaxes into a vortex texture. We obtain similar results for initializing the magnetization in a vortex pattern given by Mumax[3] and subsequently minimizing the energy.
In the second step we fix the FM magnetization in its vortex texture and add the AFM layer. In equilibrium, a compensated AFM does not produce any net magnetization. Thus, the sublattice magnetization and the Néel vector can be treated as equal entities. We initialize the Néel vector to point along +x throughout the AFM layer. This conforms to the ground state of an easy-plane AFM. For a strong enough interface exchange coupling to the FM magnetization, the AFM Néel vector transitions from its easy-plane ground state, which we called the anisotropy-dominated phase in our phenomenological considerations, into a mapping of the FM vortex structure, the interface exchange-dominated phase. A visualization of the imprinted state from our micromagnetic simulations is shown in Fig. 3.6.

In the previous section we concluded that the stability of the interface exchange dominated phase is determined by the interplay of the interface exchange coupling strength and the AFM anisotropy, that is weighted by the AFM layer thickness. By iteratively changing the interface exchange coupling strength and the AFM thickness (effective anisotropy) and repeating the above micromagnetic simulations we probe for the critical coupling strength at which the AFM vortex imprinting becomes stable. We define a stable imprinting by two criteria: The out-of-plane Néel vector at the center of the AFM vortex should point into the same direction as the out-of-plane magnetization of the FM vortex. Furthermore, we check the topological charge of the vortex structure by applying

$$q = \frac{1}{4\pi} \int \mathbf{n} \cdot \left(\frac{\partial \mathbf{n}}{\partial x} \times \frac{\partial \mathbf{n}}{\partial y} \right) \mathrm{d}x\, \mathrm{d}y, \tag{3.3}$$

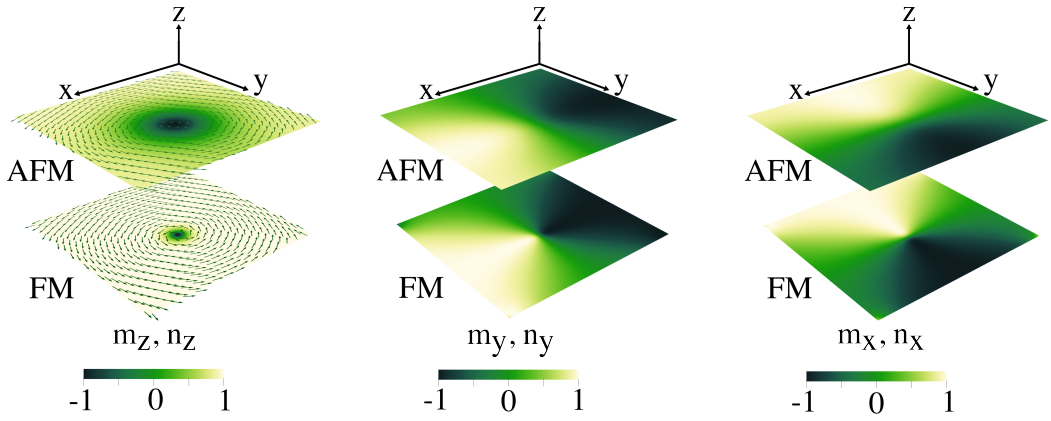

Figure 3.6: Micromagnetic simulation [89, 122] of AFM-FM vortex imprinting. The system is comprised of two layers with dimensions 128 nm × 128 nm × 1 nm each. In the left column, the out-of-plane components are shown in color, while the in-plane components are shown with arrows. In the center and right column the in-plane components are shown in color as indicated.

where q is the topological charge and $\mathbf{n}$ is the Néel vector field. The vortex has topological charge 1/2. These two criteria enable the numerical classification of a stable imprinting in our simulations.
In Fig. 3.7 we present the results from our micromagnetic simulations. The data points indicate the critical interface exchange coupling for which stable imprinting of the AFM vortex state has been reached. Thereby, the area above the linear fit lines corresponds to the anisotropy-dominated phase, and below lies the interface exchange-dominated phase, in which we observe the imprinting of the vortex states. A vortex has cylindrical symmetry and, thus, we use a square sample. When we connect multiple square areas into a rectangle, more than one vortex can be stabilized. We stabilize and imprint one, two, three, four and five vortices, arranged side-by-side. We repeat the mapping of the phase space for each number of vortices. In each case we aim for an imprinting of all vortices into the AFM layer. In accordance with topology, the out-of-plane component of the vortex texture alternates between neighboring vortices.

In Fig. 3.7 we find that the critical interface exchange coupling strength has a linear dependence on the AFM layer thickness. The phase transition happens when the effective AFM anisotropy energy is roughly equal to the interface exchange coupling energy. This result is in agreement with our phenomenological model. Furthermore, the stability of the imprinted state does not depend on the

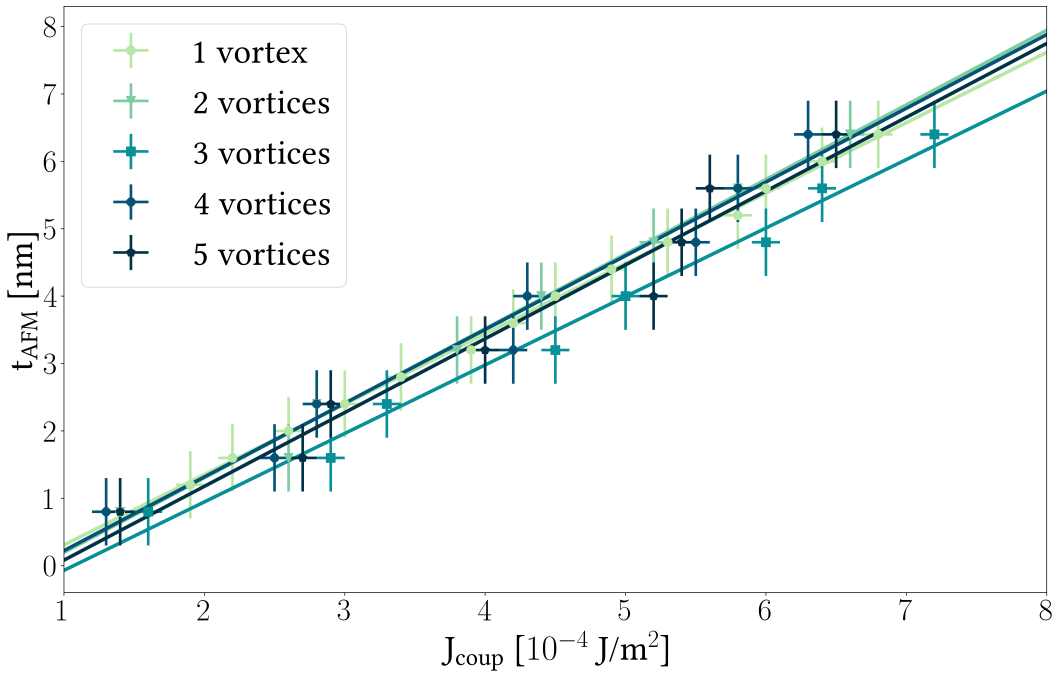

Figure 3.7: AFM phase diagram for the imprinting of multiple vortices. The AFM layer thickness t_{AFM} and interface exchange coupling J_{coup} are the model parameters that determine the state of the AFM. Each data set represents a micromagnetic simulation with the number of imprinted vortices as indicated. The stability area of the imprinted AFM vortex states lies below the lines. More details on the the simulations can be found in Appendix A.1.2.

number of imprinted vortices.

Interestingly, the vortex core size in the AFM and the FM are different, cf. Fig. 3.8. Thus, there is a local mismatch between the FM magnetization and the AFM Néel vector despite the direct coupling by interface exchange. In the next section we develop a phenomenological model to find the cause of this effect.

3.3 Properties of the Imprinted Antiferromagnetic Vortex State

We define the region of a vortex, in which the spins possess an out-of-plane component, as the vortex core. It can be interpreted as the two-dimensional version of the DW width in the sense that it provides a characteristic length scale for the system. In order to analyze the size variation of the vortex core, we return to our phenomenological model Eqn. 3.1

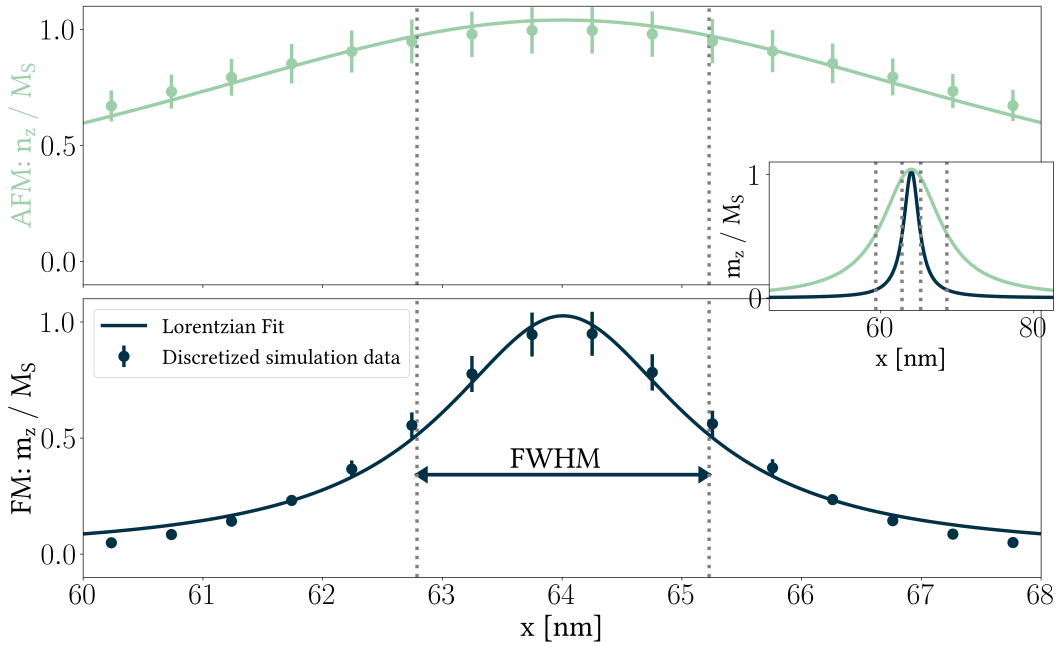

Figure 3.8: Vortex profiles. The top panel depicts the AFM Néel vector component n_z profile along the in-plane direction x. The bottom panel shows the same for the magnetization component m_z. All data points were fitted with a Lorentzian function and the full width half maximum is shown. The inset shows a larger range along x, such that the overall size of the AFM and FM vortex structures can be compared. Details on the simulations can be found in Appendix A.1.2.

$$w_{\mathrm{AFM}} = \left(\frac{1}{2} A_{\mathrm{AFM}} (\nabla \mathbf{n})^2 + \frac{1}{2} K_{\mathrm{AFM}} n_z^2\right) t_{\mathrm{AFM}} - J_{\mathrm{coup}} \mathbf{m} \cdot \mathbf{n}. \tag{3.4}$$

The vortex has an in-plane rotational symmetry in real space. That allows us to rewrite the problem as a 2D problem in spin space, that upon energy minimization in the Euler-Lagrange-formalism will yield a 1D solution.
The Néel vector in real space is parametrized by

$$\mathbf{n}_{\mathrm{real}} = n_x \hat{\mathbf{x}} + n_y \hat{\mathbf{y}} + n_z \hat{\mathbf{z}}, \tag{3.5}$$

where a hat signifies a unit vector. We can define the Néel vector in the spin space by its radial and out-of-plane component only

$$\mathbf{n}_{\mathrm{Néel}} = n_\rho \hat{\boldsymbol{\rho}} + n_z \hat{\mathbf{z}}, \tag{3.6}$$

where ρ is the radial part, such that

$$
\begin{aligned}
n_x &= n_\rho \cos\phi, \\
n_y &= n_\rho \sin\phi, \\
n_\rho &= \sin\theta, \\
n_z &= \cos\theta.
\end{aligned}
\tag{3.7}
$$

ϕ is the in-plane angle of the Néel vector. The solution for the Néel vector will be independent from ϕ. $\theta(\rho)$ is the out-of-plane angle of the Néel vector and depends on the radius from the center of the vortex. The parametrization yields the following differentials

$$
\frac{\mathrm{d}f}{\mathrm{d}x} = \frac{\partial f}{\partial \rho}\frac{\partial \rho}{\partial x} + \frac{\partial f}{\partial \phi}\frac{\partial \phi}{\partial x} = \cos\phi \frac{\partial f}{\partial \rho} - \frac{\sin\phi}{\rho}\frac{\partial f}{\partial \phi}, \tag{3.8}
$$

$$
\frac{\mathrm{d}f}{\mathrm{d}y} = \frac{\partial f}{\partial \rho}\frac{\partial \rho}{\partial y} + \frac{\partial f}{\partial \phi}\frac{\partial \phi}{\partial y} = \sin\phi \frac{\partial f}{\partial \rho} + \frac{\cos\phi}{\rho}\frac{\partial f}{\partial \phi}, \tag{3.9}
$$

where f is a trial function. The application of the parametrization on the exchange term of the energy density gives

$$
\begin{aligned}
(\nabla \mathbf{n})^2 &= (\nabla n_x)^2 + (\nabla n_y)^2 + (\nabla n_z)^2, \\
&= \left(\frac{\partial}{\partial \rho}\sin\theta\cos\phi\,\hat{\boldsymbol{\rho}} + \frac{1}{\rho}\frac{\partial}{\partial \phi}\sin\theta\cos\phi\,\hat{\boldsymbol{\phi}} + \frac{\partial}{\partial z}\sin\theta\cos\phi\,\hat{\mathbf{z}}\right)^2 \\
&+ \left(\frac{\partial}{\partial \rho}\sin\theta\sin\phi\,\hat{\boldsymbol{\rho}} + \frac{1}{\rho}\frac{\partial}{\partial \phi}\sin\theta\sin\phi\,\hat{\boldsymbol{\phi}} + \frac{\partial}{\partial z}\sin\theta\sin\phi\,\hat{\mathbf{z}}\right)^2 \\
&+ \left(\frac{\partial}{\partial \rho}\cos\theta\,\hat{\boldsymbol{\rho}} + \frac{1}{\rho}\frac{\partial}{\partial \phi}\cos\theta\,\hat{\boldsymbol{\phi}} + \frac{\partial}{\partial z}\cos\theta\,\hat{\mathbf{z}}\right)^2, \\
&= \left(\cos\theta\frac{\partial\theta}{\partial\rho}\cos\phi\,\hat{\boldsymbol{\rho}} + \frac{1}{\rho}\sin\theta(-\sin\phi)\,\hat{\boldsymbol{\phi}}\right)^2 \\
&+ \left(\cos\theta\frac{\partial\theta}{\partial\rho}\sin\phi\,\hat{\boldsymbol{\rho}} + \frac{1}{\rho}\sin\theta\cos\phi\,\hat{\boldsymbol{\phi}}\right)^2 \\
&+ \left(-\sin\theta\frac{\partial\theta}{\partial\rho}\,\hat{\boldsymbol{\rho}}\right)^2, \\
&= \cos^2\theta\left(\frac{\partial\theta}{\partial\rho}\right)^2\cos^2\phi
\end{aligned}
\tag{3.10}
$$

$$+\frac{1}{\rho^2}\,\sin^2\theta\,\sin^2\phi\,+\,\cos^2\theta\left(\frac{\partial\theta}{\partial\rho}\right)^2\sin^2\phi\,+\,\frac{1}{\rho^2}\,\sin^2\theta\,\cos^2\phi\,+\,\sin^2\theta\left(\frac{\partial\theta}{\partial\rho}\right)^2,$$
$$=\left(\frac{\partial\theta}{\partial\rho}\right)^2+\frac{1}{\rho^2}\,\sin^2\theta.$$

Eqn. 3.4 thus reads

$$w_{\mathrm{AFM}} = \frac{1}{2}\,A_{\mathrm{AFM}}\,t_{\mathrm{AFM}}\left(\left(\frac{\partial\theta}{\partial\rho}\right)^2+\frac{1}{\rho^2}\,\sin^2\theta\right)+\frac{1}{2}\,K_{\mathrm{AFM}}\,t_{\mathrm{AFM}}\,\cos^2\theta \tag{3.11}$$
$$-J_{\mathrm{coup}}\,(\sin\theta\,\cos\phi\,\sin\theta_{\mathrm{FM}}\,\cos\phi\,+\,\sin\theta\,\sin\phi\,\sin\theta_{\mathrm{FM}}\,\sin\phi\,+\cos\theta\,\cos\theta_{\mathrm{FM}}),$$

where θ_{FM} is the FM magnetization's out-of-plane angle. The contributions of magnetostatic interactions and the variation in the anisotropy strength and between the FM and the AFM change only the out-of-plane components of the order parameters. Thus, the in-plane angle ϕ of the FM magnetization and the AFM Néel vector is the same. In our calculations, we constrain the mismatch between the two order parameters to the out-of-plane component.
We will now calculate the functional derivative, where $\theta(\rho)$ is our generalized coordinate

$$\frac{\partial\mathcal{L}}{\partial\theta}-\frac{\mathrm{d}}{\mathrm{d}\rho}\,\frac{\partial\mathcal{L}}{\partial\theta'}\,=\,0. \tag{3.12}$$

That the Lagrange function in spin space is defined as

$$\mathcal{L}\,=\,\int w_{\mathrm{AFM}}\,\rho\,\mathrm{d}\rho\,\mathrm{d}\phi\,\mathrm{d}z, \tag{3.13}$$

where we have taken the Jacobian determinant ρ for the transformation from real into spin space into consideration. For the equation of motion we obtain

$$-x_{\mathrm{DW}}^2\,\frac{1}{\rho}\,\frac{\partial}{\partial\rho}\left(\rho\,\frac{\partial\theta}{\partial\rho}\right)+\left(-1\,+\,\frac{x_{\mathrm{DW}}^2}{\rho^2}\right)\sin\theta\,\cos\theta\,+\,h_{\mathrm{eff}}\,\sin(\theta\,-\,\theta_{\mathrm{FM}})\,=\,0, \tag{3.14}$$

where $x_{\mathrm{DW}}\,:=\,\sqrt{A_{\mathrm{AFM}}/K_{\mathrm{AFM}}}$ is the DW in the isolated AFM layer and $h_{\mathrm{eff}}\,:=\,J_{\mathrm{coup}}/(K_{\mathrm{AFM}}\,t_{\mathrm{AFM}})$ is an effective field in dimensionless units induced by the interface exchange coupling to the underlying FM layer.
Far away from the vortex center ($\rho\,\gg\,x_{\mathrm{DW}}$) the FM magnetization lies in-plane

$\theta_{\mathrm{FM}} = \pi/2$. Then, Eqn. 3.14 can be approximated as $(\sin\theta + h_{\mathrm{eff}})\cos\theta = 0$. For the AFM Néel vector we obtain the solution $\theta = \pi/2$ or $\theta = \pi + \arcsin(h_{\mathrm{eff}})$ (the second solution is not valid as $h_{\mathrm{eff}} > 0$ and θ is only defined from 0 to π); hence, the Néel vector also lies in-plane, as expected. Close to the vortex center ($\rho \ll x_{\mathrm{DW}}$), the FM magnetization points out-of-plane $\theta_{\mathrm{FM}} \to 0$, and also the AFM Néel vector is largely out-of-plane $\theta \ll 1$. For small θ we can expand $\sin\theta\ \cos\theta \approx \theta$. In order to find a solution for Eqn. (3.14) we insert the ansatz $\theta \sim \rho^n$ and regroup the terms

$$\left(-n^2\,\frac{x_{\mathrm{DW}}^2}{\rho^2} + \frac{x_{\mathrm{DW}}^2}{\rho^2}\right)\theta + (h_{\mathrm{eff}} - 1)\,\sin\theta = 0. \tag{3.15}$$

While the first two terms cancel for $n = 1$, the last two terms determine the stability of the solution. We obtain a stable vortex state for $h_{\mathrm{eff}} > 1$. As we defined $h_{\mathrm{eff}} := J_{\mathrm{coup}}/(K_{\mathrm{AFM}}\,t_{\mathrm{AFM}})$, we associate the effective AFM anisotropy with $K_{\mathrm{an}} := J_{\mathrm{coup}}/t_{\mathrm{AFM}} - K_{\mathrm{AFM}}$. This effective AFM anisotropy introduces a modification to the magnetocrystalline anisotropy of the AFM material by an additional term that stems from the interface exchange coupling. Such a modification then also leads to a change in the characteristic length scale and thus the vortex core size. To summarize: The vortex core size is individually determined in each layer by the intrinsic properties of the material, just we discussed for the case of a DW in Sec. 2.3.2. For example, a stronger AFM anisotropy or a thicker AFM layer leads to a smaller vortex core size. Additionally, the interface exchange coupling modifies the characteristic size of the AFM vortex core. Below we will see that for stronger interface exchange coupling the AFM vortex core size approaches the FM vortex core size.

As we previously noted from Figs. 3.4 and 3.7, close to the critical interface exchange coupling strength $K_{\mathrm{AFM}}\cdot t_{\mathrm{AFM}} \approx J_{\mathrm{coup}}$ holds true. In the interface exchange-dominated phase $K_{\mathrm{AFM}}\cdot t_{\mathrm{AFM}} < J_{\mathrm{coup}}$. For increasing J_{coup} the effective anisotropy K_{an} increases. As a consequence, the vortex core size $x_{\mathrm{core}} \sim 1/\sqrt{K_{\mathrm{an}}}$ decreases. We have seen before, that the vortex core size in the FM is smaller compared to the AFM vortex core size for the given material parameters. Hence stronger interface exchange coupling reduces the difference between the AFM vortex core size and the FM vortex core size. We will use this result to analyze our micromagnetic simulation results below.

In order to analyze the size of the vortex core, we fit a Lorentzian function to the m_z magnetization profile as shown in Fig. 3.8. For our purposes we take the full width half maximum of the Lorentzian fit function for the vortex core size. For a

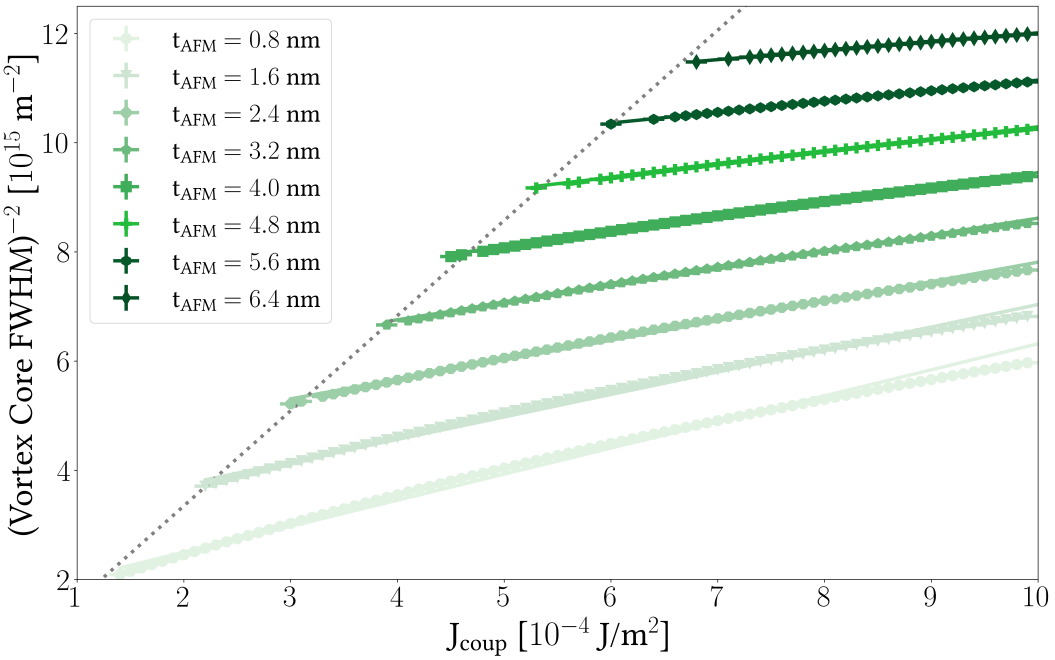

Figure 3.9: Scaling of the vortex core size with the interface coupling strength for different AFM layer thicknesses.

4 nm thick AFM layer we calculate a vortex core size of 9 nm for a sample size of 128 nm × 128 nm × 1 nm. Fig. 3.9 shows how the vortex core size changes throughout the phase diagram[4]. In agreement with our phenomenological calculation, the critical interface exchange coupling increases with increasing AFM layer thickness. Moreover, the vortex core size decreases for increasing interface exchange coupling strength, as we expected. We fitted the data points with linear functions, corresponding to $1/x^2_{\text{core}}(J_{\text{coup}}) = 1/(A_{\text{AFM}}t_{\text{AFM}}) \cdot J_{\text{coup}} - K_{\text{AFM}}/A_{\text{AFM}}$. Close to the phase transition point, where our approximations are valid, we find a good fit to the data.
With these theoretical considerations in mind, we turn ourselves towards the experimental realization of imprinted AFM vortex states, which will be discussed in the next section.

3.4 Comparison to Experimental Data

In the following section we present the experimental realization of imprinted AFM vortex states in NiO(111) (4 nm) - Fe (110) (6 nm) as obtained by our collaborators

[4]The data in Fig. 3.9 has been transformed, such that a linear function could be fitted. For ease of qualitative interpretation we provide a plot of the untransformed data in Fig. A.1 in the Appendix A.1.3.

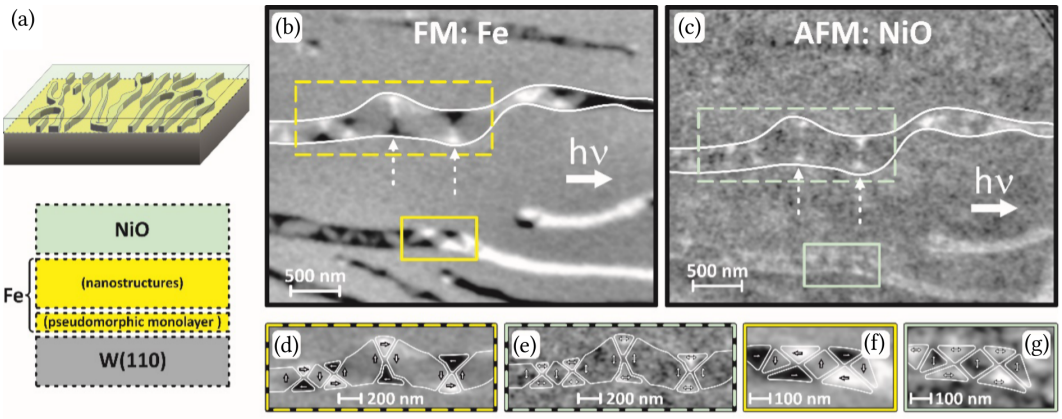

Figure 3.10: Experimental results. (a) Sample setup. (b), (c) XMCD- and XMLD-PEEM images of NiO-Fe nanostructures. The white dashed arrows indicate two of the magnetic vortices within the central nanostructure. Two yellow (b) and green (c) dashed and solid rectangles mark regions selected for magnification shown in (d)-(g) White and black arrows schematically depict the local in-plane orientation of magnetic moments in Fe and double arrows for the Néel vector for NiO vortices, respectively.

Dr. Michal Ślezak, Dr. Anna Koziol-Rachwal and Prof. Dr. Tomasz Ślezak from the AGH University of Krakow in Poland.

The main result from their experimental work is shown in Fig. 3.10. Panel (a). shows the structure of the sample. They prepared the sample by growing eight continuous monolayers of Fe (110) by molecular beam epitaxy on a single crystal W (110) substrate at room temperature. Subsequently, they post annealed the iron at 800 K such that self-organized Fe nanostructures remain on top of a Fe monolayer. The nanostructures are several hundred nano meters long and > 6 nm high. The areas between the Fe nanostructures are again covered using pseudomorphic Fe. They deposited the AFM NiO (111) layer on top by reactive vapor deposition of Ni in a partial Oxygen atmosphere of 1×10^6 mbar.

In Fig. 3.10 b-g the magnetic texture of both the FM and AFM components of NiO-Fe nanostructures are imaged using PEEM combined with X ray magnetic circular and linear dichroism (XMCD and XMLD) techniques. In Fig. 3.10 (b) and (c), we present XMCD- and XMLD-PEEM images of selected $4\,\mu m \times 2.5\,\mu m$ regions, that showcase the general magnetic configuration in NiO-Fe islands [5]. In the XMCD im-

[5]XMCD was performed at the L_3-edge of Fe ($\approx$ 700 eV photon energy) and XMLD at the L_2-edges of Ni (868.9 eV and 870.2 eV photon energy). Both experiments were conducted at 120 K at the spectroscopic photoemission and low energy electron microscope (SPELEEM) at the end station of the nanospectroscopy beamline at the Elettra synchrotron (Trieste, Italy).

age (Fig. 3.10 (b)) we observe elongated Fe nanostructures surrounded by the pseudomorphic Fe monolayer that covers the W substrate. The nanostructure regions with in-plane easy-axis orthogonal to the propagation direction of the incoming radiation appear in neutral gray, since no magnetic contrast arises in such a configuration. The white and black areas correspond to local magnetization vectors parallel or antiparallel to the in-plane beam propagation direction, respectively. Two yellow, dashed and solid rectangles in Fig. 3.10 (b) mark the regions where the narrow nanostructure hosts multiple FM vortex states along its longitudinal axis. Such magnetic vortex structures are directly imprinted into the AFM NiO, as seen in the corresponding XMLD image presented in Fig. 3.10 (c), where the analyzed vortices are marked by dashed and solid rectangles. In Fig. 3.10 (d)-(g), these regions are magnified. In these images white arrows and black double arrows schematically depict the local spin structure in Fe and NiO sublayers, respectively. The local orientation of the spin structure reveals an alternating sense of rotation for neighboring vortices. XMLD is not selective with regard to parallel or antiparallel directions of the in-plane Néel vector. Only the Néel vector axes aligned with and orthogonal to the incident radiation axis produce contrast. Thus, instead of three distinct intensity levels, corresponding to antiparallel, parallel and orthogonal alignment between the magnetization and photon polarization vectors, only two are observed in the AFM layer.
In principle, the in-plane magnetic domain structures imaged by PEEM make the identification of vortex states possible, but the limited spatial resolution of 30 – 50 nm does not allow us to visualize the vortex structure in detail.
The computed spin structures that we presented in the previous sections not only reproduce well the experimental distribution of the in-plane magnetization and Néel vector components (Fig. 3.10 (f), (g) but also prove the presence of the out-of-plane magnetic moments around the vortex center with alternating spin orientation for adjacent vortices that is accompanied by the opposite sense of rotation of the in-plane spin texture, in perfect agreement with experimental data.

3.5 Conclusion

In conclusion, we demonstrated the stabilization of topological vortex textures in the in-plane AFM NiO(111) at zero external magnetic fields.
Our analytical calculations revealed that interface exchange coupling between the AFM and the FM layers causes the Néel vector to align with the FM magnetization at the vortex center. Our micromagnetic simulations demonstrated that the stabil-

ity of such vortex states can be tuned by the AFM layer thickness. We constructed a phase diagram that takes into account the interplay between interface exchange coupling and the AFM layer thickness. The phase diagram remained consistent regardless of the number of imprinted vortices.

We found that the minimal interface exchange coupling strength required to transition into the stable AFM vortex state phase increases with AFM layer thickness. Specifically, for an AFM layer thickness of 4 nm, as studied in our experiments, we calculated the minimum critical interface exchange coupling $J_{\mathrm{coup}} \gtrsim 6 \times 10^{-4}\,\mathrm{J\,m^{-2}}$. Moreover, depending on the AFM layer thickness and interface exchange coupling strength we predict possible significant differences between the AFM and FM vortex core sizes. We found good agreement of our theoretical results with the experimental measurements of our collaborators. Our results indicate the exciting possibility of inducing localized out-of-(111)-plane AFM moments in the well-known in-plane AFM NiO(111) system.

4 Interface-Exchange Coupling of Spin Dynamics in Mn_2Au-Py

In this chapter we explore the coupled magnetization statics and dynamics of Mn_2Au-$Ni_{80}Fe_{20}$ (Py, Permalloy) thin film hybrids. Our phenomenological model reveals that interface exchange coupling in Mn_2Au-Py causes an imprinting of the AFM domain texture on the FM layer. As a consequence, the magnetization in the FM locally aligns in parallel with the AFM Néel vector. We show this alignment not only analytically, but also using atomistic spin simulations. We find that interface exchange coupling leads to coupled spin dynamics in Mn_2Au-Py and a frequency enhancement and a frequency splitting of the FM resonance (FMR) mode in the Py. Changing of the FM layer thickness enables control over the FMR frequency and dispersion of Py. We report good agreement of our results with experimental data from FMR and BLS experiments on Mn_2Au-Py thin films. In combination with these experimental results our model allows for the independent estimation of the interface exchange coupling strength to 1.6 Tnm and the study of AFM magnon frequencies without the need for THz spectroscopy. Moreover, we consider the coupled DW motion in Mn_2Au-Py. Our atomistic spin dynamics simulations demonstrate that DW motion can be initiated by acting on the FM magnetization with magnetic fields. We find a high limiting DW velocity of 8.5 km/s. We conclude that interface exchange coupling enables the controlled manipulation of coupled DWs and thereby the AFM Néel vector. [1]

[1] The following chapter and its sections have been transcribed from [88, 126] and its supplementary material, with the second author of these references being the author of this thesis. Individual

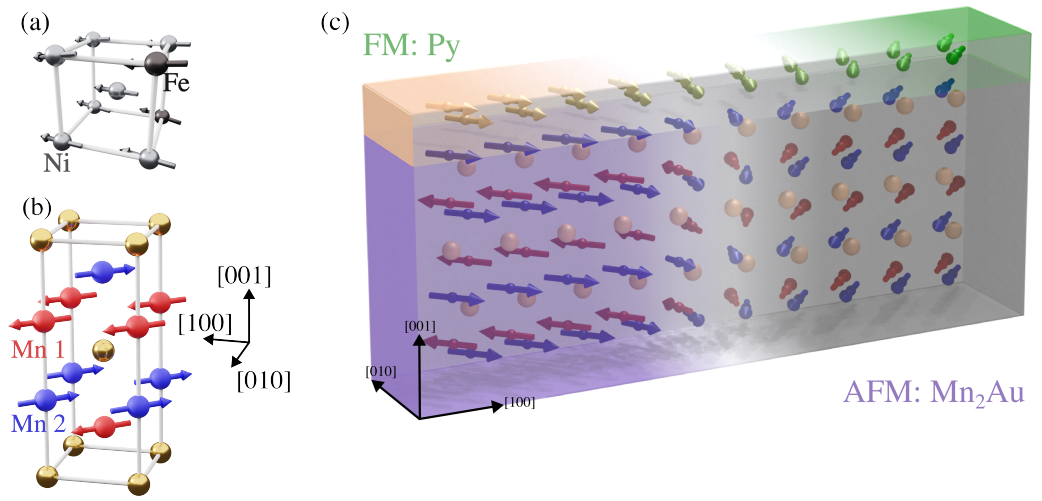

Figure 4.1: Mn_2Au-Py model system. (a), (b) Visualization of the unit cells of bcc-Py and Mn_2Au [125]. (c) Visualization of the Mn_2Au-Py hybrid system [86].

In order to harvest the advantages of FMs, e.g. manipulability, and of AFMs, speed and robustness, they can be combined in hybrid bilayer systems. We study FM and AFM materials in hybrid systems that are coupled by interface exchange coupling. The FM component facilitates magnetic control and manipulation, while the AFM material is integrated for high-frequency and ultra-fast dynamics. The key advantage of this approach is that the readout of the magnetic signal is facilitated via the FM, using conventional techniques.
In such an application, the fundamental challenge is the manipulation of the Néel vector. We consider an applied field that manipulates the FM magnetization, which in turn acts on the AFM Néel vector through interface exchange coupling. Another important approach, which we do not consider in this work, is to apply short current pulses that induce Néel spin-orbit torques (NSOTs) in the AFM. As NSOTs manipulate the Néel vector [56, 127], the FM magnetization follows coherently through interface exchange coupling [86, 88, 126].
NSOTs can be generated at interfaces with heavy metals or directly in the bulk of a metallic AFM [128, 129]. CuMnAs and Mn_2Au are two AFM materials that exhibit the required crystallographic and magnetic structure in combination with strong spin-orbit-coupling, such that a bulk NSOT can act on the Néel vector [106, 129–131]. However, Mn_2Au is better suited for spintronic applications due to its metallic conductivity. Additionally, its high Néel temperature, moderate magnetocrys-

contributions are detailed in Appendix B.1. The Bachelor thesis of Martin Münzenberg was supervised by the author of this thesis as part of this project.

talline anisotropy and large coercive field (5000 Oe in Mn_2Au-Py [86] compared to Fe-CuMnAs 200 Oe [132]) leads to long-term room-temperature stability of the Néel ordered state [86, 129]. NSOT switching of the Néel vector has been theoretically simulated [133] and experimentally shown for Mn_2Au [129, 134, 135]. Therefore, we choose the Mn_2Au-Py material system.

This system is special among AFM-FM hybrids, as it has a well defined surface termination [86]: The Py layer is polycrystalline, but due to termination requirements we can assume a bcc ordering near the interface [86, 126], which we show in Fig. 4.1 (a). Mn_2Au has a tetragonal crystal structure in which the ferromagnetically ordered sublattices are stacked in layers along the z axis, as shown in Fig. 4.1 (b). When Py is deposited atop the Mn_2Au layer, the easy-plane AFM terminates such that the atoms at the interface all belong to the same sublattice. Hence, the Py interface atoms couple directly to Mn_2Au atoms of only one sublattice, which enables an especially strong coupling. The system exhibits no exchange bias [86], but the FM magnetization and the AFM Néel vector align in parallel, as shown in Fig. 4.1 (c). This alignment prevails even when magnetic fields reorient the FM magnetization: Fields as low as $O(1\,\mathrm{T})$ achieve magnetic control over the AFM Néel vector at room temperature, while pure Mn_2Au remains field-stable up to 30 T [86, 134].

While interface exchange coupling alters the magnetic state in an AFM-FM system, it can also have significant influence on the magnetization dynamics. The FM spin wave dispersion in the GHz regime can be modified by interface exchange coupling in FM-FM, chiral FM-FM and AFM-FM heterostructures [88]. Experiments have shown that the magnetization dynamics in Mn_2Au are complex [134]. Both NSOTs and thermal effects can contribute to the change of orientation of the Néel vector. However, it was also shown that in the hybrid system the interface exchange coupling is very strong [86, 88]. Since we consider the magnetization dynamics only in the case of an applied magnetic field, we can neglect other interface effects.

But how can the THz magnons of AFM influence hybrid spin wave modes in AFM-FM hybrids? Can interface exchange coupling be used to leverage control over the spin wave dispersion of hybrid spin wave modes? And which magnetic and material parameters influence the hybrid spin wave dispersion?

In Secs. 4.1 we answer these questions by demonstrating that interface exchange coupling causes the coupling of AFM and FM modes. We start by determining the critical applied field under which the AFM Néel vector and the FM magnetization

align with an applied magnetic field. We compare a phenomenological analytical calculation with atomistic spin dynamics simulations [2]. In Sec. 4.2 and 4.3 we advance towards the dynamic regime. We use a phenomenological model to describe the hybrid eigenmodes of the hybrid system. We assume that while the Py is excited to its spin wave resonance, only evanescent spin wave modes protrude from the Py layer into the Mn_2Au layer. In Mn_2Au these evanescent waves can couple to the two non-degenerate modes of the AFM. As a result the exchange enhancement of the AFM mode elevates the FM spin dynamics frequencies [88]. Furthermore, the AFM dynamics can be made visible in the GHz regime, such that they can be studied without requiring THz spectroscopy equipment. We compare our phenomenological results to experimental data from FMR and BLS experiments and find good agreement. The experiments were performed by Hassan Al-Hamdo and Prof. Dr. Mathias Weiler at the RPTU Kaiserslautern, Germany.
In Secs. 4.4 we progress from uniform magnetization dynamics to DW motion. We simulate the field-driven coupled AFM-FM DW motion. We find a maximum DW velocity of $8.5\,\mathrm{km\,s^{-1}}$.

4.1 Influence on the Ferromagnetic Ground State

The first step towards understanding the coupled Mn_2Au-Py model system is to analyze the magnetic ground state in the presence of interface exchange coupling. Py is a metallic alloy and, in our samples, consists out of 80% Nickel and 20% iron. It orders ferromagnetically and has a small out-of-plane anisotropy [136]. However, the stability of its magnetic state is considered quite weak, which makes it ideal for studying the influence of interface effects. The crystal structure of Py is amorphous, but can be considered bcc in the interface region of the bilayer [86]. On the other hand, Mn_2Au has strong anisotropies, both out-of-plane that push the Néel vector into the plane, and in-plane that yield four easy axes along the $< 110 >$ directions in accordance to experiment [137] and theory [138]. Mn_2Au is a metallic, collinear AFM with a tetragonal crystal structure, as shown in Fig. 4.1 (b).
First, we use a Monte-Carlo simulation with the atomistic model to find the magnetic ground state of $8\,\mathrm{nm} \times 8\,\mathrm{nm} \times 5\,\mathrm{nm}$ of pure Mn_2Au. We find that in the low temperature ground state of Mn_2Au the spins of the two magnetic sublattices are

[2] The atomistic spin dynamics simulations of the hybrid system were performed by Dr. Sarah Jenkins at the Johannes Gutenberg-Universität and the Universität Duisburg Essen, Germany.

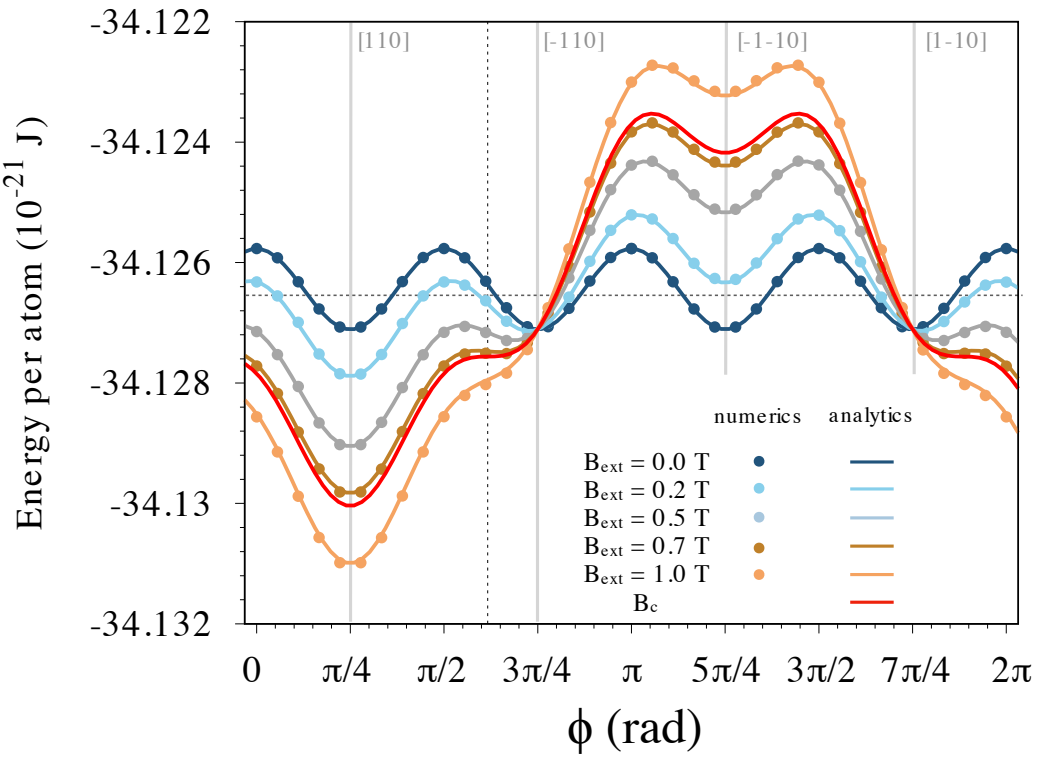

Figure 4.2: Energy surfaces of a Mn_2Au-Py hybrid. Numeric data was obtained from atomistic simulations and analytical data from phenomenology. The critical field is $B_c \approx 0.7555\,\mathrm{T}$. The Mn_2Au thickness was 5 nm, the Py was 1 nm thick.

oriented 180° apart along the [110] and [1$\bar{1}$0] directions, as shown in Fig. 4.1 (b). Details for the simulations are given in Appendix A.2.1.

Secondly, we add 1 nm of Py on top of the Mn_2Au. We use interface exchange coupling of the form $J_{\mathrm{exch}}\,\mathbf{m}\cdot\mathbf{n}$ to directly couple the FM magnetization and the AFM Néel vector. Here, J_{exch} is the exchange coupling strength [86, 88]. Because Py has a weaker anisotropy compared to Mn_2Au we assume that in the strong coupling and thin film limit the FM magnetization will align with the adjacent AFM Néel vector. Thus, we can define an effective order parameter that aligns with the FM magnetization and with one of the AFM sublattices and goes throughout the bilayer. This effective order parameter makes the angle ϕ with the [100] direction.

In order to find the ground state orientation of the effective order parameter we use simulations and analytical calculations. For the simulations we use a constrained Monte-Carlo technique [139]. We fix the direction of one of the sublattices of Mn, while all other spins are allowed to freely relax into their corresponding ground

state. The calculations use a phenomenological model with the energy density for the static magnetic state as

$$w(\phi) = E_0 + c_\phi k_\phi \cos(4\phi) - c_B \mu_{\mathrm{Py}} B_{\mathrm{ext}} \cos(\phi - \psi), \tag{4.1}$$

where the constants c_ϕ and c_B depend on the system. c_ϕ is the AFM effective anisotropy multiplied by the layer thickness of the Mn_2Au and c_B is the FM effective anisotropy times the layer thickness of the Py. E_0 is the energy of the system without the four-fold in-plane AFM anisotropy and the Zeeman term. The second term corresponds to the AFM in-plane magnetocrystalline anisotropy, that has four-fold rotational symmetry in-plane with easy-axes along $< 110 >$ directions [137, 138, 140] and the anisotropy constant is $k_\phi > 0$. The magnetic field B_{ext} couples to the magnetization, i.e. the average spin moment of Py per atom μ_{Py}, as shown in the third term. The external field is applied in-plane, where ψ is the in-plane angle.

In Fig. 4.2 we present the energy per atom as a function of the angle ϕ both from simulations and from the calculation. The magnetic field along [110] lifts the four-fold degeneracy of the ground state. The energy is lowest for the magnetization that points along the magnetic field, $\phi = \pi/4 = \psi$. For magnetic domains in which the magnetization points perpendicularly to the magnetic field, $\phi = 3/4\,\pi$ and $7/4\,\pi$, the energy is independent of the strength of the magnetic field. $\phi = 5/4\,\pi$ is energetically unfavorable. When the magnetic field strength is increased beyond the critical switching field, $B_{\mathrm{ext}} \geq B_c$, the metastable states at $\phi = 3/4\,\pi$ and $7/4\,\pi$ disappear. The reason being, that at B_c the local minima near $\phi = 3/4\,\pi$ and $7/4\,\pi$ shift and turn into saddle points, with $\partial w(\phi) / \partial\phi \,|_{\phi=\tilde{\phi}} = 0$, $\partial^2 w(\phi) / \partial\phi^2 \,|_{\phi=\tilde{\phi}} = 0$ and $\partial^3 w(\phi) / \partial\phi^3 \,|_{\phi=\tilde{\phi}} \neq 0$. Solving these equations close to $\phi = 3/4\,\pi$, we obtain

$$B_c = \frac{16\sqrt{6}\, k_\phi\, c_\phi}{9\,\mu_{\mathrm{Py}}\, c_B}, \tag{4.2}$$

with $\tilde{\phi} = 3/4\,\pi - \delta\phi \approx 1.9357$ being independent of the model parameters, as the saddle point condition is entirely controlled by the superposition of the trigonometric functions in the energy density. Using the parameters $k_\phi^{\mathrm{Mn_2Au}} = 8.001\,09 \times 10^{-25}$ J/atom [138], $\mu_{\mathrm{Py}} = 1.6\,\mu_B$, we obtain from the simulation results $E_0 \approx -34.1264 \cdot 10^{-21}$ J/atom, $c_\phi \approx 0.8375$ and $c_B \approx 0.2603$. For the critical field value, for which the AFM-FM system aligns with the magnetic field, we obtain $B_c \approx 0.7555$ T, which agrees with experimental observations [86].

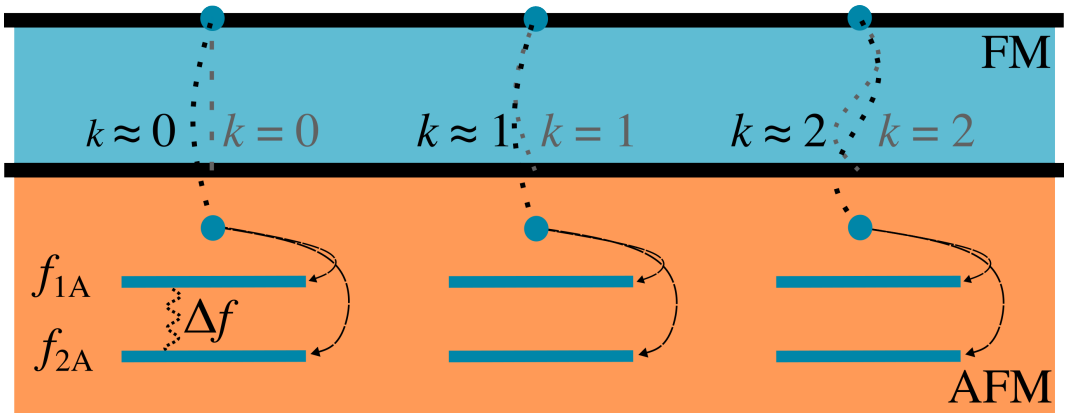

Figure 4.3: Coupling of the FM and AFM modes. Spin waves, that are excited in the FM lead to coupled evanescent waves in the AFM due to interface exchange coupling.

Thus, we find that due to interface exchange coupling in Mn_2Au-Py relatively low magnetic fields can alter the coupled AFM-FM state. In the next section we will continue to develop our description of interface exchange coupling and advance our phenomenological model towards the dynamic regime.

4.2 Enhancement of the Ferromagnetic Resonance Frequency

Previously we have seen how interface exchange coupling can enhance the influence of a magnetic field on the AFM Néel vector. In this case, the the FM magnetization mediated the action of the magnetic field. We now investigate the resonant magnetic dynamics of thin-film poly-crystalline Py deposited on single-crystalline thin-film Mn_2Au.

The idea for our model is the following: We consider the lowest energy zero wave vector FM spin wave, shown in grey in Fig. 4.3. In absence of interface exchange coupling, the boundary conditions for this mode are of von-Neumann type: At the surfaces of the FM layer, the oscillation of the spin waves has to have nodes. The novelty in our model lies in the modification of these boundary conditions due to interface exchange coupling. The FMR mode can protrude for a finite length into the AFM layer, where the momentum of the excitation is dissipated. An evanescent mode, which does not oscillate in space, but decays by nature, is excited in the AFM. The AFM evanescent mode is governed by the intrinsic properties of the AFM - exchange and anisotropy strength. These properties give the evanescent wave a

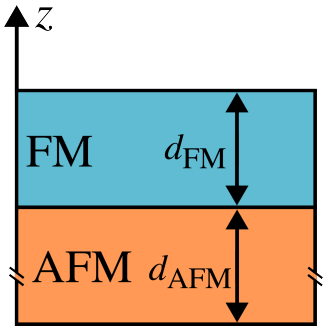

Figure 4.4: Setup of the phenomenological model.

characteristic decay length, that is the inverse of the excitation k vector. Because Mn_2Au has two resonance modes, corresponding to the in-plane and out-of-plane anisotropy energies [138], there are two evanescent modes, that the FM can couple to. Consequently, the FM mode is split in two. In the process, the FM wave vector k_F (subscript omitted in Fig. 4.3) vector is modified to a non-zero value, shown as the black mode in Fig. 4.3, because the length scale of the oscillation changed.
Consider a hybrid system, where the AFM occupies the lower half space from $z = -d_{AFM} - d_{FM}/2$ to $z = -d_{FM}/2$. The FM is situated from $z = -d_{FM}/2$ to $z = d_{FM}/2$, cf. Fig. 4.4. We build the model starting from the phenomenological energy density. In the long wavelength limit we consider only terms up to second order for the gradient expressions. Magnetization and Néel vector have a normalized length of $|\mathbf{m}| = M_{FM}$ and $|\mathbf{n}| = M_{AFM}$, respectively. We assume an isotropic system in x and y, such that we can use effective two-dimensional model in the yz plane. We model the Py using a weak in-plane and an out-of-plane anisotropy. The Mn_2Au has a strong negative out-of-plane anisotropy, forcing the Néel vector orientation to lie in the xy plane (easy plane), where a fourth order rotational anisotropy governs the easy axis directions. To this end, the energy density is given by

$$w_{AFM} = \frac{1}{2} H_{\parallel}^{A} n_y^2 + \frac{1}{2} H_{\perp}^{A} n_z^2 + \frac{1}{2} J_{AFM} \left[(\nabla n_y)^2 + (\nabla n_z)^2 \right], \tag{4.3}$$

$$w_{FM} = \frac{1}{2} H_{\parallel}^{F} m_y^2 + \frac{1}{2} H_{\perp}^{F} m_z^2 + \frac{1}{2} J_{FM} \left[(\nabla m_y)^2 + (\nabla m_z)^2 \right] - M_{FM} \mu_0 (H_y m_y + H_z m_z), \tag{4.4}$$

$$w_{int} = J_{exch} \xi M_{AFM} M_{FM} \left[m_y n_y + m_z n_z - \frac{1}{2} m_y^2 - \frac{1}{2} n_y^2 - \frac{1}{2} m_z^2 - \frac{1}{2} n_z^2 \right] \delta\left(z + \frac{d_{FM}}{2} \right), \tag{4.5}$$

where the AFM energy density w_{AFM} is comprised of in-plane and out-of-plane anisotropy fields $H_{\parallel}^{A} := K_{\parallel}^{N} M_{\mathrm{AFM}}$ and $H_{\perp}^{A} := K_{\perp}^{N} M_{\mathrm{AFM}}$, exchange and coupling to an external magnetic field. $K_{\parallel}^{N}$ and $K_{\perp}^{N}$ are the anisotropy constants. μ_0 is the magnetic field constant. The FM energy density w_{FM} consists of in-plane and out-of-plane anisotropy terms $H_{\parallel}^{F} := K_{\parallel}^{M} M_{\mathrm{FM}}$ and $H_{\perp}^{F} := K_{\perp}^{M} M_{\mathrm{FM}}$, exchange and coupling to an external magnetic field. The external field $\mathbf{H}$ couples to the FM magnetization. We model the coupling between the AFM and the FM layers by w_{int}, which is given by direct coupling of the FM magnetization and the AFM Néel vector, that favors parallel alignment of the two. Here we introduce the phenomenological length scale ξ, that gives the thickness of the interface region in which the interface exchange coupling influences the magnetization.
We neglect damping, the effect of an external field on the AFM and linearize the equations of motion

$$\ddot{n}_y + \omega_{\parallel 0}^2 n_y - \tilde{c}^2 \Delta n_y = 0, \tag{4.6}$$

$$\ddot{n}_z + \omega_{\perp 0}^2 n_z - \tilde{c}^2 \Delta n_z = 0, \tag{4.7}$$

$$\dot{m}_y = \omega_{2,\mathrm{FM}} m_z - \gamma J_{\mathrm{FM}} \Delta m_z + \gamma \mu_0 H_0 m_z, \tag{4.8}$$

$$\dot{m}_z = -\omega_{1,\mathrm{FM}} m_y + \gamma J_{\mathrm{FM}} \Delta m_y - \gamma \mu_0 H_0 m_y, \tag{4.9}$$

where γ is the gyromagnetic ratio of the electron, $J_{\mathrm{FM}} = A_{\mathrm{FM}}/M_{\mathrm{FM}}$ is the FM exchange stiffness, $\omega_{\parallel 0} := 2\pi f_{\parallel 0}$, $\omega_{\perp 0} := 2\pi f_{\perp 0}$, $f_{\parallel 0}^2 := \frac{\gamma^2}{(2\pi)^2} B_{ex} K_{\parallel}^{A}$, $f_{\parallel 0}^2 := \frac{\gamma^2}{(2\pi)^2} B_{ex} K_{\perp}^{A}$ the AFM resonance frequencies and $\omega_{1,\mathrm{FM}} := 2\pi f_{1,\mathrm{FM}}$, $\omega_{2,\mathrm{FM}} := 2\pi f_{2,\mathrm{FM}}$, $\omega_{1,\mathrm{FM}} \ll \omega_{2,\mathrm{FM}}$ the FM resonance frequencies. We estimate the magnon velocity $\tilde{c} = 2\pi c$ with $c = \frac{\gamma}{2\pi}\sqrt{A_{\mathrm{AFM}} B_{\mathrm{ex}}/(M_{\mathrm{AFM}})}$, where A_{AFM} is the AFM exchange stiffness, B_{ex} is the AFM exchange field and M_{AFM} is the AFM saturation magnetization, to $\tilde{c} \approx 22.49\,\mathrm{km\,s^{-1}}$ [141]. Other values are given in Tab. 4.1.
We use the boundary conditions imposed on the system by the interlayer coupling to determine those FM magnons that are influenced by the coupling to the AFM layer. Without coupling, the boundary conditions at the surfaces of the FM layer are of von-Neumann type. Through the terms that are introduced by the interface exchange coupling J_{exch} the boundary condition at the interface is relaxed, such that the FM excitation can penetrate the interface at $z = -\frac{d_{\mathrm{FM}}}{2}$

$$z = \frac{d_{\mathrm{FM}}}{2}: \qquad J_{\mathrm{FM}} \partial_z m_y = 0,\ J_{\mathrm{FM}} \partial_z m_z = 0, \tag{4.10}$$

Table 4.1: Model parameters.

Parameter	Value	Reference
M_{FM}	$8.6 \cdot 10^5 \frac{\mathrm{A}}{\mathrm{m}}$	[136]
A_{FM}	$10.0 \frac{\mathrm{pJ}}{\mathrm{m}}$	[142]
M_{AFM}	$1.6 \cdot 10^6 \frac{\mathrm{A}}{\mathrm{m}}$	[143]
A_{AFM}	$20.1 \frac{\mathrm{pJ}}{\mathrm{m}}$	[144, 145]
B_{ex}	1300 T	[137]
$f_{\parallel 0}$	0.3 THz	This work
$f_{\perp 0}$	> 1 THz	This work
κ_1	$0.09 \frac{1}{\mathrm{nm}}$	This work
κ_2	$\gg \kappa_1$	This work
$J_{\mathrm{exch}} M_{\mathrm{AFM}} \xi$	1.6 T nm	This work

$$z = -\frac{d_{\mathrm{FM}}}{2}: \qquad A_{\mathrm{FM}}\,\partial_z m_y + J_{\mathrm{exch}}\,\xi\,M_{\mathrm{AFM}}\Big(n_y - m_y\Big) = 0, \tag{4.11}$$

$$A_{\mathrm{FM}}\,\partial_z m_z + J_{\mathrm{exch}}\,\xi\,M_{\mathrm{AFM}}\Big(n_z - m_z\Big) = 0, \tag{4.12}$$

$$-A_{\mathrm{AFM}}\,\partial_z n_y + J_{\mathrm{exch}}\,\xi\,M_{\mathrm{FM}}\Big(m_y - n_y\Big) = 0, \tag{4.13}$$

$$-A_{\mathrm{AFM}}\,\partial_z n_z + J_{\mathrm{exch}}\,\xi\,M_{\mathrm{FM}}\Big(m_z - n_z\Big) = 0, \tag{4.14}$$

$$z = -\frac{d_{\mathrm{AFM}} + d_{\mathrm{FM}}}{2}: \qquad J_{\mathrm{AFM}}\,\partial_z n_y = 0,\ J_{\mathrm{AFM}}\,\partial_z n_z = 0. \tag{4.15}$$

We parametrize the FM magnetization and the AFM Néel vector as follows

$$\mathbf{m}(z,\,t) = \hat{x} + \delta\mathbf{m}(z,\,t), \tag{4.16}$$

$$\delta\mathbf{m} = \begin{pmatrix} 0 \\ e^{i\,2\,\pi\,f_{\mathrm{FM}}\,t}\,m_y^{k_\parallel}(z) \\ e^{i\,2\,\pi\,f_{\mathrm{FM}}\,t}\,m_z^{k_{\perp\,\tau}}(z) \end{pmatrix}, \tag{4.17}$$

$$\mathbf{n}(z,\,t) = \hat{x} + \delta\mathbf{n}(z,\,t), \tag{4.18}$$

$$\delta\mathbf{n} = \begin{pmatrix} 0 \\ e^{i\,2\,\pi\,f_{\parallel 0}\,t}\,n_y^{\kappa_1}(z) \\ e^{i\,2\,\pi\,f_{\perp 0}\,t}\,n_z^{\kappa_2}(z) \end{pmatrix}. \tag{4.19}$$

In Mn_2Au the out-of-plane anisotropy pushes the Néel vector in-plane. The in-plane anisotropy leads to a four-fold degeneracy of the in-plane easy axes along the $< 110 >$ directions. We choose our coordinate system such that the Néel

vector points along the x direction in equilibrium. Due to the interface exchange coupling, also the FM magnetization points along x in equilibrium. We study out-of-plane oscillations perpendicular to this equilibrium orientation and restrict our study to the lowest energy mode. The wave vectors of the magnon modes are given for each component: $k_{\parallel}$, $k_{\perp\,\tau}$, κ_1 and κ_2; τ is either 1 or 2, depending on the mode coupling considered between the FM and the AFM. We assume that the coupling between the AFM and the FM layers concerns only the out-of-plane excitations of the FM, which is why we now focus on $k_{\perp,\,\tau}$.
When we consider a low energy excitation, we can assume evanescent modes in the AFM layer. That means, that only in the FM a magnonic mode is excited. In this case, the oscillating magnons in the FM decay exponentially upon entering the AFM at the interface. We parametrize the perturbation as

$$m_\alpha^k(z) \;=\; a_k \left[e^{i\,k\,(z\,-\,d_{\mathrm{FM}}/2)} \;+\; e^{-i\,k\,(z\,-\,d_{\mathrm{FM}}/2)} \right], \tag{4.20}$$

$$n_\alpha^\kappa(z) \;=\; c_\kappa \left[e^{\kappa\,(z\,+\,d_{\mathrm{AFM}}\,+\,d_{\mathrm{FM}}\,/\,2)} \;+\; e^{-\kappa\,(z\,+d_{\mathrm{AFM}}\,+\,d_{\mathrm{FM}}\,/\,2)} \right]. \tag{4.21}$$

a_k and c_κ denote the coefficients of the perturbation to the order parameter. α denotes the spatial components and k and κ are the wave vectors according to the spatial component under consideration. By inserting the ansatz Eqns. (4.20), (4.21) into the boundary conditions Eqns. (4.10)ff, we obtain for the boundary condition on the wave vectors at $z \;=\; -d_{\mathrm{FM}}/2$

$$\begin{aligned} \Big[A_{\mathrm{FM}}\, k_{\perp\,\tau}\, \sin(k_{\perp\,\tau}\, d_{\mathrm{FM}}) \;-\; J_{\mathrm{exch}}\, M_{\mathrm{AFM}}\, \xi\, \cos(k_{\perp\,\tau}\, d_{\mathrm{FM}}) \Big]\, a & \\ + J_{\mathrm{exch}}\, M_{\mathrm{AFM}}\, \xi\, \cosh(\kappa_\tau\, d_{\mathrm{AFM}})\, c \;=\; 0, & \qquad (4.22) \\ J_{\mathrm{exch}}\, M_{\mathrm{FM}}\, \xi\, \cos(k_{\perp\,\tau}\, d_{\mathrm{FM}})\, a \;+\; \Big[- A_{\mathrm{AFM}}\, \kappa\, \sinh(\kappa_\tau\, d_{\mathrm{AFM}}) & \\ - J_{\mathrm{exch}}\, M_{\mathrm{FM}}\, \xi\, \cosh(\kappa_\tau\, d_{\mathrm{AFM}}) \Big]\, c \;=\; 0, & \qquad (4.23) \end{aligned}$$

from which we extract a condition on $k_{\perp\,\tau}$

$$\begin{aligned} - A_{\mathrm{FM}}\, A_{\mathrm{AFM}}\, k_{\perp\,\tau}\, \kappa_\tau\, \sin(k_{\perp\,\tau}\, d_{\mathrm{FM}})\, \sinh(\kappa_\tau\, d_{\mathrm{AFM}}\,) & \\ - A_{\mathrm{FM}}\, k_{\perp\,\tau}\, \sin(k_{\perp\,\tau}\, d_{\mathrm{FM}})\, J_{\mathrm{exch}}\, M_{\mathrm{FM}}\, \xi\, \cosh(\kappa_\tau\, d_{\mathrm{AFM}}) & \\ + A_{\mathrm{AFM}}\, \kappa_\tau\, \sinh(\kappa_\tau\, d_{\mathrm{AFM}})\, J_{\mathrm{exch}}\, M_{\mathrm{AFM}}\, \xi\, \cos(k_{\perp\,\tau}\, d_{\mathrm{FM}}) \;=\; 0. & \qquad (4.24) \end{aligned}$$

For simplicity we omit the indices of the coefficients a and c. We approximate the AFM wave vector ($f \ll f_{\parallel 0},\, f_{\perp 0}$)

$$\begin{aligned} \kappa_1 &= \frac{\sqrt{f_{\parallel 0}^2 - f^2}}{c} \approx \frac{\sqrt{f_{\parallel 0}^2}}{c}, \\ \kappa_2 &= \frac{\sqrt{f_{\perp 0}^2 - f^2}}{c} \approx \frac{\sqrt{f_{\perp 0}^2}}{c}. \end{aligned} \tag{4.25}$$

With the relation between the resonance frequencies and the AFM wave vectors we can simplify the condition on $k_{\perp\tau}$

$$\begin{aligned} & k_{\perp\tau}\,\kappa_\tau \tan(k_{\perp\tau}\,d_{\mathrm{FM}}) \tanh(\kappa_\tau\,d_{\mathrm{AFM}}) \\ &= \frac{J_{\mathrm{exch}}\,\xi}{A_{\mathrm{FM}}\,A_{\mathrm{AFM}}} \Big[- J_{\mathrm{FM}}\,k_{\perp\tau} \tan(k_{\perp\tau}\,d_{\mathrm{FM}}) + J_{\mathrm{AFM}}\,\kappa_\tau \tanh(\kappa_\tau\,d_{\mathrm{AFM}}) \Big], \end{aligned} \tag{4.26}$$

$$\begin{aligned} \Rightarrow \quad & k_{\perp 1/2}\,\frac{f_{\parallel 0\,/\,\perp 0}}{c} \tan(k_{\perp 1/2}\,d_{\mathrm{FM}}) \tanh\!\left(\frac{f_{\parallel 0\,/\,\perp 0}}{c}\,d_{\mathrm{AFM}}\right) \\ &= \frac{J_{\mathrm{exch}}\,\xi}{A_{\mathrm{FM}}\,A_{\mathrm{AFM}}} \Big[- J_{\mathrm{FM}}\,k_{\perp 1/2} \tan(k_{\perp 1/2}\,d_{\mathrm{FM}}) \\ & + J_{\mathrm{AFM}}\,\frac{f_{\parallel 0\,/\,\perp 0}}{c} \tanh\!\left(\frac{f_{\parallel 0\,/\,\perp 0}}{c}\,d_{\mathrm{AFM}}\right) \Big] \end{aligned} \tag{4.27}$$

These relations are not solvable analytically, which is why we solve them graphically. For this we rewrite them into a single transcendental equation

$$k_{\perp 1/2}\,d_{\mathrm{FM}} \tan(k_{\perp 1/2}\,d_{\mathrm{FM}}) = \frac{\frac{J_{\mathrm{exch}}\,M_{\mathrm{AFM}}\,\xi}{A_{\mathrm{FM}}}\,d_{\mathrm{FM}}\,\frac{f_{\parallel 0\,/\,\perp 0}}{c} \tanh\!\left(\frac{f_{\parallel 0\,/\,\perp 0}}{c}\,d_{\mathrm{AFM}}\right)}{\frac{f_{\parallel 0\,/\,\perp 0}}{c} \tanh\!\left(\frac{f_{\parallel 0\,/\,\perp 0}}{c}\,d_{\mathrm{AFM}}\right) + \frac{J_{\mathrm{exch}}\,M_{\mathrm{FM}}\,\xi}{A_{\mathrm{AFM}}}}. \tag{4.28}$$

Fig. 4.5 shows schematically how the allowed wave vector values, that solve the transcendental equation, can be visualized. The left-hand-side of Eqn. (4.28) has periodicity in k, while the right-hand-side is constant. Because Mn_2Au has two non-degenerate modes with different κ vectors, there are two values the right-hand-side of Eqn. (4.28) can assume. Eqn. (4.28) has periodic solutions at the intersections of the left-hand-side equation with these lines in Fig. 4.5.
For the parameter values of this experiment, which are given in Tab. 4.1, we can

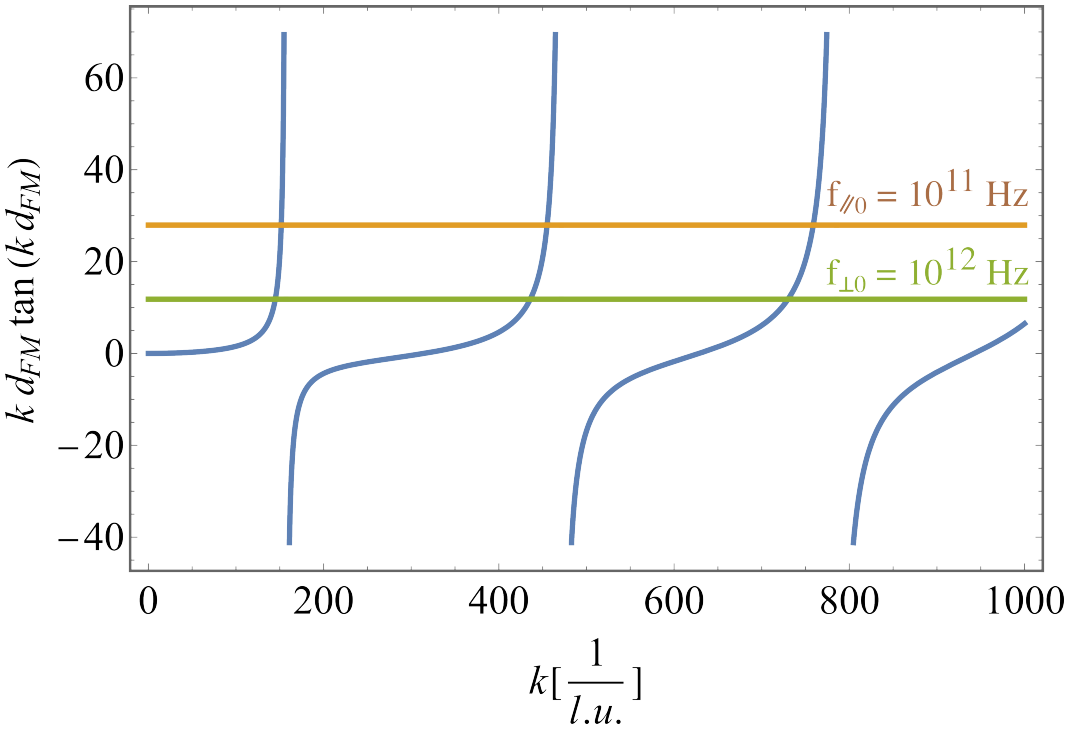

Figure 4.5: Graphic solution of the transcendental equation Eqn. (4.28). The blue line shows $k\,d_{\mathrm{FM}}\,\tan(k\,d_{\mathrm{FM}})$, while the orange curve shows the right-hand-side of Eqn. (4.28) for $f_{\parallel 0} = 10^{11}$ Hz and the green curve shows the right-hand-side of Eqn. (4.28) for $f_{\perp 0} = 10^{12}$ Hz.

approximate $\tan(x) \approx x$, $M_{\mathrm{AFM}} \approx M_{\mathrm{FM}}$ and $\tanh(x) \approx 1$

$$k_{\perp\,1/2} = \sqrt{\frac{1}{J_{\mathrm{FM}}}\,\frac{J_{\mathrm{exch}}\,\xi\,A_{\mathrm{AFM}}\,\kappa_{1,2}}{(J_{\mathrm{AFM}}\,\kappa_{1,2} + J_{\mathrm{exch}}\,\xi)}}\,\frac{1}{\sqrt{d_{\mathrm{FM}}}}. \tag{4.29}$$

With Eqn. (4.29) we are now able to find the k vectors that contribute to the hybrid modes in the bilayer system. By inserting these values into the Kittel equation, we will find the corresponding frequencies, as described in the next section.
In summary, we find that interface exchange coupling leads to a frequency enhancement and splitting of the FM magnon spectrum. The direct coupling of the AFM and FM spin dynamics modifies the standard boundary conditions. When a FM magnon is excited, it possesses a characteristic k vector. If this k vector corresponds to a solution of the transcendental equation, the FM magnon couples to an AFM evanescent spin wave. Associated with the coupling is a modification of the length scale of the FM oscillation and thereby its k vector. As a result the frequency of the FM magnon does not only increase, but the resonance mode splits

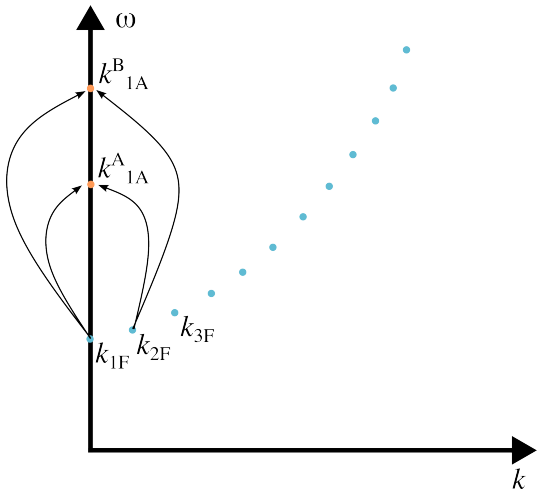

Figure 4.6: The FM has quadratic dispersion, and allowed k vectors (blue) can couple to the lowest energy AFM magnon modes (orange).

into two branches. Each branch couples to a different mode of the AFM, as shown in Fig. 4.6. As a result, the FMR signal consists of two resonances, instead of the single pure FM mode.
So far we have developed a novel model, which describes the coupled magnon dynamics in Mn_2Au-Py. Does the model agree with the experiment? And how accurately can material constants be determined using the model? In the next section we will answer these questions by applying our model to experimental data.

4.3 Coupled Magnon Dynamics

In the previous section we developed a model to describe the coupled magnon dynamics in Mn_2Au-Py. In this section we will apply this model to experimental data from our collaborators Hassan Al-Hamdo and Prof. Dr. Mathias Weiler at the RPTU Kaiserslautern, Germany.
For the experiment our collaborators epitaxially grew 40 nm thick Mn_2Au thin films on Al_2O_3 substrates. These were then covered with Py thin film layers with thicknesses of $2\,\text{nm} \leq d_{\text{FM}} \leq 30\,\text{nm}$ [86, 144, 146].
They performed FM resonance spectroscopy using a coplanar wave guide. In such an experiment the sample is glued onto a microwave guide. The wave guide is a microwave resonator through which an oscillating electromagnetic field can propagate. Because the sample is mounted directly on the resonator, the spatial distribution of the oscillating field throughout the sample is homogeneous, such that a homogeneous excitation of spin waves can be achieved. In addition, the copla-

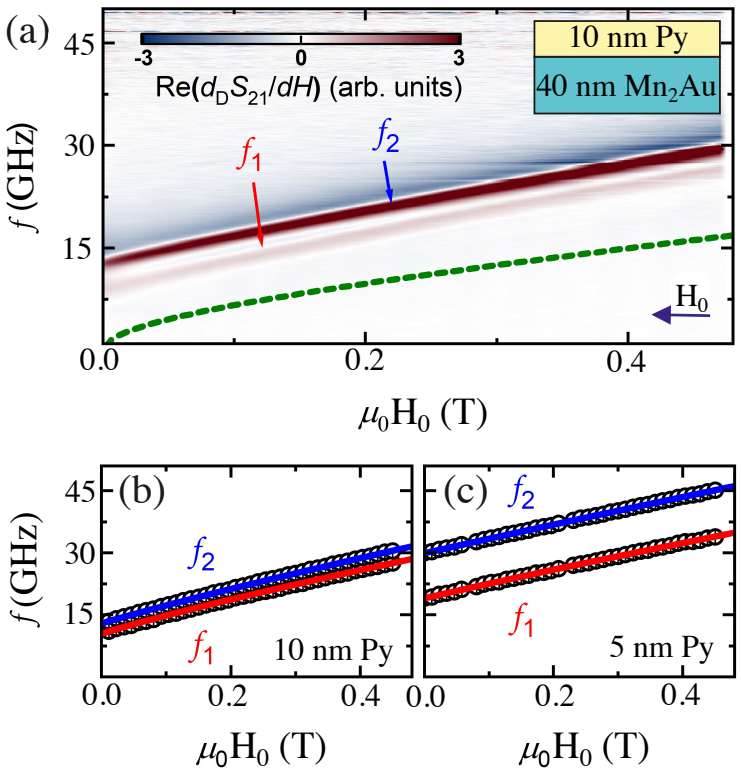

Figure 4.7: (a) Spectrum FMR signal of a Mn_2Au (40 nm)-Py (10 nm) sample. The dashed line indicates the expected FMR for a bare Py thin film. (b) Resonance frequencies f_1 and f_2 vs. external magnetic field H_0 obtained from fitting data in panel (a). The lines are fits to the modified Kittel equation from our model (see text) with M_{FM} = 1 T as a fitting parameter. (c) Same as (b) but for a Mn_2Au (40 nm)-Py (5 nm) sample.

nar wave guide with the sample mounted is placed inside an electro magnet such that a static magnetic field can be applied in the sample plane. The coplanar wave guide can be rotated around the out-of-plane axis in the static magnetic field. This means that the static magnetic field can be applied along an arbitrary in-plane direction of the sample. In our case, the field is applied in-plane, in parallel with the sample's magnetization and Néel vector. A coil detects the response signal that the excited spin waves emit and the data post processing, that involves a Fourier transformation of the signal reveals the spin wave frequency spectrum including the resonance.

In Fig. 4.7 (a) we present the FMR spectrum [147] that was measured using a Py (10 nm)-Mn_2Au (40 nm) sample. The dashed, green line indicates the signal of pure in-plane isotropic polycrystalline Py. For the bilayer system, however, we find two resonance modes with non-degenerate frequencies f_1 and f_2, both of which are

enhanced by $O(10\,\mathrm{GHz})$ over the pure Py mode. The $f_2 > f_1$ mode is stronger and higher in frequency compared to the f_1 mode. Thus, we find both a frequency enhancement and a frequency splitting of the FMR mode, as we show in Fig. 4.7 (b).

The measurement was repeated in a series for all samples with different thicknesses of the FM Py layer. We found that when the FM layer thickness becomes smaller, the frequency enhancement over the pure Py mode and the frequency splitting between f_1 and f_2 become larger, as shown in Fig. 4.7 (c) for a Py (5 nm)-Mn_2Au (40 nm) sample. The thickness dependence of the frequency splitting suggests the interfacial origin of the interface exchange coupling that we use in our model. The lines in Fig. 4.7 (b) and (c) are fits using Eqn. (4.30). Below we explain how we apply our model from the previous section Sec. 4.2 to model these results.

We use the dipolar exchange spin wave dispersion in a tangentially magnetized FM thin film [148, 149] to fit our data

$$f(k_\perp, k_\parallel) = \frac{\gamma}{2\pi}\sqrt{B_\perp B_\parallel}, \tag{4.30}$$

with the effective out-of-plane stiffness field

$$B_\perp = \mu_0 H_0 + J_{\mathrm{FM}}(k_\perp^2 + k_\parallel^2) + \mu_0 M_{\mathrm{FM}} G_0, \tag{4.31}$$

and in-plane stiffness field

$$B_\parallel = \mu_0 H_0 + J_{\mathrm{FM}}(k_\perp^2 + k_\parallel^2) + \mu_0 M_{\mathrm{FM}}(1 - G_0). \tag{4.32}$$

Here, M_{FM} is the saturation magnetization of the FM. The external magnetic field $\mathbf{H}_0$ is applied in the film plane parallel to the magnetization $\mathbf{m}$. $J_{\mathrm{FM}} = A_{\mathrm{FM}}/M_{\mathrm{FM}}$ with exchange stiffness A_{FM}. The factor

$$G_0 = \frac{1 - \exp(-k_\parallel d)}{k_\parallel d} \tag{4.33}$$

accounts for the effects of dipole-dipole interactions [149], where $k_\parallel$ is the in-plane wave vector. In our FMR experiments only FMR modes corresponding to out-of-plane k vectors are excited as the coupled spin waves propagate along the out-of-plane direction through the FM and into the AFM. Hence, $k_\parallel = 0$, but $k_\perp \neq 0$ as sketched in Fig. 4.8 (a).

In our experiments, spin waves are excited in the FM by the oscillating field of the FMR setup. No spin waves are excited in the AFM, as the applied frequencies are

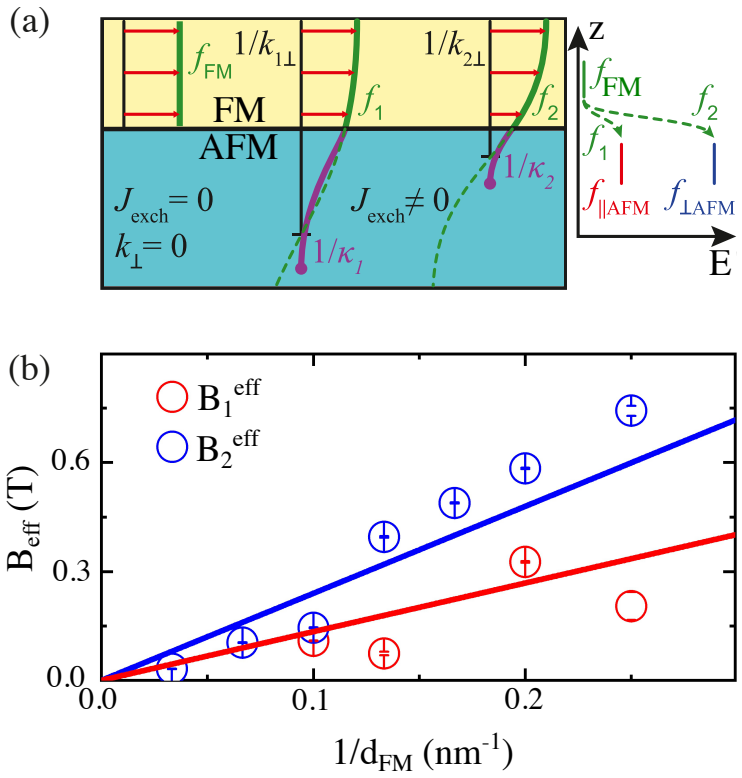

Figure 4.8: (a) Sketch of the sample structure and coupling of modes. The FMR with frequency f_{FM} couples to the two AFM modes in the AFM. This results in hybrid modes with frequencies f_1 and f_2 with perpendicular wave vector $k_{i,\perp}$. The Néel vector excitations decay within $1/\kappa_i$ (see text). (b) The effective stiffness fields resulting from the mode coupling exceed 0.6 T for Py thickness $d_{FM} \leq 5$ nm.

much below the magnon frequencies of Mn_2Au, as we will see later. However, the interface exchange coupling between the AFM and the FM leads to a modification of the boundary conditions for the excited FM spin wave. In contrast to the pure Py case, where the spin wave cannot protrude the boundaries of the FM, the interface exchange coupling allows the dissipation of the energy of the FM spin wave into the AFM layer. In the AFM, no oscillating spin wave is present, but an evanescent wave, which does not oscillate space, but rather decays with a characteristic decay length κ, cf. Eqn. (4.21). This means that only those FMR modes are excited, whose k vectors allow for coupled modes in the bilayer system. These k vectors satisfy Eqn. (4.29).

We sketch the coupling of the modes in Fig. 4.8 (a): The figure consists of three columns. In the leftmost column, the uncoupled, pure Py spin wave is shown. In the other two columns, interface exchange coupling leads to a modification of the

k vector of the FM spin wave, as it protrudes into the AFM layer. The distance it can protrude into the AFM layer is governed by the decay $\propto \exp(-\kappa z)$, where κ is the decay constant. This modification of the FMR k vector consequently leads to a frequency enhancement.

In Mn_2Au the out-of-plane anisotropy pushed the Néel vector into the plane, while the in-plane anisotropy favors the in-plane easy axes directions. Because of this tetragonal symmetry, two non-degenerate resonance modes can be excited in the in-plane AFM. These modes correspond to an in-plane mode where the Néel vector oscillates in-plane with f_0 and a stronger out-of-plane mode, where the Néel vector oscillates out-of-plane with $f_{\perp 0}$. The FM spin wave couples non-degenerately to both of these modes, which leads to a splitting of the FMR mode into two modes with different frequencies. The frequencies are given by

$$f_{\parallel \mathrm{AFM}} = \sqrt{f_{\parallel 0}^2 + c^2 (k_\perp^2 + k_\parallel^2)}, \tag{4.34}$$

$$f_{\perp \mathrm{AFM}} = \sqrt{f_{\perp 0}^2 + c^2 (k_\perp^2 + k_\parallel^2)}. \tag{4.35}$$

Here, $2\pi c$ is the magnon velocity in the AFM which depends on the AFM exchange stiffness A_{AFM} and the exchange field B_{ex} that keeps the antiparallel alignment of magnetic sublattices in the AFM

$$c = \frac{\gamma}{2\pi} \sqrt{\frac{A_{\mathrm{AFM}} B_{\mathrm{ex}}}{M_{\mathrm{AFM}}}}. \tag{4.36}$$

The out-of-plane mode is strongest $f_{\perp 0} \gg f_{\parallel 0} \gg f_{\mathrm{FM}}$, and we neglect the effect of the dc magnetic field $\mathbf{H}_0$ on the AFM spectra. We show a quantitative calculation of the coupled modes in Fig. 4.9, where the different decay lengths of the two evanescent modes in the AFM and the corresponding wave length of the FM spin wave are clearly visible. The top panel shows the uncoupled, pure Py case, while the bottom two panels show the coupled modes.

In Eqn. (4.25) we have shown that the decay length κ depends on the eigenfrequency of the AFMR mode and is different for in-plane and out-of-plane branches

$$\kappa_1 = \frac{\sqrt{f_{\parallel 0}^2 - f_1^2}}{c} \approx \frac{f_{\parallel 0}}{c}, \tag{4.37}$$

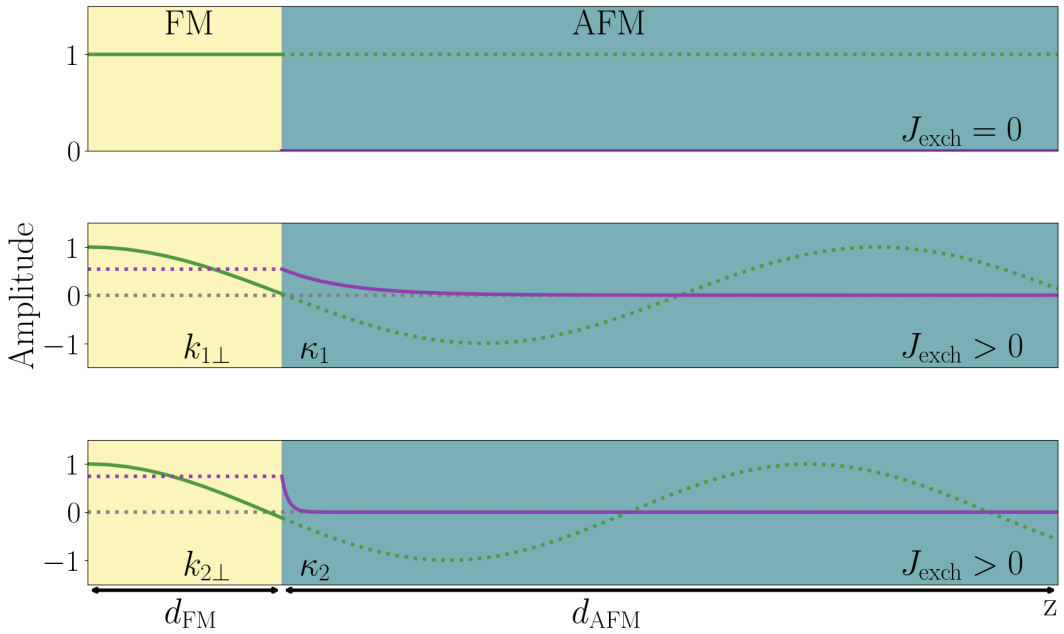

Figure 4.9: Numerical visualization of the coupled modes. Non-zero interface exchange coupling leads to the continuation of the FM spin wave as an evanescent mode in the AFM. The top panel shows the uncoupled case, while the bottom two panels show the two non-degenerate modes that arise in the coupled case.

$$\kappa_2 = \frac{\sqrt{f_{\perp 0}^2 - f_2^2}}{c} \approx \frac{f_{\perp 0}}{c}. \tag{4.38}$$

The eigenfrequencies $f_1 := f(k_\parallel, k_{1\perp})$ and $f_2 := f(k_\parallel, k_{2\perp})$ are calculated from Eqn. (4.30) by substituting those values of wave vectors $k_{1\perp}$ and $k_{2\perp}$ that satisfy the boundary conditions in Eqn. (4.10)ff. For estimating $k_{1\perp}$ and $k_{2\perp}$, we focus on the lowest modes with $k_{1\perp}, k_{2\perp} \ll \pi/d_{\mathrm{FM}}$ that have larger overlap with the homogeneous oscillating magnetic field than the other modes.

We now want to compare our results to previous measurements of the interface exchange coupling in this system [86] and estimate the AFM magnon frequencies from our data. From Eqn. (4.30) we can define the effective stiffness field induced by the coupled AFM-FM spin dynamics

$$B_1^{\mathrm{eff}} := J_{\mathrm{FM}}\, k_{1\perp}^2, \tag{4.39}$$

$$B_2^{\mathrm{eff}} := J_{\mathrm{FM}}\, k_{2\perp}^2. \tag{4.40}$$

The stiffness fields scale linearly as $1/d_{\mathrm{FM}}$ as shown in Eqn. (4.29). Furthermore, they are proportional to the exchange coupling J_{exch} between FM and AFM layers. We obtain values for the stiffness fields from fitting f_1 and f_2 vs. H_0 by Eqn. (4.30), as shown in Fig. 4.8 (b) (data points). The lines are linear fits in accordance with the scaling expected from Eqn. (4.29). We show the detailed fitting procedure in Appendix A.2.2.

In order to relate our results to the coercivity measurements in Bommanaboyena et al. [86] it is instrumental to understand, that on the one hand, we calculate the coupling strength from dynamic measurements of the resonance frequency. On the other hand, coercivity measurements measure the interface exchange coupling from a static magnetization texture in the magnetic ground state. But we can relate the coercive field $\mu_0 H_{\mathrm{c}}$ of our sample series within experimental uncertainty to B_1^{eff}

$$B_1^{\mathrm{eff}} \approx \mu_0 H_{\mathrm{c}} = \frac{4\,\xi\, B_{\mathrm{an}}\, J_{\mathrm{exch}}\, M_{\mathrm{FM}}\, d_{\mathrm{AFM}}}{4\, B_{\mathrm{an}}\, d_{\mathrm{AFM}} + \xi\, J_{\mathrm{exch}}\, M_{\mathrm{FM}}} \frac{1}{d_{\mathrm{FM}}}, \tag{4.41}$$

where B_{an} is the AFM in-plane anisotropy field. This expression corresponds to Eqn. (2) of Ref. [86]. B_2^{eff} is related to the out-of-plane anisotropy of Mn_2Au, which due to the experimental geometry is not accessible in the static measurements [86]. Using Eqn. (4.41) for fitting the experimentally determined $\mu_0 H_{\mathrm{c}}$ [86], we determine $\xi J_{\mathrm{exch}} M_{\mathrm{FM}} \approx 1.6\,\mathrm{T\,nm}$. This interface exchange coupling is stronger compared to reports on the insulating AFM/metallic FM bilayers Co-$LaFeO_3$ [119] or Fe-NiO [104]. Moreover, while frequency enhancement was found by earlier studies the mode splitting remains a novelty in AFM-FM bilayers [150, 151].

Using the fitting of the effective fields $B_1^{\mathrm{eff}} := J_{\mathrm{FM}}\, k_{1\perp}^2$ and $B_2^{\mathrm{eff}} := J_{\mathrm{FM}}\, k_{2\perp}^2$ as a function of the inverse FM thickness, as shown in Fig. 4.8 (b), we further determine $B_2^{\mathrm{eff}}/B_1^{\mathrm{eff}} \approx 2.4$. This ratio is inserted into Eqn. (4.29)

$$\frac{B_2^{\mathrm{eff}}}{B_1^{\mathrm{eff}}} = \frac{\kappa_2}{\kappa_1} \cdot \frac{\kappa_1\, J_{\mathrm{AFM}} + \xi\, J_{\mathrm{exch}}\, M_{\mathrm{FM}}}{\kappa_2\, J_{\mathrm{AFM}} + \xi\, J_{\mathrm{exch}}\, M_{\mathrm{FM}}}. \tag{4.42}$$

From Eqn. (4.42) we can estimate

$$\frac{1}{\kappa_1} - \frac{3}{\kappa_2} = \left(\frac{B_2^{\mathrm{eff}}}{B_1^{\mathrm{eff}}} - 1\right) \frac{J_{\mathrm{AFM}}}{\xi\, J_{\mathrm{exch}}\, M_{\mathrm{FM}}} \approx 11\,\mathrm{nm}. \tag{4.43}$$

Taking into account that $\kappa_1 \ll \kappa_2$ and using the value of magnon velocity $2\,\pi\, c = 22.49\,\mathrm{km\,s^{-1}}$, we estimate $f_{\parallel 0} \approx 0.3\,\mathrm{THz}$, which is about a factor two larger than previous direct THz measurements of magnons in Mn_2Au films grown by a different technique [152]. Thus, our model provides the possibility to independently

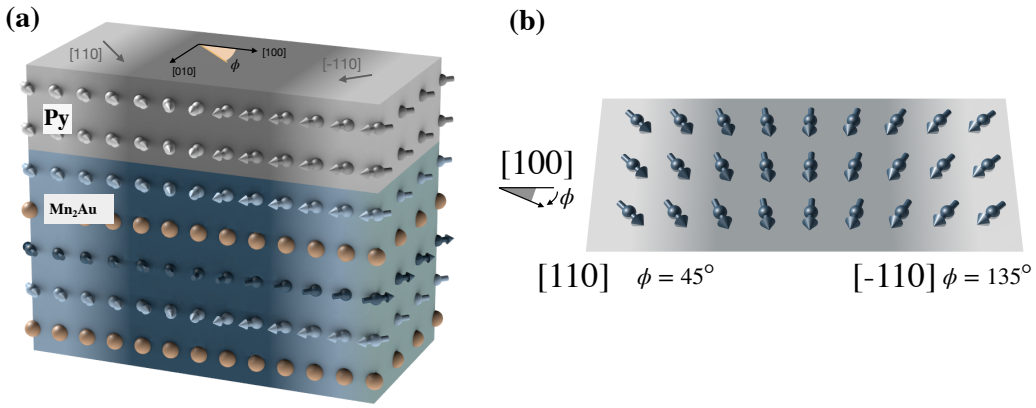

Figure 4.10: 90° DW in Mn_2Au-Py [126]. (a) Bilayer structure. (b) Top view.

determine the magnon frequency in Mn_2Au, which is in the THz range, without the experimental equipment required to measure THz frequencies.

4.4 Coupled Domain Wall Dynamics

In the previous chapter we have studied the coupled uniform spin wave dynamics in Mn_2Au-Py. However, while computing and data storage technologies rely on the switching of the magnetization as the principle carrier of information, this is done in regions - or domains. As we presented in Chap. 2, magnetic domains are separated by DWs. The reading and writing of information can be facilitated by displacing DWs using DW motion.

In this section we want to look at the stabilization of coupled DWs in Mn_2Au-Py. Moreover, we develop a model to analyze the atomistic spin dynamics simulations done by Dr. Sarah Jenkins, that study the effect of a driving magnetic field on the DW dynamics in the system.

We consider an AFM-FM hybrid, where the AFM occupies the lower half-space $z < 0$ and the FM occupies the upper half-space $z > 0$. We calculate the DW profile in the coupled AFM-FM system by using the energy density [138]

$$\mathcal{L} = \int \int_{-t_A}^{0} \mathcal{L}_A \, \mathrm{d}x \, \mathrm{d}z + \int \int_{0}^{t_F} \mathcal{L}_F \, \mathrm{d}x \, \mathrm{d}z + \mathcal{L}_{\mathrm{int}} \, \delta(z), \tag{4.44}$$

$$\mathcal{L}_A = \frac{M_S}{2 H_{\mathrm{ex}} \gamma^2} \left(\dot{\theta}_A^2 + \dot{\phi}_A^2 \sin^2(\theta_A) \right) - w_A, \tag{4.45}$$

$$w_A = \frac{1}{2} A_A \left((\nabla \theta_A)^2 + (\nabla \phi_A)^2 \sin^2(\theta_A) \right) + \frac{1}{2} H_\perp^A M_S \cos^2(\theta_A)$$

$$- \frac{1}{4} H_{\parallel}^{A} M_S \sin^4(\theta_A) \cos(4\,\phi_A), \tag{4.46}$$

$$\mathcal{L}_F = \frac{M_F}{\gamma} \dot{\phi}_F \,(1 - \cos(\theta_F)) - w_F, \tag{4.47}$$

$$w_F = \frac{1}{2} A_F \left((\nabla \theta_F)^2 + (\nabla \phi_F)^2 \sin^2(\theta_F) \right) + \frac{1}{2} H_{\perp}^{F} M_F \cos^2(\theta_F) - \frac{1}{4} H_{\parallel}^{F} M_F \sin^4(\theta_F) \cos(4\,\phi_F), \tag{4.48}$$

$$\mathcal{L}_{\text{int}} = -w_{\text{int}} = -\Big(J_{\text{exch}} M_F M_S \,\xi \,(\cos(\theta_A)\cos(\theta_F) + \sin(\theta_A)\sin(\theta_F)\cos(\phi_A - \phi_F)) \Big), \tag{4.49}$$

where the Lagrangian and energy densities with subscripts $_A$ denote the AFM part of the system ($-t_A < z < 0$ with the AFM layer thickness t_A) and subscripts $_F$ denote the FM part of the system ($0 < z < t_F$ with the FM layer thickness t_F). γ is the gyromagnetic ratio of the electron, H_{ex} is the exchange field of Mn_2Au, A_A is the exchange stiffness and the AFM anisotropies are given by an out-of-plane field $H_{\perp}^{A}$ and an in-plane field $H_{\parallel}^{A}$. For the FM we implement the exchange stiffness A_F, the out-of-plane anisotropy $H_{\perp}^{F}$ and the in-plane anisotropy $H_{\parallel}^{F}$. The interface exchange coupling is characterized by a coupling constant J_{exch} and a length scaling factor ξ. We parametrize the FM magnetization in spherical coordinates: $m_x = M_F \cos(\phi_F)\sin(\theta_F)$, $m_y = M_F \sin(\phi_F)\sin(\theta_F)$, $m_z = M_F \cos(\theta_F)$. Analogously we parametrize the AFM Néel vector as: $n_x = M_S \cos(\phi_A)\sin(\theta_A)$, $n_y = M_S \sin(\phi_A)\sin(\theta_A)$, $n_z = M_S \cos(\theta_A)$. All angles depend on the spatial coordinates x, z and the time t. Both the saturation magnetization of the AFM M_S and the FM M_F are per unit volume.

We have seen previously that Mn_2Au is an in-plane AFM and because we assume strong coupling, the AFM Néel vector and the FM magnetization align in-plane. For a 90° DW along x, as shown in Fig. 4.10, the boundary conditions are

$$z = 0: \qquad \phi_A = \phi_F, \quad \theta_A = \theta_F, \tag{4.50}$$

$$x \to \infty: \qquad \phi_A \to \frac{\pi}{2} \text{ or } \frac{3}{2}\pi, \quad \theta_A \to \frac{\pi}{2}, \tag{4.51}$$

$$\phi_F \to \frac{\pi}{2} \text{ or } \frac{3}{2}\pi, \quad \theta_F \to \frac{\pi}{2}, \tag{4.52}$$

$$x \to -\infty: \qquad \phi_A \to \frac{3}{2}\pi \text{ or } \frac{\pi}{2}, \quad \theta_A \to \frac{\pi}{2}, \tag{4.53}$$

$$\phi_F \to \frac{3}{2}\pi \text{ or } \frac{\pi}{2}, \quad \theta_F \to \frac{\pi}{2}. \tag{4.54}$$

We assume that in equilibrium the DW profile $\phi_{A,F}$ is only dependent on x. The spatial dependence is carried implicitly and not explicitly denoted for simplicity. Functional minimization of the Lagrangian yields

$$
\begin{aligned}
&- H_{\parallel}^{F}\, M_F \sin^4(\theta_F) \sin(4\,\phi_F) \;-\; \frac{M_F}{\gamma} \sin(\theta_F)\, \dot{\theta}_F \;+\; A_F \sin^2(\theta_F)\, \Delta\phi_F \\
&+\; A_F \sin(2\phi_F)\, (\nabla\theta_F)\, (\nabla\phi_F) \;=\; 0, \qquad (4.55)\\
&\frac{M_F}{\gamma}\, \dot{\phi}_F \sin\theta_F \;-\; \frac{1}{2}\, A_F\, (\nabla\phi_F)^2 \sin(2\theta_F) \\
&+\; \frac{1}{2}\, H_{\perp}^{F}\, M_F \sin(2\theta_F) \;+\; H_{\parallel}^{F}\, M_F \cos(4\,\phi_F) \sin^3(\theta_F) \cos(\theta_F) \;+\; A_F\, \Delta\theta_F \;=\; 0. \qquad (4.56)
\end{aligned}
$$

for the FM energy and

$$
\begin{aligned}
&- H_{\parallel}^{A}\, M_S \sin^4(\theta_A) \sin(4\,\phi_A) \;-\; \frac{M_S}{H_{ex}\, \gamma^2}\, \ddot{\phi}_A \sin^2(\theta_A)\,, + A_A \sin^2(\theta_A)\, \Delta\phi_A \\
&+\; A_A \sin(2\theta_A)\, (\nabla\theta_A)\, (\nabla\phi_A) \;=\; 0, \qquad (4.57)\\
&\frac{M_S}{H_{ex}\, \gamma^2}\, \dot{\phi}_A^2 \sin(2\,\theta_A) \;-\; \frac{1}{2}\, A_A\, (\nabla\phi_A)^2 \sin(2\theta_A) \\
&+\; \frac{1}{2}\, H_{\perp}^{A}\, M_S \sin(2\theta_A) \;+\; H_{\parallel}^{A}\, M_S \cos(4\phi_A) \sin^3(\theta_A) \cos\theta_A + \; A_A\, \Delta\theta_A \\
&-\; \frac{M_S}{H_{ex}\, \gamma^2}\, \ddot{\theta}_A = \; 0. \qquad (4.58)
\end{aligned}
$$

for the AFM energy. At the interface the boundary terms give the conditions

$$
\begin{aligned}
A_A\, \partial_z\, \theta_A \;-\; J_{\text{int}}\, M_S\, M_F\, \xi \left(- \sin\theta_A \cos\theta_F \;+\; \cos\theta_A \sin\theta_F \cos(\phi_A \;-\; \phi_F) \right) &= 0, \qquad (4.59)\\
-A_F\, \partial_z\, \theta_F \;-\; J_{\text{int}}\, M_S\, M_F\, \xi \left(- \cos\theta_A \sin\theta_F \;+\; \sin\theta_A \sin\theta_F \cos(\phi_A \;-\; \phi_F) \right) &= 0, \qquad (4.60)\\
A_A \sin^2\theta_A\, \partial_z\, \phi_A \;+\; J_{\text{int}}\, M_S\, M_F\, \xi \sin\theta_A \sin\theta_F \sin(\phi_A \;-\; \phi_F) &= 0, \qquad (4.61)\\
-A_F \sin^2\theta_F\, \partial_z\, \phi_F \;-\; J_{\text{int}}\, M_S\, M_F\, \xi \sin\theta_F \sin\theta_A \sin(\phi_A \;-\; \phi_F) &= 0. \qquad (4.62)
\end{aligned}
$$

Thus, the equation of state is

$$-H_{\parallel}^{A} M_S \sin(4\phi_A) + A_A (\partial_x^2 + \partial_z^2) \phi_A = 0, \tag{4.63}$$

$$A_A \partial_z \phi_A + J_{\text{int}} M_S M_F \xi \sin(\phi_A - \phi_F) = 0, \tag{4.64}$$

$$-H_{\parallel}^{F} M_F \sin(4\phi_F) + A_F (\partial_x^2 + \partial_z^2) \phi_F = 0. \tag{4.65}$$

Assuming strong coupling ($\phi_A = \phi_F$) this gives the solution of the DW profile:

$$\phi_A = \arctan\left(\exp\left(\frac{x - X_0}{x_{DW}^{A}}\right)\right), \tag{4.66}$$

$$\phi_F = \arctan\left(\exp\left(\frac{x - X_0}{x_{DW}^{F}}\right)\right), \tag{4.67}$$

where X_0 is an integration constant that is used to shift the DW in the AFM and the FM part in order to match their lateral positions. The widths of the DWs are denoted by $x_{DW}^{A} = \sqrt{A_A/(4 H_{\parallel}^{A} M_S)}$ and $x_{DW}^{F} = \sqrt{A_F/(4 H_{\parallel}^{F} M_F)}$ and, due to the AFM's stronger anisotropy, the DW width in the AFM is smaller than in the FM. Due to interface exchange coupling a surface anisotropy is induced at the interface between the two layers, that modifies the DW width in both layers. We analyze this influence using atomistic spin dynamics performed by Dr. Sarah Jenkins using the open-source package VAMPIRE [79]. Specifically, we simulate Mn_2Au-Py with a 90° DW from [110] to [1$\bar{1}$0] along the [100] direction, as shown in Fig. 4.10. The system has the dimensions 1000 nm × 40 nm × (5 nm (Mn_2Au) + 1 nm (Py)) and the DW is located initially at $x = 100$ nm. The DW is initialized in both layers and the magnetization dynamics of the two layers are coupled by interface exchange coupling. Although Py is amorphous in the bulk [136, 142, 153], we assume a bcc ordering near the thin film interface region, to which we restrict our investigation. The Hamiltonian $\mathcal{H}$ of the Mn_2Au-Py comprises four terms:

$$\mathcal{H} = \mathcal{H}_{Mn_2Au} + \mathcal{H}_{Py} + \mathcal{H}_{\text{int}} + \mathcal{H}_{\text{ext}}, \tag{4.68}$$

where the terms are in order: AFM contribution, FM contribution, interface exchange coupling term, Zeeman term. Individually, the terms are given by

$$\mathcal{H}_{Mn_2Au} = -\sum_{i<j} \left(S_i \mathbf{J}_{ij}^{Mn_2Au} S_j + S_i^z \tilde{\mathbf{J}}_{ij}^{Mn_2Au} S_j^z \right)$$

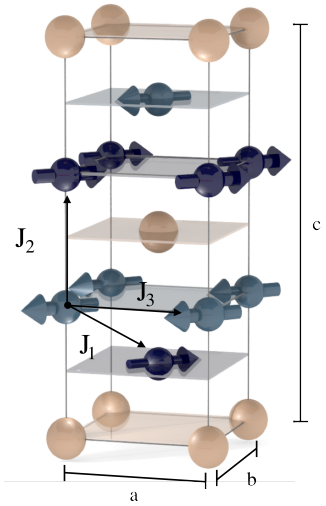

Figure 4.11: Exchange interactions in Mn_2Au up to the third nearest neighbor.

$$+ \sum_i \left(k_4^{\mathrm{Mn_2Au}} \, (S_i^z)^4 \, + \, k_\phi^{\mathrm{Mn2Au}} \, (S_i^x)^2 \, (S_i^y)^2 \right) \, + \, \mathcal{H}_d, \tag{4.69}$$

$$\mathcal{H}_{\mathrm{Py}} \, = \, - \sum_{i<j} S_i \, \mathbf{J}_{ij}^{\mathrm{Py}} \, S_j \, + \, \frac{k_c^{\mathrm{Py}}}{2} \, \sum_i \, (S_x^4 \, + \, S_y^4 \, + \, S_z^4) \, + \, \mathcal{H}_d, \tag{4.70}$$

$$\mathcal{H}_{\mathrm{int}} \, = \, - \sum_{i<j} S_i \, \mathbf{J}_{ij}^{\mathrm{int}} \, S_j \, + \, \mathcal{H}_d, \tag{4.71}$$

$$\mathcal{H}_{\mathrm{ext}} \, = \, - \sum_i \mu_s \, S_i \cdot \mathbf{B}_{\mathrm{ext}}, \tag{4.72}$$

where S_i are unit vectors that describe the atomistic spins, $\mathbf{J}_{ij}^{\mathrm{Mn_2Au}}$ is the exchange interaction matrix, $\tilde{\mathbf{J}}_{ij}^{\mathrm{Mn_2Au}}$ is the two-ion anisotropy constant [71], $k_4 < 0$ is the AFM out-of-plane anisotropy constant and $k_\phi > 0$ is the AFM in-plane anisotropy constant. $\mathcal{H}_d$ is the magnetostatic field. The out-of-plane anisotropy dominates and pushes the spins into the easy-plane, while the in-plane anisotropy picks the symmetry-equivalent $< 110 >$ directions as easy-axes. We set the cutoff for the exchange interaction after the third nearest neighbor. As can be seen in Fig. 4.11, the first (coupling constant J_1, distance 2.180 Å) and second nearest neighbors (coupling constant J_2, distance 2.853 Å) are coupled ferromagnetically, while the third nearest neighbor (coupling constant J_3, distance 3.327 Å) is coupled antiferromagnetically. For the interface exchange coupling we consider a coupling constant of 0.31×10^{-20} J/link, which is 20% of the bulk value of the Mn_2Au exchange interaction, as proposed in Ref. [86, 88]. For all simulations the damping constants $\lambda_{\mathrm{Py}} = \lambda_{\mathrm{Mn2Au}} = 0.01$ were used, unless stated otherwise. Please refer to Tab. 4.2

for the parameters that were used for the simulation.
In the FM Hamiltonian $\mathbf{J}_{ij}^{\mathrm{Py}}$ is the FM exchange stiffness and k_c^{Py} is the FM cubic anisotropy constant. The interface exchange coupling constant is given by $\mathbf{J}_{ij}^{\mathrm{int}}$, and it couples directly the FM and adjacent AFM spins at the interface between the two layers. An external field $\mathbf{B}_{\mathrm{ext}}$ can be coupled to the system by using the Zeeman term $\mathcal{H}_{\mathrm{ext}}$ with the spin moment of the respective spin μ_s.
The equilibrium state of the coupled DW was simulated using a Monte-Carlo integrator for one million time steps at zero temperature. Fig. 4.12 (a) shows the height averaged magnetic order parameter along x of this simulation in comparison to pure Mn_2Au. This means that we averaged the FM magnetization and the AFM Néel vector along the stacking axis of the hybrid and denoted this effective order parameter as $\mathbf{n}$. The profile of this order parameter is fitted with Eqn. (4.66). From the fit we determine a 30% increase of the DW width in Mn_2Au: 29.3 nm for pure Mn_2Au, 38.2 nm in Mn_2Au-Py.
This shows that the z dependence of the effective anisotropy in the coupled system cannot be neglected. Throughout the stacking axis of the hybrid the relative influences of the AFM and FM anisotropies vary. Consequently, the DW width varies as a function of z. In the limiting cases, the DW width at the top of the FM layer approaches the value for pure Py, while at the bottom of the AFM layer the value for pure Mn_2Au can be found. Due to the boundary condition of strong interface exchange coupling at the interface, a continuous variation of the DW width takes place along the z axis, such that the DW width connects smoothly at the interface. Such a smooth profile was obtained from atomistic spin dynamics simulations for varying FM layer thickness and is shown in Fig. 4.12 (b). We observe that the DW in Mn_2Au is narrower than in Py, as was expected from Eqns. 4.66, 4.67. Furthermore, the thicker the FM layer is, the stronger is the variation of the DW width. For a thin FM layer the coupled system is dominated by the AFM. However, as the two layers approach equal thickness, the effective anisotropy for the coupled system is equally influenced by both the FM and the AFM anisotropy, such that the interface exchange coupling strongly modifies the DW width.

We will use a magnetic field, that couples strongly to the FM part of the coupled DW, to set the DW into motion. We will see, that while the FM is set into motion, the interface exchange coupling will lead to coupled DW motion throughout the hybrid system.
The role of heating is a very important, albeit complicated, aspect of magnetization

Table 4.2: Model parameters for Mn_2Au used in the simulations. Isotropic exchange parameters are taken from Khmelevskyi et al. [145] and magnetic anisotropies are taken from Shick et al. [138]. The magnetic moment of the Mn sites is taken from experimental measurements of Barthem et al. [137].

Interaction	J_{xx}	J_{yy}	J_{zz}	Unit
$\mathbf{J}_1^{Mn_2Au}$	-1.094296	-1.094296	-1.086911	10^{-20} J (per link)
$\mathbf{J}_2^{Mn_2Au}$	-1.469234	-1.469234	-1.459319	10^{-20} J (per link)
$\mathbf{J}_3^{Mn_2Au}$	0.318261	0.318261	0.318261	10^{-20} J (per link)
$\tilde{\mathbf{J}}_1^{Mn_2Au}$	0.0	0.0	0.007385	10^{-20} J (per link)
$\tilde{\mathbf{J}}_2^{Mn_2Au}$	0.0	0.0	0.009915	10^{-20} J (per link)
$\tilde{\mathbf{J}}_3^{Mn_2Au}$	0.0	0.0	0.318261	10^{-20} J (per link)
$\tilde{\mathbf{J}}^{Py}$	0.009915	0.009915	0.009915	10^{-20} J (per link)
$\tilde{\mathbf{J}}^{int}$	0.318261	0.318261	0.318261	10^{-20} J (per link)
	Parameter	Value		Unit
	a, b	3.327		Å
	c	8.539		Å
	μ_{Mn}	4.0		μ_{B}
	μ_{Py}	1.6		μ_{B}
	$k_4^{Mn_2Au}$	-1.60218×10^{-24}		J/atom
	$k_\phi^{Mn_2Au}$	8.00109×10^{-25}		J/atom
	k_c^{Py}	1.0×10^{-26}		J/atom
	λ_{Mn_2Au}	0.01		–
	λ_{Py}	0.01		–

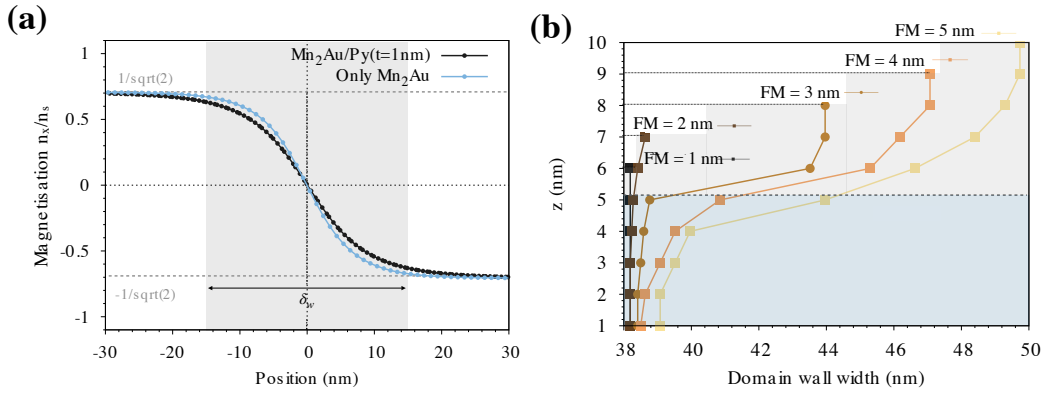

Figure 4.12: (a) DW profiles for n_x of a Mn_2Au-Py (1 nm) (5 nm) and a pure Mn_2Au (5 nm) system. The DW width δ_w increases for the bilayer system. (b) DW width variation along the stacking axis of the hybrid.

dynamics in Mn_2Au, and consequently Mn_2Au-Py. Experiments have shown that both NSOTs and thermomagnetoelastic effects can not be excluded from contributing to Néel vector switching in Mn_2Au [134]. Because of its high Néel temperature, the Néel state of Mn_2Au is regarded as very temperature stable. But because the interface exchange coupling observed in experiments is very strong [86, 88], we can neglect other interface effects. Suturin et al. discovered thermally driven short range fluctuations in nanometre spatial ranges in FMs [154]. We study the magnon spectra in our model system, but the role of thermal effects remains inconclusive. In order to still give a first indication on the influences thermal fluctuations could have on our results, we included simulations with different damping in the following (cf. Figs. 4.13, 4.14). The maximum DW velocity is not affected by the damping and the dynamics converge in the limit of strong driving fields. Our results hold qualitatively. Further studies of the role of heating unfortunately remain out of scope of this work and would require a dedicated study in order to clearly discern the contributions from thermomagnetoelastic and NSOT effects.

We consider a system of lateral dimensions 1000 nm along x and 40 nm along y. Furthermore, the Py layer is 1 nm and the Mn_2Au layer is 5 nm thick. We start from a relaxed 90° DW from the [110] direction to the [1$\bar{1}$0] direction, centered at $x = 100$ nm. We apply a magnetic field along the [110] direction to the hybrid system, such that the domain on one side of the DW becomes energetically favorable. Coupling of a magnetic field to the FM is much more efficient than to the AFM, as the FM possesses a large net magnetization. Hence, energetically, one FM domain is preferred and grows. This sets the FM DW into motion. Due to the strong

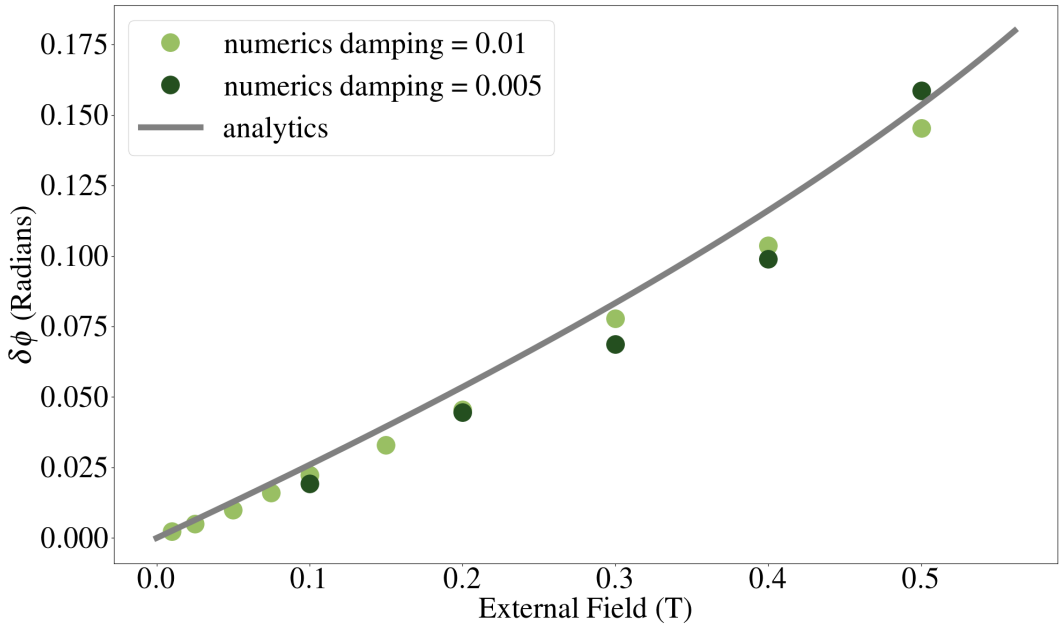

Figure 4.13: Shift of the equilibrium orientation of the order parameter under an applied field. Atomistic spin dynamics simulations and the analytical calculation agree.

interface exchange coupling, the FM DW drags the AFM DW with it, resulting in coupled DW motion.

But an applied field does not only cause DW motion. Additionally, it shifts the equilibrium orientation of the effective order parameter of the bilayer, as we have seen in Fig. 4.2 in Sec. 4.1. The shifted value of the order parameter in the $[1\bar{1}0]$ domain becomes $n_x = -1/\sqrt{2} + \delta n_x$ and $\delta n_x = 1/\sqrt{2} - \cos(\delta\phi - \pi/2)$. In order to obtain an analytical expression for the relation between the shift in the magnetic in-plane angle ϕ and the applied field $\mathbf{B}_{\text{ext}}$, we differentiate the energy functional Eqn. (4.1) once with respect to ϕ, and equalize the result with zero. In this way we can track the position of the extremal points of the energy spectrum. The resulting expression is

$$B = \frac{c_\phi\, k_\phi}{c_B\, \mu_{\text{Py}}} \frac{\sin(4\,\phi)}{\sin\left(\phi - \frac{\pi}{4}\right)}. \tag{4.73}$$

Thus, we can calculate our analytical expression for the shift $\delta\phi$ as a function of the applied field $\mathbf{B}_{\text{ext}}$ as

$$\mathbf{B}_{\text{ext}}\left(\delta\phi\right) \;=\; 4\,g\,\frac{\sin\left(4\left(\delta\phi \;-\; \frac{\pi}{2}\right)\right)}{\cos\left(\left(\delta\phi \;-\; \frac{\pi}{2}\right) \;+\; \frac{\pi}{4}\right)}. \tag{4.74}$$

In Fig. 4.13 we show the shift $\delta\phi$ versus the applied field both from our analytical calculation and from the atomistic spin dynamics simulations. For the analytical model we used the model parameters from Sec. 4.1: $k_{\phi}^{\text{Mn}_2\text{Au}} \;=\; 8.001\,09 \times 10^{-25}$ J/atom [138], $\mu_{\text{Py}} \;=\; 1.6\,\mu_B$, $E_0 \;\approx\; -34.1264 \cdot 10^{-21}$ J/atom, $c_{\phi} \;\approx\; 0.8375$ and $c_B \;\approx\; 0.2603$. The simulation data and the analytical calculations fit. This is in agreement with our calculations in Sec. 4.1, where the magnetic field induced a shift $\delta\phi$ in the position of the energy minimum for the domain oriented approximately perpendicular to the applied field.

In Fig. 4.14 we show the DW velocity, measured for the averaged order parameter, as a function of the applied field strength. The velocity is calculated for steady DW motion after an initial stabilization period. Previously, we have calculated the critical switching field, for which the AFM Néel vector and the FM magnetization reorient parallel to the applied field, cf. Sec. 4.1. The critical switching field acts as the limit for the maximum DW velocity, as it causes the system to become mono domain and the DW vanishes. The AFM magnetic moments pin the FM magnetic moments at the interface. As a result the applied field strengths required in order to set the DW into motion in the bilayer are higher compared to the pure Py case. We have fitted the data using Eqn. (3) from Ref. [155] with a velocity of $c \;\approx\; 8.5\,\text{km}\,\text{s}^{-1}$. As expected, the DW velocity increases with greater applied field. We observe the maximum velocity threshold in Fig. 4.14 at $B_c \;=\; 0.7555\,\text{T}$ with a maximum DW velocity of around $8.5\,\text{km}\,\text{s}^{-1}$, independent from the damping that was used for the simulation.

4.5 Conclusion

In this chapter we investigated the coupled magnetization dynamics in Mn_2Au-Py. In contrast to the previous chapter, Chap. 3, not the FM magnetization texture was imprinted onto the AFM, but rather the AFM domain structure dominated the hybrid system. In the static regime we used a phenomenological model to show the imprinting of the AFM domain texture onto the FM magnetization, as had been previously shown in the experiment [86]. By applying a magnetic field we showed that the effective magnetic field that is needed to reorient the AFM Néel vector in the Mn_2Au-Py system is lower than for pure Mn_2Au. The critical switching field

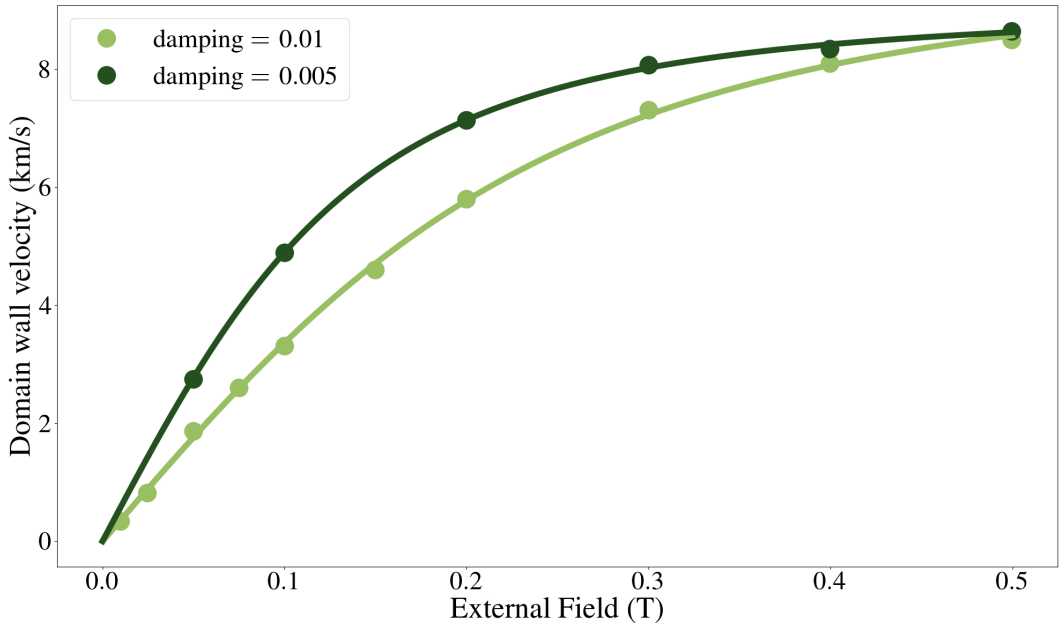

Figure 4.14: Stabilized DW velocity vs. external field.

amounted to $B_c = 0.7555\,\mathrm{T}$. This results was verified using atomistic spin dynamics simulations. Then we progressed into the dynamic regime by analyzing both the uniform magnetization dynamics and coupled DW motion. We conducted our study of the uniform magnetization dynamics in Mn_2Au-Py in cooperation with our collaborators Hassan Al-Hamdo and Prof. Dr. Mathias Weiler. We found that interface exchange coupling facilitates the control of the hybrid mode resonance frequencies and spin wave dispersion through the FM layer thickness. The unperturbed Py resonance splits into two non-degenerate modes with a strong enhancement of the frequencies in the hybrid system. As the cause we attributed the coupling of the Py dynamics to the in-plane and out-of-plane modes of the easy-plane AFM Mn_2Au. Our phenomenological model fits well to the observed vector network analyser-FMR (VNA-FMR data). It revealed that the magnitude of the frequency enhancement depends on the strength of the interface exchange coupling and on the AFM magnon frequencies. Furthermore, we were able to use our model to independently estimate the interface exchange coupling strength to $\xi J_{\mathrm{exch}} M_{\mathrm{FM}} = 1.6\,\mathrm{T\,nm}$ and with it the AFM magnon frequencies, which were within a factor of 2 of the literature values [152]. Our study showed that we can exploit THz AFM dynamics to control sub-THz hybrid spin dynamics. In Sec. 4.4 we concentrated on coupled DW motion in Mn_2Au-Py. The DW motion can be driven by magnetic fields acting predominantly on the FM. Due to the strong in-

terface exchange coupling, the FM drags the AFM with it. We find a limiting DW velocity of $8.5\,\mathrm{km\,s^{-1}}$. Our results fulfill the requirement of controlled Néel vector manipulation in order to enable AFM-based high-density information storage and efficient computing techniques.

Summary and Outlook

During the time research for this thesis began, the first experimental observations of interface exchange coupling of unprecedented strength emerged in Mn_2Au-Py [86]. A further novelty of these findings was the absence of exchange bias, that usually accompanies interface exchange coupling in AFM-FM hybrid systems. These findings opened up new avenues for controlling and reading out the AFM state in the hybrid system, which are essential for the application of AFMs as active components in novel computing devices. In this thesis we investigated the influences of interface exchange coupling on the magnetic ground state and its excitations in the dynamic regime of AFM-FM hybrid systems.

In Chapter 3 we demonstrated the stabilization of topological vortex textures in the in-plane AFM NiO(111) through interface exchange coupling to the FM Fe(110) at zero external magnetic fields. First, the vortex state naturally appears in the FM layer through magnetostatic interactions that depend on the boundaries of the grown nanostructures. Then, interface exchange coupling is responsible for overcoming the AFM anisotropy. In its isolated state, the Néel vector of NiO(111) lies in-plane. Through interface exchange coupling to the FM with the vortex in place, the FM vortex texture imprints onto the AFM Néel vector texture, such that the spatial distribution of the Néel vector is inhomogeneous and, at the vortex core, fully out-of-plane.
In a multiscale approach we use an analytical model, which was derived from phenomenological considerations in the macrospin approximation, and micromagnetic simulations. Our analytical calculations revealed that interface exchange coupling between the AFM and the FM layers causes the Néel vector to align with the FM magnetization at the vortex center. These results indicate the exciting pos-

sibility of inducing localized out-of-(111)-plane AFM moments in the well-known in-plane AFM NiO(111) system.
Furthermore, we demonstrated using micromagnetic simulations that the stability of the imprinted vortex states in the AFM can be tuned by the AFM layer thickness. While interface exchange coupling is the driving force behind the imprinting, the AFM anisotropy can be effectively varied through the AFM layer thickness, which is experimentally accessible. We constructed a phase diagram that takes into account the interplay between interface exchange coupling and the AFM layer thickness. The phase diagram remained consistent regardless of the number of imprinted vortices.
We proceeded with an analysis of the minimum requirements for an imprinting of the vortex state and its size dependence on the system's parameters. We found that the minimal interface exchange coupling strength required to transition into the stable AFM vortex state phase increases with AFM layer thickness. Specifically, for an AFM layer thickness of 4 nm, as studied in our experiments, we calculated the minimum critical interface exchange coupling $J_{\mathrm{coup}} \gtrsim 6 \times 10^{-4}\,\mathrm{J\,m^{-2}}$. Moreover, depending on the AFM layer thickness and interface exchange coupling strength we predict possible significant differences between the AFM and FM vortex core sizes. We found good agreement of our theoretical results with the experimental measurements of our collaborators.
In our models we neglected magnetoelastic effects, which are known to play a role in the magnetization dynamics of NiO [156]. The implementation of the magnetoelastic interaction into our model would be a viable extension in the future. The logical next step would be to investigate the dynamics of the imprinted vortex state. Such a study would pave the way towards more applications-based research for computational devices. It was recently shown that magnetic skyrmions can be used as the basic units of computation [157, 158]. In this context not only vortices, but also DWs and skyrmions could be considered in NiO-Fe. Furthermore, the interaction between imprinted topological states would be of interest for the application in neuromorphic computing.

In Chapter 4 we investigated the coupled magnetization dynamics in Mn_2Au-Py. We used a multiscale approach involving phenomenological models and atomistic spin dynamics simulations. First, we considered the influence of interface exchange coupling in the AFM-FM hybrid system on the magnetic ground state. We used a phenomenological model to show the imprinting of the AFM domain texture onto the FM magnetization, as had been previously shown in the experi-

ment [86].
In its isolated form, the AFM Mn_2Au requires large magnetic fields to reorient its Néel vector. Through interface exchange coupling to Permalloy, which is very susceptible to magnetic fields, this critical switching field was found to be lower in the AFM-FM hybrid system, compared to the pure AFM. The critical switching field amounted to $B_c = 0.7555\,\mathrm{T}$. We also used atomistic spin dynamics simulations to show this result, and the results from both methods agree.
Then we progressed into the dynamic regime by analyzing both the magnon dynamics and coupled DW motion. We conducted our study of the uniform magnetization dynamics in Mn_2Au-Py in cooperation with our collaborators Hassan Al-Hamdo and Prof. Dr. Mathias Weiler. Our investigation was directed towards coupled magnon excitations. While pure Permalloy exhibits a standard FM magnon dispersion, Mn_2Au exhibits two non-degenerate magnon modes that stem from its in-plane and out-of-plane anisotropies. We found, using a phenomenological model, that interface exchange coupling facilitates a hybrid mode resonance and spin wave dispersion. The unperturbed Py resonance splits into two non-degenerate modes with a strong enhancement of the frequencies in the hybrid system. As the cause we attributed the coupling of the Py dynamics to the in-plane and out-of-plane modes of the easy-plane AFM Mn_2Au. We found that the frequency enhancement and splitting can be controlled by the experimentally accessible FM layer thickness. Our phenomenological model fits well to the observed VNA-FMR data. It revealed that the magnitude of the frequency enhancement depends on the strength of the interface exchange coupling and on the AFM magnon frequencies.
Furthermore, we were able to use our model to independently estimate the interface exchange coupling strength and with it the AFM magnon frequencies. Our study showed that we can exploit THz AFM dynamics to control sub-THz hybrid spin dynamics in an attempt to speed up computational devices. Simultaneously, AFM dynamics significantly influence the hybrid system's behavior through frequency splitting and enhancement. This meets a key requirement for the application of AFM-FM hybrid systems in neuromorphic computing.
We further concentrated on coupled DW motion in Mn_2Au-Py utilizing atomistic spin dynamics simulations and a phenomenological model. The DW motion can be driven by magnetic fields acting predominantly on the FM. Due to the strong interface exchange coupling, the FM drags the AFM with it. We find a limiting DW velocity of $8.5\,\mathrm{km\,s^{-1}}$. Our results fulfill the requirement of controlled Néel vector

manipulation in order to enable AFM-based high-density information storage and efficient computing techniques.
Although further understanding of the Mn_2Au-Py material system was gained through the research conducted in this thesis, many questions remain open and many interesting research directions are possible. For instance an ab-initio study on the strength of interface exchange coupling could shine light on its origin in the electronic system and, thereby, make it possible to identify further material candidates that exhibit equally strong coupling. In our phenomenological models we neglected magnetothermal effects on the coupled magnetization dynamics. It was recently shown experimentally, that in competition with Néel SOTs, thermo-magnetoelastic effects play a dominant role in the current-induced switching of Mn_2Au [134]. Such influences will also show up in the hybrid system and could be studied using atomistic spin dynamics simulations. Experimentally, DW motion in Mn_2Au-Py would provide an interesting opportunity for study.

In conclusion, we have shown that interface exchange coupling is key to coupled magnetization states and dynamics in AFM-FM hybrid systems and enables functionalities in line with the needs of novel computing devices.

A Appendix

A.1 Supplementary Material for Interface-Exchange Mediated Vortex Imprinting in NiO-Fe

A.1.1 Parameters of Insets in Fig. 3.4

In Fig. 3.4 we show visualizations of the imprinted AFM vortex state from micromagnetic simulations. The position of the insets is qualitative with respect to the axes of the plot. In Tab. A.1 we present the corresponding parameters that were used for each simulation.

Table A.1: Model parameters.

Picture Inset	K_{AFM} [10^5 J/m^3]	J_{coup} [10^{-4} J/m^2]	t_{AFM} [nm]
A	1.0	1.4	0.8
B	5.0	5.0	4.0
C	8.0	9.9	6.4
D	1.0	5.0	0.8
E	5.0	9.9	4.0
F	1.0	9.9	0.8

A.1.2 Mumax^3 Code

In the following we show Mumax^3 code that was used to first relax a vortex state in the FM, then to load the system's initial configuration with the FM in the vortex state and the AFM in-plane and finally to study the stability of the imprinted AFM vortex state under the variation of the AFM anisotropy and the interface exchange coupling. In all three code examples we use the version that imprints five vortices in each layer.

```
/*

Vortex State in FM

    Author: T. Wagner, adapted from V. K. Bharadwaj
    Date: 07.02.2023
    Description: Relax a five vortex state in a single layer FM
    using demagnetising fields.


*/

// System size
nx := 640
ny := 128
nz := 2

dx := 1e-9
dy := 1e-9
dz := 1e-9

lx := nx*dx
ly := ny*dy
lz := nz*dz

SetGridSize(nx,ny,nz)
SetCellSize(dx, dy, dz)
OpenBC = true

// Material Constants taken from paper https://aip.scitation.org/
    doi/10.1063/1.4867597
satmag := 5e6 // A/m
//satmag := 1.77e7 // A/m
Kz := 5e5
Ki := 0.0
// Ki := 19369.2

AnisU = vector(0,0,1)
Aex = 2.1e-11 // J/m
Ku1 = Kz
//Msat = satmag
Alpha = 0.01
Enabledemag = True

```

```
43
44 // Custrom Fields: Fourth order in-plane anisotropy
45 //Ki4 := Ki
46 //c1 := Constvector(1,0,0)
47 //c2 := Constvector(0,1,0)
48
49 //anisField := Add( Mul( Const(-0.25 * Ki4 / (satmag)), Mul(Mul(
      Mul(Dot(c1, m), Dot(c1, m)), Dot(c1, m)), c1) ), Mul( Const
      (-0.25 * Ki4 / (satmag)), Mul(Mul(Mul(Dot(c2, m), Dot(c2, m)),
      Dot(c2, m)), c2) ) )
50
51 //anisEdens := Dot(anisField, m)
52 //AddFieldTerm(anisField)
53 //AddEdensTerm(anisEdens)
54
55
56 // Custom Initial Magnetization Configuration three Vortex State
57 body := cuboid(lx, ly, lz)
58 angle := pi/4
59 s1 := sqrt(2*(ly/2)*(ly/2))
60
61 BodyCuboidFelayer     := cuboid(s1, s1,  1e-9).transl( 0,  0, -0.5
      e-9   )
62 BodyCentreCylinder    := cylinder(10e-9, 1e-9).transl( 0,  0, -0.5
      e-9   )
63 BodyCuboidNiO2layer   := cuboid(lx, ly,  1e-9).transl( 0,  0,  0.5
      e-9   )
64
65 BodyCuboidFelayerOnly := body.sub(BodyCuboidNiO2layer)
66
67 setgeom(BodyCuboidFelayerOnly)
68
69 // defregion(0, body)
70 defregion(1, BodyCuboidFelayer.rotz(angle).transl( -(4*lx/10)+(lx
      /10)+1e-9,  0, 0)  )
71 defregion(2, BodyCuboidFelayer.rotz(angle).transl( -(4*lx/10)-(lx
      /10)+1e-9, 0, 0)  )
72 defregion(3, BodyCuboidFelayer.rotz(angle).transl( -(4*lx/10)+1e
      -9,  ly/2-1e-9, 0)  )
73 defregion(4, BodyCuboidFelayer.rotz(angle).transl( -(4*lx/10)+1e
      -9, -ly/2+1e-9, 0)  )
74
75 defregion(5, BodyCuboidFelayer.rotz(angle).transl( -(2*lx/10)+(lx
      /10)+1e-9,  0, 0)  )
```

```
76 defregion(6, BodyCuboidFelayer.rotz(angle).transl( -(2*lx/10)+1e
       -9,  ly/2-1e-9, 0)  )
77 defregion(7, BodyCuboidFelayer.rotz(angle).transl( -(2*lx/10)+1e
       -9, -ly/2+1e-9, 0)  )
78
79 defregion(8, BodyCuboidFelayer.rotz(angle).transl( (lx/10)-1e-9,
       0, 0)  )
80 defregion(9, BodyCuboidFelayer.rotz(angle).transl( 0,  ly/2-1e-9,
       0)  )
81 defregion(10, BodyCuboidFelayer.rotz(angle).transl( 0, -ly/2+1e-9,
        0)  )
82
83 defregion(11, BodyCuboidFelayer.rotz(angle).transl( (2*lx/10)+(lx
       /10)-1e-9,  0, 0)  )
84 defregion(12, BodyCuboidFelayer.rotz(angle).transl( (2*lx/10)-1e
       -9,  ly/2-1e-9, 0)  )
85 defregion(13, BodyCuboidFelayer.rotz(angle).transl( (2*lx/10)-1e
       -9, -ly/2+1e-9, 0)  )
86
87 defregion(14, BodyCuboidFelayer.rotz(angle).transl( (4*lx/10)+(lx
       /10)-1e-9,  0, 0)  )
88 defregion(15, BodyCuboidFelayer.rotz(angle).transl( (4*lx/10)-1e
       -9,  ly/2-1e-9, 0)  )
89 defregion(16, BodyCuboidFelayer.rotz(angle).transl( (4*lx/10)-1e
       -9, -ly/2+1e-9, 0)  )
90
91 defregion(17, BodyCentreCylinder.transl(-(4*lx/10)+1e-9, 0, 0))
92 defregion(18, BodyCentreCylinder.transl(-(2*lx/10)+1e-9, 0, 0))
93 defregion(19, BodyCentreCylinder)
94 defregion(20, BodyCentreCylinder.transl((2*lx/10)-1e-9, 0, 0))
95 defregion(21, BodyCentreCylinder.transl((4*lx/10)-1e-9, 0, 0))
96 // defregion(6, BodyCuboidNiO2layer)
97
98
99 m.setRegion(1, uniform(0, 1, 0).Add(0.1, randomMag()) )  // Right
100 m.setRegion(2, uniform(0, -1, 0).Add(0.1, randomMag()) )  // Left
101 m.setRegion(3, uniform(-1, 0, 0).Add(0.1, randomMag()) )  // Top
102 m.setRegion(4, uniform(1,  0, 0).Add(0.1, randomMag()) )  //
       Bottom
103
104 m.setRegion(5, uniform(0, -1, 0).Add(0.1, randomMag()) )  // Right
105 m.setRegion(6, uniform(1,  0, 0).Add(0.1, randomMag()) )  // Top
106 m.setRegion(7, uniform(-1, 0, 0).Add(0.1, randomMag()) )  //
       Bottom
```

```
107
108 m.setRegion(8, uniform(0, 1, 0).Add(0.1, randomMag()) )  // Right
109 m.setRegion(9, uniform(-1,  0, 0).Add(0.1, randomMag()) )  // Top
110 m.setRegion(10, uniform(1, 0, 0).Add(0.1, randomMag()) )  //
    Bottom
111
112 m.setRegion(11, uniform(0, -1, 0).Add(0.1, randomMag()) )  //
    Right
113 m.setRegion(12, uniform(1,  0, 0).Add(0.1, randomMag()) )  // Top
114 m.setRegion(13, uniform(-1, 0, 0).Add(0.1, randomMag()) )  //
    Bottom
115
116 m.setRegion(14, uniform(0, 1, 0).Add(0.1, randomMag()) )  // Right
117 m.setRegion(15, uniform(-1,  0, 0).Add(0.1, randomMag()) )  // Top
118 m.setRegion(16, uniform(1, 0, 0).Add(0.1, randomMag()) )  //
    Bottom
119
120 m.setRegion(17, uniform(0, 0, 1).Add(0.1, randomMag()) )  //
    cylinder at the centre
121 m.setRegion(18, uniform(0, 0, -1).Add(0.1, randomMag()) )  //
    cylinder at the centre
122 m.setRegion(19, uniform(0, 0, 1).Add(0.1, randomMag()) )  //
    cylinder at the centre
123 m.setRegion(20, uniform(0, 0, -1).Add(0.1, randomMag()) )  //
    cylinder at the centre
124 m.setRegion(21, uniform(0, 0, 1).Add(0.1, randomMag()) )  //
    cylinder at the centre
125
126 // m.setRegion(6, uniform(0, 0, 0)                          )  //
    NiO2 layer
127
128 Msat.setRegion(1, satmag )
129 Msat.setRegion(2, satmag )
130 Msat.setRegion(3, satmag )
131 Msat.setRegion(4, satmag )
132 Msat.setRegion(5, satmag )
133 Msat.setRegion(6, satmag )
134 Msat.setRegion(7, satmag )
135 Msat.setRegion(8, satmag )
136 Msat.setRegion(9, satmag )
137 Msat.setRegion(10, satmag )
138 Msat.setRegion(11, satmag )
139 Msat.setRegion(12, satmag )
140 Msat.setRegion(13, satmag )
```

```
Msat.setRegion(14, satmag )
Msat.setRegion(15, satmag )
Msat.setRegion(16, satmag )
Msat.setRegion(17, satmag )
Msat.setRegion(18, satmag )
Msat.setRegion(19, satmag )
Msat.setRegion(20, satmag )
Msat.setRegion(21, satmag )
// Msat.setRegion(6, 0.0    )  // NiO2 layer

// Simulate

SaveAs(m, sprintf("micustomfivevortexKz%.2f Ki %.1f.ovf", Kz
    , Ki))

relax()
minimize()
tablesave()

SaveAs(m, sprintf("mfcustomfivevortexKz%.2f Ki %.1f.ovf", Kz
    , Ki))

print(Kz, Ki, Eexch, Eanis, Edemag, EZeeman, Etotal)
```

```
/*

Vortex State in AFM

    Author: T. Wagner, adapted from V. K. Bharadwaj
    Date: 07.02.2023
    Description: Map the FM five vortex state into the AFM layer.

*/

// System size
nx := 640
ny := 128
nz := 2

dx := 1e-9
dy := 1e-9
dz := 1e-9

lx := nx*dx
```

```
ly := ny*dy
lz := nz*dz

SetGridSize(nx,ny,nz)
SetCellSize(dx, dy, dz)
OpenBC = true

// Material Constants taken from paper https://aip.scitation.org/doi/10.1063/1.4867597

satmag := 5e6 // A/m
Kz := -5e5
Ki := 0.0
AexIntra := 2.1e-11 // J/m

AnisU = vector(0,0,1)
Aex = AexIntra // J/m
Ku1 = Kz
Msat = satmag
Alpha = 0.01
Enabledemag = False

// Custrom Fields: Fourth order in-plane anisotropy
Ki4 := Ki
// c1 := Constvector(1,0,0)
// c2 := Constvector(0,1,0)

// anisField := Add( Mul( Const(-0.25 * Ki4 / (satmag)), Mul(Mul(Mul(Dot(c1, m), Dot(c1, m)), Dot(c1, m)), c1) ), Mul( Const(-0.25 * Ki4 / (satmag)), Mul(Mul(Mul(Dot(c2, m), Dot(c2, m)), Dot(c2, m)), c2) ) )

// anisEdens := Dot(anisField, m)
// AddFieldTerm(anisField)
// AddEdensTerm(anisEdens)

BodyCuboidNiO2layer   := cuboid(lx, ly,  1e-9).transl( 0,  0,  0.5e-9   )

defregion(6, BodyCuboidNiO2layer)

m.loadfile("initialcustomfivevortex1.out/mfcustomfivevortexKz-500000.00Ki10000.0.ovf")
//m.setRegion(6, randommag()                          )  // NiO2
```

```
   layer
m.setRegion(6, uniform(1,  0, 0).Add(0.1, randomMag())
               )  // NiO2 layer

// define a region for every layer, needed for interlayer exchange
    coupling
for i:=0; i¡nz; i++-
    defRegion(i, layer(i))

save(regions)

AexInter := 2.1e-2
scale := (AexInter * dz) / (2 * AexIntra)
for j:=0; j¡nz-1; j++-
    extscaleExchange(j, j+1, scale)


frozenspins.setregion(0, 1)

// Simulate

SaveAs(m, sprintf("mifefivevortexNirandKz%.2fKi%.1
   fJinter%.2f.ovf", Kz, Ki, AexInter))

print(Kz, Ki, AexInter, Eexch, Eanis, Edemag, EZeeman, Etotal
   )

relax()
minimize()
tablesave()

SaveAs(m, sprintf("mffefivevortexNirandKz%.2fKi%.1
   fJinter%.2f.ovf", Kz, Ki, AexInter))
```

```
/*

Vortex State in FM

    Author: T. Wagner, adapted from: V. K. Bharadwaj
    Date: 07.02.2023
    Description: Study stability of five vortex state mapping in
   AFM layer from five vortex state in FM layer.


```

```
*/

// System size
//nx := 640
//ny := 128
//nz := 2

//dx := 1e-9
//dy := 1e-9
//dz := 1e-9

nx := 1280
ny := 256
nz := 4

dx := 0.5e-9
dy := 0.5e-9
dz := 0.5e-9

lx := nx*dx
ly := ny*dy
lz := nz*dz

SetGridSize(nx,ny,nz)
SetCellSize(dx, dy, dz)
OpenBC = true

// Material Constants taken from paper https://aip.scitation.org/doi/10.1063/1.4867597

satmag := 5e6 // A/m
AexIntra := 2.1e-11 // J/m
Aex = AexIntra // J/m
Msat = satmag
Alpha = 0.01
Enabledemag = False

BodyCuboidNiO2layer   := cuboid(lx, ly,  1e-9).transl( 0,  0,  0.5e-9   )
defregion(6, BodyCuboidNiO2layer)    // NiO2 layer

// define a region for every layer, needed for interlayer exchange coupling

```

```
//for i:=0; i¡nz; i++-
//    defRegion(i, layer(i))
//

defRegion(0, layer(0).add(layer(1)))
defRegion(1, layer(2).add(layer(3)))

save(regions)


//KzMin   := 1e5
//KzMax   := 8e5
//Kzstep  := 0.5e5

KzMin   := 6e5
KzMax   := 6e5
Kzstep  := 0.5e5

for K1:=Kzmin; K1¡=Kzmax; K1+=Kzstep-

    // Setting the anisotropy parameter and direction

    Kz := K1
    Ku1 = -Kz
    AnisU = vector(0,0,1)

    Keff := K1 - (0.5*MU0*satmag*satmag)
    Ki := 0.0

    //RKKYmin   := 0.9e-4
    //RKKYmax   := 12e-4
    //RKKYstep  := 1e-5

    RKKYmin   := 6e-4
    RKKYmax   := 6e-4
    RKKYstep  := 1e-5

    for RKKY1:=RKKYmin; RKKY1¡=RKKYmax; RKKY1+=RKKYstep-

        m.loadfile("initialcustomfivevortex2smallcs.out/
    miFefivevortexNirandKz-500000.00Ki0.0Jinter0.02.ovf
    ")

        AexInter := RKKY1
```

```
93        scale := (AexInter * dz) / (2 * AexIntra)
94        //for j:=0; j¡nz-1; j++-
95        //    extscaleExchange(j, j+1, scale)
96        //
97        for j:=0; j¡2; j++-
98            extscaleExchange(j, j+1, scale)
99
100
101       frozenspins.setregion(0, 1)
102       //m.setregion(1, uniform(-1,  0, 0).Add(0.1, randomMag()))
103       //m.setregion(1, randomMag())
104       SaveAs(m, sprintf("miFevortexNiuniXKz%.dKi%.1
    fJinter%.6f.ovf", Kz, Ki, AexInter))
105
106       relax()
107       minimize()
108
109       SaveAs(m, sprintf("mfFevortexNiuniXKz%.dKi%.1
    fJinter%.6f.ovf", Kz, Ki, AexInter))
110
111
112       print(Kz, Ki, AexInter, Eexch, Eanis, Edemag, EZeeman,
     Etotal)
113
114
115
```

A.1.3 Original Data for Fig. 3.9

In Fig. 3.9 the data was transformed such that a linear fit function could be used. In Fig. A.1 we show the original, untransformed data.

A.2 Supplementary Material for Interface-Exchange Coupling of Spin Dynamics in Mn_2Au-Py

A.2.1 VAMPIRE Input Code for Mn_2Au

We atomistically simulated the magnetic ground state of Mn_2Au using the following input code for VAMPIRE.

```
1 #--------------------------------------------------
2 # System dimensions
3 #--------------------------------------------------
```

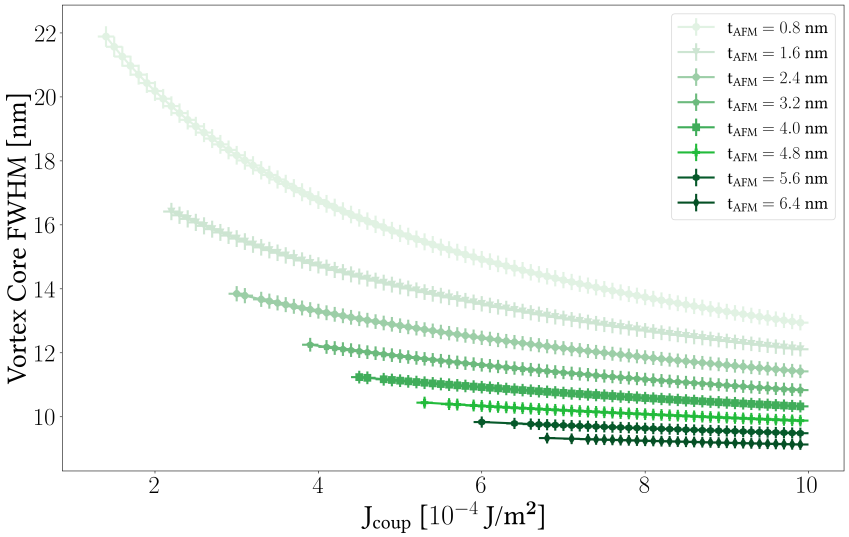

Figure A.1: Scaling of the vortex core size with the interface coupling strength for different AFM layer thicknesses.

```

dimensions:system-size-x=5 !nm
dimensions:system-size-y=5 !nm
dimensions:system-size-z=5 !nm
#dimensions:unit-cell-size=2.866 !A

#-----------------------------------------------------
# Material files
#-----------------------------------------------------

material:file=Mn2Au.mat
material:unit-cell-file=Mn2Au.ucf

#-----------------------------------------------------
# Simulation attributes
#-----------------------------------------------------

sim:time-step=1.0E-16
sim:time-steps-increment=1000
sim:cooling-time=0.1!ns
sim:cooling-function=linear
sim:total-time-steps=1000000
sim:minimum-temperature=0
sim:maximum-temperature=1000


```

```
anisotropy:enable-bulk-neel-anisotropy
anisotropy:surface-anisotropy-threshold=20
anisotropy:surface-anisotropy-nearest-neighbour-range=0.4!nm

sim:program=field-cool
sim:integrator=llg-heun

#-------------------------------------------------
# Data output
#-------------------------------------------------

output:real-time
output:temperature
output:material-magnetization
output:mean-magnetisation-length
output:magnetization
```

```
#=================================================
# Sample vampire material file V3+
#=================================================


#-------------------------------------------------
# Number of Materials
#-------------------------------------------------

material:num-materials=3

#-------------------------------------------------
# Material 1-3 IrMn
#-------------------------------------------------

material[1]:material-name="Mn"
material[1]:damping-constant=1.0
material[1]:atomic-spin-moment=3.79!muB
material[1]:material-element="C"
material[1]:density=1.00
material[1]:initial-spin-direction=random
material[1]:exchange-matrix[1]=6.67!mRyd
material[1]:exchange-matrix[2]=6.67!mRyd
material[1]:uniaxial-anisotropy-constant = -9e-24

material[2]:material-name="Mn"
material[2]:damping-constant=1.0
```

```
material[2]:atomic-spin-moment=3.79!muB
material[2]:material-element=”Mn”
material[2]:density=1.00
material[2]:initial-spin-direction=random
material[2]:exchange-matrix[1]=6.67!mRyd
material[2]:exchange-matrix[2]=6.67!mRyd
material[2]:uniaxial-anisotropy-constant = -9e-24

material[3]:material-name=”Au”
material[3]:non-magnetic
```

```
# Unit cell size:
3.54 3.54 3.54
# Unit cell vectors:
1.0 0.0 0.0
0.0 1.0 0.0
0.0 0.0 1.0
# Atoms num, id cx cy cz mat lc hc
1
0 0.5 0.5 0.5 0 1 2
# Interactions n exctype, id i j dx dy dz Jij
6 0
0 0 0 1 0 0 11.2e-21
1 0 0 -1 0 0 11.2e-21
2 0 0 0 1 0 11.2e-21
3 0 0 0 -1 0 11.2e-21
4 0 0 0 0 1 11.2e-21
5 0 0 0 0 -1 11.2e-21
```

A.2.2 Fitting Procedure of the Kittel Equation

We fit Eq. (4.30) to the experimentally determined resonance frequencies as a function of H_0 for each FM layer thickness with $k_{1\perp}$ and $k_{2\perp}$ as fitting parameters. For this we use the fitting formula

$$f^2 = p(1)\,x^2 + p(2)\,x + p(3). \tag{A.1}$$

This equation is related to the Kittel equation Eqn. (4.30) in the following way

$$\begin{aligned} f^2 &= \left(\frac{\gamma}{2\pi}\mu_0 H + \frac{\gamma}{2\pi}\frac{A_F}{M_M}k^2\right)\left(\frac{\gamma}{2\pi}\mu_0 H + \frac{\gamma}{2\pi}\frac{A_F}{M_M}k^2 + f_2\right) \\ &= \frac{\gamma}{2\pi}^2(\mu_0 H)^2 + \frac{\gamma}{2\pi}\mu_0 H\left(\frac{\gamma}{2\pi}\frac{A_F}{M_M}k^2 + \frac{\gamma}{2\pi}\frac{A_F}{M_M}k^2 + f_2\right) \end{aligned} \tag{A.2}$$

$$+ \frac{\gamma}{2\pi} \frac{A_F}{M_M} k^2 \left(\frac{\gamma}{2\pi} \frac{A_F}{M_M} k^2 + f_2 \right) \tag{A.3}$$

$$= f_H^2 + f_H (f_{F1} + f_{F2}) + f_{F1} f_{F2}. \tag{A.4}$$

We use $x := \mu_0 H$, $f_H := \frac{\gamma}{2\pi} \mu_0 H$, $f_{F1} := \frac{\gamma}{2\pi} \frac{A_F}{M_M} k^2$, $f_{F2} := \frac{\gamma}{2\pi} \frac{A_F}{M_M} k^2 + f_2$. Thus we can identify:

$$p(1) = \frac{\gamma^2}{(2\pi)^2} a \tag{A.5}$$

$$p(2) = \frac{\gamma}{(2\pi)} (f_{F1} + f_{F2}) a \tag{A.6}$$

$$p(3) = f_{F1} f_{F2} a. \tag{A.7}$$

By dividing by the appropriate power of $\frac{\gamma}{2\pi}$ we can convert the fitting constants from GHz (the unit of the experimental data of f) into

$$p1 = a, \tag{A.8}$$

$$p2 = a (f_{F1} + f_{F2}), \tag{A.9}$$

$$p3 = a f_{F1} f_{F2}, \tag{A.10}$$

where a is an arbitrary scaling constant. Here, $p1$ is the dimensionless scaling constant that originates from the experiment, $p2$ has the unit Hz and $p3$ Hz^2. We combine the above relations for $p1$, $p2$, $p3$

$$f_{F1} = \frac{p2}{p1} - f_{F2}, \tag{A.11}$$

$$f_{F2,1/2} = \frac{p2 \pm \sqrt{p2^2 - 4 p3 p1}}{2p1}. \tag{A.12}$$

By division of $f_{F1}/(\gamma/(2\pi))$ we convert f_{F1} into Tesla. From the evaluation of the frequencies we can now determine the FM k vector

$$k_1 = \sqrt{\frac{M_M}{A_F} f_{F1}}. \tag{A.13}$$

By inserting this k vector into the transcendental equation

$$k\, t_F \tan(k\, t_F) \;=\; \frac{\frac{J_{int}\, M_N^2\, \xi^2}{A_A}\; \frac{\frac{M_M^2}{M_N^2}}{\frac{A_F}{A_A}}\; \frac{t_F}{\xi}\; \frac{\omega_{1A}}{c} \tanh(\frac{\omega_{1A}}{c}\, t_A)}{-\frac{\omega_{1A}}{c} \tanh(\frac{\omega_{1A}}{c}\, t_A) \;+\; \frac{J_{int}\, M_N^2\, \xi^2}{A_A}\; \frac{1}{\xi}}, \tag{A.14}$$

and solving for J_{int} we determine the thickness dependence of the interlayer coupling strength $J_{int}\, M_M$ in T. We determine the FM k vectors for each resonance frequency branch f_1 and f_2. From the boundary conditions and Eq. (4.30) we obtain the approximate expression in Eqn. (4.29). We determine $\xi J_{\mathrm{exch}} M_{\mathrm{FM}} \approx 1.6\,\mathrm{T\,nm}$.

B Other Information

B.1 Contributions

In this section we detail the contributions of the author to the projects presented in this work (names of collaborators removed for data privacy).

B.1.1 Revealing the ultra-fast domain wall motion in Mn_2Au through permalloy capping

- Simulation and numerical data evaluation by the author and -
- Phenomenological model and calculations by the author, supported by - and -
- Manuscript writing by the author, - and -, supported by -

B.1.2 Coupling of ferromagnetic and antiferromagnetic spin dynamics in Mn_2Au/NiFe thin-film bilayers

- Phenomenological model and calculations by the author, supported by -
- Manuscript writing by the author and -, supported by - and -

B.1.3 Imprinting of Antiferromagnetic Vortex States in NiO-Fe Nanostructures

- Simulation and numerical data evaluation by the author, supported by -
- Phenomenological model and calculations by the author, supported by -

- Manuscript writing by the author and -, supported by - and - with input from the co-authors

B.2 List of Publications

- S. Jenkins, T. Wagner, O. Gomonay, K. Everschor-Sitte, "Revealing the ultrafast domain wall motion in Mn_2Au through permalloy capping", Phys. Rev. B **109**, 224431 - Published 27 June 2024, https://doi.org/10.1103/PhysRevB.109.224431.

- H. Al-Hamdo, T. Wagner, Y. Lytvynenko, G. Kendzo, S. Reimers, M. Ruhwedel, M. Yaqoob, V. I. Vasyuchka, P. Pirro, J. Sinova, M. Kläui, M. Jourdan, O. Gomonay, M. Weiler, "Coupling of ferromagnetic and antiferromagnetic spin dynamics in Mn_2Au/NiFe thin-film bilayers", Phys. Rev. Lett. **131**, 046701 - Published 24 July 2023, https://doi.org/10.1103/PhysRevLett.131.046701.

- M. Ślezak, T. Wagner, V. K. Bharadwaj, O. Gomonay, A. Kozioł-Rachwał, T. O. Mentes, A. Locatelli, M. Zajac, D. Wilgocka-Ślezak, P. Drózdz, T. Ślezak, "From Magnetostatics to Topology: Antiferromagnetic Vortex States in NiO-Fe Nanostructures", *Adv. Mater. Interfaces* 2024, 11, 2400309. https://doi.org/10.1002/admi.202400309.

Bibliography

[1] History Hit, "The legacy of hal 9000: How science fiction depictions of ai have changed over time," (last accessed 2024-07-09).

[2] Harvard Kenneth C. Griffin Graduate School of Arts and Sciences, "The history of artificial intelligence," (last accessed 2024-07-09).

[3] BBVA Foundation, "'2001' and artificial intelligence: reflections from marvin minsky, frontiers laureate in 2014," (last accessed 2024-07-09).

[4] D. M. Burton, *The History of Mathematics*, 7th ed. (Mc Graw Hill, 2011).

[5] World Economic Forum, "How to manage ai's energy demand - today, tomorrow and in the future," (last accessed 2024-06-18).

[6] A. Kurenkov, S. Fukami, and H. Ohno, "Neuromorphic computing with antiferromagnetic spintronics," J. Appl. Phys. **128**, 010902 (2020).

[7] S. Zhu, T. Yu, T. Xu, H. Chen, S. Dustdar, S. Gigan, D. Gunduz, E. Hossain, Y. Jin, F. Lin, B. Liu, Z. Wan, J. Zhang, Z. Zhao, W. Zhu, Z. Chen, T. S. Durrani, H. Wang, J. Wu, T. Zhang, and Y. Pan, "Intelligent Computing: The Latest Advances, Challenges, and Future," Intell. Comput. **2** (2023), 10.34133/icomputing.0006, arXiv:2211.11281 .

[8] Forbes, "Chatgpt and generative ai innovations are creating sustainability havoc," (last accessed 2024-06-18).

[9] EE Times Europe, "How quantum computing can help make ai greener," (last accessed 2024-06-18).

[10] N. Thompson, K. Greenewald, K. Lee, and G. F. Manso, "The Computational Limits of Deep Learning," in *Arxiv Prepr.* (LIMITS, 2023) arXiv:2007.05558 .

[11] A. Mehonic and A. J. Kenyon, "Brain-inspired computing needs a master plan," Nature **604**, 255–260 (2022), arXiv:2104.14517 .

[12] J. von Neumann, "First draft of a report on the edvac," IEEE Annals of the History of Computing **15**, 27–75 (1993).

[13] J. Backus, "Can programming be liberated from the von neumann style? a functional style and its algebra of programs," Commun. ACM **21**, 613–641 (1978).

[14] S. O. Valenzuela, P Gambardella, K. Garello, O. Klein, J. F. Sierra, and J. Sinova, "Spintronic materials," in *Encycl. Condens. Matter Phys.* (Elsevier, 2024) 2nd ed., pp. 159–176.

[15] M. N. Baibich, J. M. Broto, A. Fert, F. Nguyen Van Dau, F. Petroff, P. Etienne, G. Creuzet, A. Friederich, and J. Chazelas, "Giant Magnetoresistance of (001)Fe/(001)Cr Magnetic Superlattices," Phys. Rev. Lett. **61**, 2472–2475 (1988), /dx.doi.org/10.1103/PhysRevLett.61.2472 .

[16] G. Binasch, P. Grünberg, F. Saurenbach, and W. Zinn, "Enhanced magnetoresistance in layered magnetic structures with antiferromagnetic interlayer exchange," Phys. Rev. B **39**, 4828–4830 (1989).

[17] A. Fert, "Nobel Lecture: Origin, development, and future of spintronics," Rev. Mod. Phys. **80**, 1517–1530 (2008).

[18] P. A. Grünberg, "Nobel Lecture: From spin waves to giant magnetoresistance and beyond," Rev. Mod. Phys. **80**, 1531–1540 (2008).

[19] G.. Brumfiel, "The physics prize inside the iPod," Nature (2007), 10.1038/449643a.

[20] S. S. P. Parkin, N. More, and K. P. Roche, "Oscillations in Exchange Coupling and Magnetoresistance in Metallic Superlattice Structures," Phys. Rev. Lett. **23**, 130 (2014).

[21] S. S. P. Parkin, R. Bhadra, and K. P. Roche, "Oscillatory magnetic exchange coupling through thin copper layers," Phys. Rev. Lett. **66**, 2152–2155 (1991).

[22] S. S. P. Parkin, X. Jiang, C. Kaiser, A. Panchula, K. Roche, and M. Samant, "Magnetically engineered spintronic sensors and memory," Proc. IEEE **91**, 661–679 (2003).

[23] S. Mao, Y. Chen, F. Liu, X. Chen, B. Xu, P. Lu, M. Patwari, H. Xi, C. Chang, B. Miller, D. Menard, B. Pant, J. Loven, K. Duxstad, S. Li, Z. Zhang, A. Johnston, R. Lamberton, M. Gubbins, T. McLaughlin, J. Gadbois, J. Ding, B. Cross, S. Xue, and P. Ryan, "Commercial tmr heads for hard disk drives: characterization and extendibility at 300 gbit2," IEEE Transactions on Magnetics **42**, 97–102 (2006).

[24] M. Julliere, "Tunneling between ferromagnetic films," Phys. Lett. A **54**, 225–226 (1975).

[25] J. S. Moodera, L. R. Kinder, T. M. Wong, and R. Meservey, "Large magnetoresistance at room temperature in ferromagnetic thin film tunnel junctions," Phys. Rev. Lett. **74**, 3273–3276 (1995).

[26] T. Miyazaki and N. Tezuka, "Giant magnetic tunneling effect in Fe/Al2O3/Fe junction," J. Magn. Magn. Mater. **139**, L231–L234 (1995).

[27] C. Zheng, K. Zhu, S. Cardoso de Freitas, J. Chang, J. E. Davies, P. Eames, P. P. Freitas, O. Kazakova, C. Kim, C. Leung, S. Liou, A. Ognev, S. N. Piramanayagam, P. Ripka, A. Samardak, K. Shin, S. Tong, M. Tung, S. X. Wang, S. Xue, X. Yin, and P. W. T. Pong, "Magnetoresistive sensor development roadmap (non-recording applications)," IEEE Transactions on Magnetics **55**, 1–30 (2019).

[28] J. Puebla, J. Kim, K. Kondou, and Y. Otani, "Spintronic devices for energy-efficient data storage and energy harvesting," Commun. Mater. **1**, 24 (2020).

[29] J.C. Slonczewski, "Current-driven excitation of magnetic multilayers," J. Magn. Magn. Mater. **159**, L1–L7 (1996), arXiv:1601.07392v2 .

[30] Nature Portfolio, "Spintronics enters the mainstream," (last accessed 2024-06-18).

[31] S. S. P. Parkin and S. Yang, "Memory on the racetrack," Nat. Nanotechnol. **10**, 195–198 (2015).

[32] A. Soumyanarayanan, N. Reyren, A. Fert, and C. Panagopoulos, "Emergent phenomena induced by spin–orbit coupling at surfaces and interfaces," Nature **539**, 509–517 (2016), arXiv:1611.09521 .

[33] A. Fert, N. Reyren, and V. Cros, "Magnetic skyrmions: advances in physics and potential applications," Nat. Rev. Mater. **2**, 17031 (2017), arXiv:1712.07236 .

[34] E. Y. Vedmedenko, R. K. Kawakami, Denis D. Sheka, P. Gambardella, A. Kirilyuk, A. Hirohata, C. Binek, O. Chubykalo-Fesenko, S. Sanvito, B. J. Kirby, J. Grollier, Karin Everschor-Sitte, T. Kampfrath, C. Y. You, and A. Berger, "The 2020 magnetism roadmap," J. Phys. D. Appl. Phys. **53** (2020), 10.1088/1361-6463/ab9d98.

[35] J. Nogués and I. K. Schuller, "Exchange bias," J. Magn. Magn. Mater. **192**, 203–232 (1999).

[36] O. Gomonay, V. Baltz, A. Brataas, and Y. Tserkovnyak, "Antiferromagnetic spin textures and dynamics," Nat. Phys. **14**, 213–216 (2018).

[37] T. Jungwirth, X. Marti, P. Wadley, and J. Wunderlich, "Antiferromagnetic spintronics," Nat. Nanotechnol. **11**, 231–241 (2016), arXiv:1606.04284 .

[38] S. Selzer, "Simulations on the Dynamics of Complex Magnetic Nanostructures," PhD Thesis (2021).

[39] M. Beg, "Skyrmionic states in confined helimagnetic nanostructures," PhD Thesis (2016).

[40] S. J. Blundell, *Magnetism in condensed matter (Oxford Master Series in Physics)*, 1st ed. (Oxford University Press, 2001).

[41] D. J. Griffiths, *Introduction to Electrodynamics*, 4th ed. (Addison-Wesley, 2012).

[42] N. Bohr, "I. On the constitution of atoms and molecules," London, Edinburgh, Dublin Philos. Mag. J. Sci. **26**, 1–25 (1913).

[43] S. J. Barnett, "Magnetization by Rotation," Phys. Rev. **6**, 239–270 (1915).

[44] O. W. Richardson, "A Mechanical Effect Accompanying Magnetization," Phys. Rev. (Series I) **26**, 248–253 (1908).

[45] A. Einstein, "Experimenteller Nachweis der Ampereschen Molekularstroeme," Naturwissenschaften **3**, 237–238 (1915).

[46] A Einstein and W. J. de Haas, "Experimental proof of the existence of Ampère's molecular currents," K. Akad. van Wet. te Amsterdam, Proc. **18**, 696–711 (1915).

[47] W. Gerlach and O. Stern, "Das magnetische Moment des Silberatoms," Zeitschrift fuer Phys. **9**, 353–355 (1922).

[48] D. Go, D. Jo, H. Lee, M. Kläui, and Y.y Mokrousov, "Orbitronics: Orbital currents in solids," EPL (Europhysics Lett. **135**, 37001 (2021), arXiv:2107.08478 .

[49] W. Pauli, "Über den Einfluß der Geschwindigkeitsabhängigkeit der Elektronenmasse auf den Zeemaneffekt," Zeitschrift für Phys. **31**, 373–385 (1925).

[50] W. Heisenberg, "Zur Theorie des Ferromagnetismus," Zeitschrift fuer Phys. **49**, 619–636 (1928).

[51] E. C. Stoner, "Collective electron ferronmagnetism," Proc. R. Soc. London. Ser. A. Math. Phys. Sci. **165**, 372–414 (1938).

[52] P. Curie, "Biographical," (last accessed 2024-05-24).

[53] R. Skomski, "5 Finite-temperature magnetism," in *Simple Models of Magnetism* (Oxford University Press, 2008) https://academic.oup.com/book/0/chapter/142601448/chapter-ag-pdf/48030614/book_2390_section_142601448.ag.pdf .

[54] T Moriya, "Itinerant Electron Magnetism," Annu. Rev. Mater. Res. **14**, 1–25 (1984).

[55] J. M. Santiago, C-L Huang, and E. Morosan, "Itinerant magnetic metals," J. Phys. Condens. Matter **29**, 373002 (2017).

[56] O. Gomonay and V. M. Loktev, "Spintronics of antiferromagnetic systems," Low Temp. Phys. **40**, 17–35 (2014).

[57] A.M. Kosevich, B.A. Ivanov, and A.S. Kovalev, "Magnetic Solitons," Phys. Rep. **194**, 117–238 (1990), 0308464 .

[58] C. Kittel, "Theory of Antiferromagnetic Resonance," Phys. Rev. **82**, 565 (1951).

[59] L. Šmejkal, J. Sinova, and T. Jungwirth, "Emerging Research Landscape of Altermagnetism," Phys. Rev. X **12**, 040501 (2022), arXiv:2204.10844 .

[60] J Krempaský, L Šmejkal, S. W. D'Souza, M Hajlaoui, G Springholz, K Uhlířová, F Alarab, P C Constantinou, V. Strocov, D Usanov, W R Pudelko, R González-Hernández, A. Birk Hellenes, Z Jansa, H Reichlová, Z Šobáň, R. D. Gonzalez Betancourt, P Wadley, J. Sinova, D Kriegner, J Minár, J H Dil, and T Jungwirth, "Altermagnetic lifting of Kramers spin degeneracy," Nature **626**, 517–522 (2024), arXiv:2308.10681 .

[61] O. Eriksson, A. Bergman, L. Bergqvist, and J. Hellsvik, *Atomistic Spin Dynamics: Foundations and Applications* (Oxford University Press, 2017) p. 272 pp.

[62] U. Atxitia, D. Hinzke, and U. Nowak, "Fundamentals and applications of the Landau–Lifshitz–Bloch equation," J. Phys. D. Appl. Phys. **50**, 033003 (2017).

[63] M. D. Kuz'min, "Shape of temperature dependence of spontaneous magnetization of ferromagnets: Quantitative analysis," Phys. Rev. Lett. **94**, 16–19 (2005).

[64] R. F.L. Evans, U. Atxitia, and R. W. Chantrell, "Quantitative simulation of temperature-dependent magnetization dynamics and equilibrium properties of elemental ferromagnets," Phys. Rev. B - Condens. Matter Mater. Phys. **91**, 1–7 (2015), arXiv:1409.7397 .

[65] H. Kronmüller, "General Micromagnetic Theory and Applications," in *Mater. Sci. Technol.* (Wiley, 2019) pp. 1–43.

[66] L. Landau and E. Lifshitz, "On the theory of the dispersion of magnetic permeability in ferromagnetic bodies," Phys. Z. Sowjetunion **8**, 153–169 (1935).

[67] F. Bloch, "Nuclear Induction," Phys. Rev. **70**, 460–474 (1946).

[68] W. Heisenberg, "Mehrkörperproblem und Resonanz in der Quantenmechanik," Zeitschrift für Phys. **38**, 411–426 (1926).

[69] I Dzyaloshinskii, "A thermodynamic theory of "weak" ferromagnetism of antiferromagnetics," J. Phys. Chem. Solids **4**, 241–255 (1958).

[70] T. Moriya, "Anisotropic Superexchange Interaction and Weak Ferromagnetism," Phys. Rev. **120**, 91–98 (1960).

[71] R. F. L. Evans, L. Rózsa, S. Jenkins, and U. Atxitia, "Temperature scaling of two-ion anisotropy in pure and mixed anisotropy systems," Phys. Rev. B **102**, 020412 (2020), arXiv:2002.02548 .

[72] H.B. Callen and E. Callen, "The present status of the temperature dependence of magnetocrystalline anisotropy, and the power law," J. Phys. Chem. Solids **27**, 1271–1285 (1966).

[73] U. Nowak, "Classical spin models," in *Handbook of Magnetism and Advanced Magnetic Materials* (John Wiley & Sons, Ltd, 2007) https://onlinelibrary.wiley.com/doi/pdf/10.1002/9780470022184.hmm205 .

[74] R. Kikuchi, "On the Minimum of Magnetization Reversal Time," J. Appl. Phys. **27**, 1352–1357 (1956).

[75] S. Iida, "The difference between gilbert's and landau-lifshitz's equations," J. Phys. Chem. Solids **24**, 625–630 (1963).

[76] T.L. Gilbert, *Formulation, Foundations and Applications of the phenomenological theory of ferromagnetism*, Ph.D. thesis (1956).

[77] T.L. Gilbert, "Classics in Magnetics A Phenomenological Theory of Damping in Ferromagnetic Materials," IEEE Trans. Magn. **40**, 3443–3449 (2004), arXiv:1011.1669v3 .

[78] W. F. Brown, "Thermal Fluctuations of a Single-Domain Particle," Phys. Rev. **130**, 1677–1686 (1963), arXiv:arXiv:1011.1669v3 .

[79] R. F.L. Evans, W. J. Fan, P. Chureemart, T. Ostler, M. O.A. Ellis, and R. W. Chantrell, "Atomistic spin model simulations of magnetic nanomaterials," J. Phys. Condens. Matter **26**, 103202 (2014), arXiv:1310.6143 .

[80] M. Sallermann, H. Jónsson, and S. Blügel, "Stability of Hopfions in Bulk Magnets with Competing Exchange Interactions," Phys. Rev. B **107**, 1–13 (2022), arXiv:2212.01320 .

[81] M. Greber, "Rendering by M. Greber," Rendering generously provided by M. Greber .

[82] C. Kittel, *Introduction to Solid State Physics*, 7th ed. (John Wiley and Sons, 1996).

[83] G. S. Abo, Y. K. Hong, J. Park, J. Lee, W. Lee, and B. C. Choi, "Definition of magnetic exchange length," IEEE Trans. Magn. **49**, 4937–4939 (2013).

[84] M.J. Donahue and D.G. Porter, "Exchange energy formulations for 3D micromagnetics," Phys. B Condens. Matter **343**, 177–183 (2004).

[85] M.J. Donahue and R.D. McMichael, "Exchange energy representations in computational micromagnetics," Phys. B Condens. Matter **233**, 272–278 (1997).

[86] S. P. Bommanaboyena, D. Backes, L. S.I. I. Veiga, S. S. Dhesi, Y. R. Niu, B. Sarpi, T. Denneulin, A. Kovács, T. Mashoff, O. Gomonay, J. Sinova, K. Everschor-Sitte, D. Schönke, R. M. Reeve, M. Kläui, H.-J. Elmers, and M. Jourdan, "Readout of an antiferromagnetic spintronics system by strong exchange coupling of Mn2Au and Permalloy," Nat. Commun. **12**, 6539 (2021), arXiv:2106.02333 .

[87] Sophie F. Weber, Andrea Urru, Sayantika Bhowal, Claude Ederer, and Nicola A. Spaldin, "Surface Magnetization in Antiferromagnets: Classification, Example Materials, and Relation to Magnetoelectric Responses," Phys. Rev. X **14**, 021033 (2024), arXiv:2306.06631 .

[88] H. Al-Hamdo, T. Wagner, Y. Lytvynenko, G. Kendzo, S. Reimers, M. Ruhwedel, M. Yaqoob, V. I. Vasyuchka, P. Pirro, J. Sinova, M. Kläui, M. Jourdan, O. Gomonay, and M. Weiler, "Coupling of Ferromagnetic and Antiferromagnetic Spin Dynamics in Mn_2Au/NiFe Thin Film Bilayers," Phys. Rev. Lett. **131**, 046701 (2023), arXiv:2302.07915 .

[89] A. Vansteenkiste, J. Leliaert, M. Dvornik, M. Helsen, F. Garcia-Sanchez, and B. Van Waeyenberge, "The design and verification of MuMax3," AIP Adv. **4**, 0–22 (2014), arXiv:1406.7635 .

[90] P. Nieves, U. Atxitia, R. W. Chantrell, and O. Chubykalo–Fesenko, "The classical two-sublattice Landau–Lifshitz–Bloch equation for all temperatures," Low Temp. Phys. **41**, 739–744 (2015).

[91] E. G. Tveten, T. Müller, J. Linder, and A. Brataas, "Intrinsic magnetization of antiferromagnetic textures," Phys. Rev. B **93**, 104408 (2016), arXiv:1506.06561 .

[92] Michał Ślęzak, Tobias Wagner, Venkata Krishna Bharadwaj, Olena Gomonay, Anna Kozioł-Rachwał, Tevfik Onur Menteş, Andrea Locatelli, Marcin Zając, Dorota Wilgocka-Ślęzak, Piotr Dróżdż, and Tomasz Ślęzak, "From Magnetostatics to Topology: Antiferromagnetic Vortex States in NiO-Fe Nanostructures," Adv. Mater. Interfaces **11**, 1–7 (2024), arXiv:2403.05151 .

[93] D. Marković, M. W. Daniels, P. Sethi, A. D. Kent, M. D. Stiles, and J. Grollier, "Easy-plane spin Hall nano-oscillators as spiking neurons for neuromorphic computing," Phys. Rev. B **105**, 014411 (2022), arXiv:2110.06737 .

[94] J. Torrejon, M. Riou, F. A. Araujo, S. Tsunegi, G. Khalsa, D. Querlioz, P. Bortolotti, V. Cros, K. Yakushiji, A. Fukushima, H. Kubota, S. Yuasa, M. D. Stiles, and J. Grollier, "Neuromorphic computing with nanoscale spintronic oscillators," Nature **547**, 428–431 (2017), arXiv:1701.07715 .

[95] K. Y. Guslienko, K. Lee, and S. Kim, "Dynamic Origin of Vortex Core Switching in Soft Magnetic Nanodots," Phys. Rev. Lett. **100**, 027203 (2008).

[96] D. Caso, P. Tuero, J. García, K. Y. Guslienko, and F. G. Aliev, "Dynamics and Reversible Control of the Bloch-Point Vortex Domain Wall in Short Cylindrical Magnetic Nanowires," Phys. Rev. Appl. **19**, 064030 (2023).

[97] D. Betto and J. M. D. Coey, "Vortex state in ferromagnetic nanoparticles," J. Appl. Phys. **115** (2014), 10.1063/1.4867597.

[98] J. Sort, K. S. Buchanan, V. Novosad, A. Hoffmann, G. Salazar-Alvarez, A. Bollero, M. D. Baró, B. Dieny, and J. Nogués, "Imprinting vortices into antiferromagnets," Phys. Rev. Lett. **97**, 1–4 (2006).

[99] J. Stöhr, A. Scholl, T. J. Regan, S. Anders, J. Lüning, M. R. Scheinfein, H. A. Padmore, and R. L. White, "Images of the antiferromagnetic structure of a NiO(100) surface by means of X-ray magnetic linear dichroism spectromicroscopy," Phys. Rev. Lett. **83**, 1862–1865 (1999).

[100] G. van der Laan, E. Arenholz, R. V. Chopdekar, and Y. Suzuki, "Influence of crystal field on anisotropic x-ray magnetic linear dichroism at the Co^{2+} $L_{2,3}$ edges," Phys. Rev. B **77**, 064407 (2008).

[101] J. Wu, D. Carlton, J. S. Park, Y. Meng, E. Arenholz, A. Doran, A. T. Young, A. Scholl, C. Hwang, H. W. Zhao, J. Bokor, and Z. Q. Qiu, "Direct observation of imprinted antiferromagnetic vortex states in CoO/Fe/Ag(001) discs," Nat. Phys. **7**, 303–306 (2011).

[102] G. Salazar-Alvarez, J. J. Kavich, J. Sort, A. Mugarza, S. Stepanow, A. Potenza, H. Marchetto, S. S. Dhesi, V. Baltz, B. Dieny, A. Weber, L. J. Heyderman, J. Nogués, and P. Gambardella, "Direct evidence of imprinted vortex states in the antiferromagnet of exchange biased microdisks," Appl. Phys. Lett. **95** (2009), 10.1063/1.3168515.

[103] M. Ślezak, H. Nayyef, P. Dróżdż, W. Janus, A. Kozioł-Rachwał, M. Szpytma, M. Zając, T. O. Menteş, F. Genuzio, A. Locatelli, and T. Ślezak, "Controllable magnetic anisotropy and spin orientation of a prototypical easy-plane antiferromagnet on a ferromagnetic support," Phys. Rev. B **104**, 1–10 (2021).

[104] M. Ślezak, P. Drózdz, W. Janus, H. Nayyef, A. Kozioł-Rachwał, M. Szpytma, M. Zając, T. O. Menteş, F. Genuzio, A. Locatelli, and T. Ślezak, "Fine tuning of ferromagnet/antiferromagnet interface magnetic anisotropy for field-free switching of antiferromagnetic spins," Nanoscale **12**, 18091–18095 (2020).

[105] A. Kozioł-Rachwał, M. Ślęzak, M. Zając, P. Dróżdż, W. Janus, M. Szpytma, H. Nayyef, and T. Ślęzak, "Control of spin orientation in antiferromagnetic NiO by epitaxial strain and spin–flop coupling," APL Mater. **8** (2020), 10.1063/5.0011736.

[106] P. Wadley, B. Howells, J. Železný, C. Andrews, V. Hills, R. P. Campion, V. Novák, K. Olejník, F. Maccherozzi, S. S. Dhesi, S. Y. Martin, T. Wagner, J. Wunderlich, F. Freimuth, Y. Mokrousov, J. Kuneš, J. S. Chauhan, M. J. Grzybowski, A. W. Rushforth, Kw Edmond, B. L. Gallagher, and T. Jungwirth, "Electrical switching of an antiferromagnet," Science (80-.). **351**, 587–590 (2016), arXiv:1503.03765 .

[107] F. P. Chmiel, N. Waterfield Price, R. D. Johnson, A. D. Lamirand, J. Schad, G. van der Laan, D. T. Harris, J. Irwin, M. S. Rzchowski, C.-B. B. Eom, and P. G. Radaelli, "Observation of magnetic vortex pairs at room temperature

in a planar α-Fe2O3/Co heterostructure," Nat. Mater. **17**, 581–585 (2018), arXiv:1801.02560 .

[108] E. Folven, T. Tybell, A. Scholl, A. Young, S. T. Retterer, Y. Takamura, and J. K. Grepstad, "Antiferromagnetic domain reconfiguration in embedded LaFeO3 thin film nanostructures," Nano Lett. **10**, 4578–4583 (2010).

[109] E. Folven, J. Linder, O. Gomonay, A. Scholl, A. Doran, A. T. Young, S. T. Retterer, V. K. Malik, T. Tybell, Y. Takamura, and J. K. Grepstad, "Controlling the switching field in nanomagnets by means of domain-engineered antiferromagnets," Phys. Rev. B **92**, 094421 (2015), arXiv:1508.01520 .

[110] M. S. Lee, T. A. Wynn, E. Folven, R. V. Chopdekar, A. Scholl, A. T. Young, S. T. Retterer, J. K. Grepstad, and Y. Takamura, "Tailoring Spin Textures in Complex Oxide Micromagnets," ACS Nano **10**, 8545–8551 (2016).

[111] D. Sander, S. O. Valenzuela, D. Makarov, C. H. Marrows, E. E. Fullerton, P. Fischer, J. McCord, P. Vavassori, S. Mangin, P. Pirro, B. Hillebrands, A. D. Kent, T. Jungwirth, O. Gutfleisch, C. G. Kim, and A. Berger, "The 2017 Magnetism Roadmap," J. Phys. D. Appl. Phys. **50**, 363001 (2017).

[112] T. Jungwirth, J. Sinova, A. Manchon, X. Marti, J. Wunderlich, and C. Felser, "The multiple directions of antiferromagnetic spintronics," Nat. Phys. **14**, 200–203 (2018).

[113] E. Arenholz, G. Van Der Laan, R. V. Chopdekar, and Y. Suzuki, "Angle-dependent Ni2+ X-ray magnetic linear dichroism: Interfacial coupling revisited," Phys. Rev. Lett. **98**, 1–4 (2007).

[114] M. Finazzi, A. Brambilla, P. Biagioni, J. Graf, G. H. Gweon, A. Scholl, A. Lanzara, and L. Duò, "Interface coupling transition in a thin epitaxial antiferromagnetic film interacting with a ferromagnetic substrate," Phys. Rev. Lett. **97**, 1–4 (2006).

[115] A. D. Bang, I. Hallsteinsen, F. K. Olsen, S. D. Slöetjes, S. T. Retterer, A. Scholl, E. Arenholz, E. Folven, and J. K. Grepstad, "Néel vector reorientation in ferromagnetic/antiferromagnetic complex oxide nanostructures," Appl. Phys. Lett. **114** (2019), 10.1063/1.5094604.

[116] J. Wu, J. S. Park, W. Kim, E. Arenholz, M. Liberati, Andreas Scholl, Y. Z. Wu, C. Hwang, and Z. Q. Qiu, "Direct Measurement of Rotatable and Frozen

CoO Spins in Exchange Bias System of CoO/Fe/Ag(001)," Phys. Rev. Lett. **104**, 217204 (2010).

[117] W. Janus, T. Ślęzak, M. Ślęzak, M. Szpytma, P. Dróżdż, H. Nayyef, A. Mandziak, D. Wilgocka-Ślęzak, M. Zając, M. Jugovac, T. O. Menteş, A. Locatelli, and A. Kozioł-Rachwał, "Tunable magnetic anisotropy of antiferromagnetic NiO in (Fe)/NiO/MgO/Cr/MgO(001) epitaxial multilayers," Sci. Rep. **13**, 1–9 (2023).

[118] P. K. Arekapudi, S. S, B. Böhm, L. Ramasubramanian, F. Ganss, P. Heinig, S. Stienen, C. Fowley, K. Lenz, A. M. Deac, M. Albrecht, and O. Hellwig, "Direct imaging of distorted vortex structures and magnetic vortex annihilation processes in ferromagnetic/antiferromagnetic disk structures," Phys. Rev. B **103**, 14405 (2021).

[119] F. Nolting, A. Scholl, J. Stöhr, J W Seo, J Fompeyrine, H Siegwart, J.-P. Locquet, S Anders, J. Lüning, E. E. Fullerton, M. F. Toney, M. R. Scheinfein, and H. A. Padmore, "Direct observation of the alignment of ferromagnetic spins by antiferromagnetic spins," Nature **405**, 767–769 (2000).

[120] A. D. Bang, F. K. Olsen, S. D. Slöetjes, A. Scholl, S. T. Retterer, C. A.F. Vaz, T. Tybell, E. Folven, and J. K. Grepstad, "Magnetic domain formation in ultrathin complex oxide ferromagnetic/antiferromagnetic bilayers," Appl. Phys. Lett. **113** (2018), 10.1063/1.5047271.

[121] C. Schmitt, L. Baldrati, L. Sanchez-Tejerina, F. Schreiber, A. Ross, M. Filianina, S. Ding, F. Fuhrmann, R. Ramos, F. Maccherozzi, D. Backes, M.-A. Mawass, F. Kronast, S. Valencia, E. Saitoh, G. Finocchio, and M. Kläui, "Identification of Néel Vector Orientation in Antiferromagnetic Domains Switched by Currents in NiO/Pt Thin Films," Phys. Rev. Appl. **15**, 034047 (2021), arXiv:2008.08507 .

[122] L. Exl, S. Bance, F. Reichel, T. Schrefl, H. Peter Stimming, and N. J. Mauser, "LaBonte's method revisited: An effective steepest descent method for micromagnetic energy minimization," J. Appl. Phys. **115** (2014), 10.1063/1.4862839, arXiv:1309.5796 .

[123] M. D. Kuz'min, K P Skokov, L V B Diop, I A Radulov, and O Gutfleisch, "Exchange stiffness of ferromagnets," Eur. Phys. J. Plus **135**, 301 (2020).

[124] C. D. Graham, "Magnetocrystalline Anisotropy Constants of Iron at Room Temperature and Below," Phys. Rev. **112**, 1117–1120 (1958).

[125] Martin Münzenberg, "Rendering by Martin Münzenberg," Rendering generously provided by Martin Münzenberg .

[126] S. Jenkins, T. Wagner, O. Gomonay, and K. Everschor-Sitte, "Revealing ultrafast domain wall motion in Mn2Au through permalloy capping," Phys. Rev. B **109**, 224431 (2024).

[127] A. H. MacDonald and M. Tsoi, "Antiferromagnetic metal spintronics," Philos. Trans. R. Soc. A Math. Phys. Eng. Sci. **369**, 3098–3114 (2011), arXiv:0510797 [cond-mat] .

[128] M. Wang, J. Zhou, X. Xu, T. Zhang, Z. Zhu, Z. Guo, Y. Deng, M. Yang, K. Meng, B. He, J. Li, G. Yu, T. Zhu, A. Li, X. Han, and Y. Jiang, "Field-free spin-orbit torque switching via out-of-plane spin-polarization induced by an antiferromagnetic insulator/heavy metal interface," Nat. Commun. **14**, 2871 (2023).

[129] S. Yu. Bodnar, L. Šmejkal, I. Turek, T. Jungwirth, O. Gomonay, J. Sinova, A. A. Sapozhnik, H.-J. Elmers, M. Kläui, and M. Jourdan, "Writing and reading antiferromagnetic Mn2Au by Néel spin-orbit torques and large anisotropic magnetoresistance," Nat. Commun. **9**, 348 (2018), arXiv:1706.02482 .

[130] K. Olejník, T. Seifert, Z. Kašpar, V. Novák, P. Wadley, R. P. Campion, M. Baumgartner, P. Gambardella, P. Němec, J. Wunderlich, J. Sinova, P. Kužel, M. Müller, T. Kampfrath, and T. Jungwirth, "Terahertz electrical writing speed in an antiferromagnetic memory," Sci. Adv. **4**, 1–8 (2018), arXiv:1711.08444 .

[131] T. Matalla-Wagner, M.-F. Rath, D. Graulich, J.-M. Schmalhorst, G. Reiss, and M. Meinert, "Electrical Néel-Order Switching in Magnetron-Sputtered CuMnAs Thin Films," Phys. Rev. Appl. **12**, 064003 (2019), arXiv:1903.12387 .

[132] P. Wadley, K. W. Edmonds, M. R. Shahedkhah, R. P. Campion, B. L. Gallagher, J. Železný, J. Kuneš, V. Novák, T. Jungwirth, V. Saidl, P. Němec, F. Maccherozzi, and S. S. Dhesi, "Control of antiferromagnetic spin axis orientation in bilayer Fe/CuMnAs films," Sci. Rep. **7**, 11147 (2017), arXiv:1702.03147 .

[133] S. Selzer, L. Salemi, A. Deák, E. Simon, L. Szunyogh, P. M. Oppeneer, and U. Nowak, "Current-induced switching of antiferromagnetic order in Mn2Au from first principles," Phys. Rev. B **105**, 1–8 (2022).

[134] S. Reimers, Y. Lytvynenko, Y. R. Niu, E. Golias, B. Sarpi, L. S. I. Veiga, T. Denneulin, A. Kovács, R. E. Dunin-Borkowski, J. Bläßer, M. Kläui, and M. Jourdan, "Current-driven writing process in antiferromagnetic Mn2Au for memory applications," Nat. Commun. **14**, 1861 (2023), arXiv:2208.04048 .

[135] Y. Behovits, A. L Chekhov, S. Yu Bodnar, O. Gueckstock, S. Reimers, Y. Lytvynenko, Y. Skourski, M. Wolf, T. S Seifert, O. Gomonay, M. Kläui, M. Jourdan, and T. Kampfrath, "Terahertz Néel spin-orbit torques drive nonlinear magnon dynamics in antiferromagnetic Mn2Au," Nat. Commun. **14**, 6038 (2023), arXiv:2305.03368 .

[136] G. Nahrwold, J. M. Scholtyssek, S. Motl-Ziegler, O. Albrecht, U. Merkt, and G. Meier, "Structural, magnetic, and transport properties of Permalloy for spintronic experiments," J. Appl. Phys. **108** (2010), 10.1063/1.3431384.

[137] V. M.T.S. Barthem, C. V. Colin, H. Mayaffre, M. H. Julien, and D. Givord, "Revealing the properties of Mn 2 Au for antiferromagnetic spintronics," Nat. Commun. **4**, 2892 (2013).

[138] A. B. Shick, S. Khmelevskyi, O. N. Mryasov, J. Wunderlich, and T. Jungwirth, "Spin-orbit coupling induced anisotropy effects in bimetallic antiferromagnets: A route towards antiferromagnetic spintronics," Phys. Rev. B **81**, 212409 (2010), arXiv:1002.2151 .

[139] P. Asselin, R. F. L. Evans, J. Barker, R. W. Chantrell, R. Yanes, O. Chubykalo-Fesenko, D. Hinzke, and U. Nowak, "Constrained Monte Carlo method and calculation of the temperature dependence of magnetic anisotropy," Phys. Rev. B **82**, 054415 (2010), arXiv:1006.3507 .

[140] J. Hirst, U. Atxitia, S. Ruta, J. Jackson, L. Petit, and T. Ostler, "Temperature-dependent micromagnetic model of the antiferromagnet Mn_2Au : A multiscale approach," Phys. Rev. B **106**, 094402 (2022).

[141] O. Gomonay, K. Yamamoto, and J. Sinova, "Spin caloric effects in antiferromagnets assisted by an external spin current," J. Phys. D. Appl. Phys. **51**, 264004 (2018), arXiv:1803.07949 .

[142] N. Smith, D. Markham, W. Doyle, and D. Latourette, "Magnetoresistive measurement of the exchange constant in varied thickness Permalloy films (abstract)," J. Appl. Phys. **63**, 2948 (1988).

[143] A. A. Sapozhnik, M. Filianina, S. Yu. Bodnar, A. Lamirand, M.-A. Mawass, Y. Skourski, H.-J. Elmers, H. Zabel, M. Kläui, and M. Jourdan, "Direct imaging of antiferromagnetic domains in Mn2Au manipulated by high magnetic fields," Phys. Rev. B **97**, 134429 (2018), arXiv:1803.03022 .

[144] A. A. Sapozhnik, C. Luo, H. Ryll, F. Radu, M. Jourdan, H. Zabel, and H.-J. Elmers, "Experimental determination of exchange constants in antiferromagnetic Mn2Au," Phys. Rev. B **97**, 184416 (2018), arXiv:1803.03524 .

[145] S. Khmelevskyi and P. Mohn, "Layered antiferromagnetism with high Neel temperature in the intermetallic compound Mn2Au," Appl. Phys. Lett. **93**, 1–4 (2008).

[146] M. Jourdan, H. Bräuning, A. Sapozhnik, H.-J. Elmers, H. Zabel, and M. Kläui, "Epitaxial Mn 2 Au thin films for antiferromagnetic spintronics," J. Phys. D. Appl. Phys. **48**, 385001 (2015).

[147] H. Maier-Flaig, S. T. B. Goennenwein, R. Ohshima, M. Shiraishi, R. Gross, H. Huebl, and M. Weiler, "Note: Derivative divide, a method for the analysis of broadband ferromagnetic resonance in the frequency domain," Rev. Sci. Instrum. **89** (2018), 10.1063/1.5045135, arXiv:1705.05694 .

[148] C. Kittel, "On the theory of ferromagnetic resonance absorption," Phys. Rev. **73**, 155–161 (1948).

[149] B. A. Kalinikos and A. N. Slavin, "Theory of dipole-exchange spin wave spectrum for ferromagnetic films with mixed exchange boundary conditions," J. Phys. C Solid State Phys. **19**, 7013–7033 (1986).

[150] Nguyen N. Phuoc and C.K. Ong, "Influence of ferromagnetic thickness on dynamic anisotropy in exchange-biased MnIr/FeCo multilayered thin films," Phys. B Condens. Matter **406**, 3514–3518 (2011).

[151] N. N. Phuoc, L. T. Hung, and C.K. Ong, "Ultra-high ferromagnetic resonance frequency in exchange-biased system," J. Alloys Compd. **506**, 504–507 (2010).

[152] M. Arana, F. Estrada, D. S. Maior, J. B. S. Mendes, L. E. Fernandez-Outon, W. A. A. Macedo, V. M. T. S. Barthem, D. Givord, A. Azevedo, and S. M. Rezende, "Observation of magnons in Mn 2 Au films by inelastic Brillouin and Raman light scattering," Appl. Phys. Lett. **111**, 192409 (2017).

[153] P. Yu, X. F. Jin, J. Kudrnovský, D. S. Wang, and P. Bruno, "Curie temperatures of fcc and bcc nickel and permalloy: Supercell and Green's function methods," Phys. Rev. B - Condens. Matter Mater. Phys. **77**, 1–8 (2008).

[154] S. M. Suturin, A. Philippi-Kobs, R. Carley, R. Gort, G. Grübel, E. Jal, M. V. Baidakova, E. Y. Lobanova, L. Mercadier, S. L. Molodtsov, L. Müller, D. V. Potorochin, M. Riepp, W. Roseker, A. Scherz, J. Schlappa, L. Le Guyader, G. Mercurio, M. Turcato, B. Van Kuiken, A. Yaroslavtsev, A. Y. Deviatov, Y. O. Kvashnin, A. I. Lichtenstein, V. V. Mazurenko, and I. I. Pronin, "Short nanometer range optically induced magnetic fluctuations accompanying ultrafast demagnetization of nanoscale ferromagnetic domains," Phys. Rev. B **108**, 174444 (2023).

[155] O. Gomonay, T. Jungwirth, and J. Sinova, "High Antiferromagnetic Domain Wall Velocity Induced by Néel Spin-Orbit Torques," Phys. Rev. Lett. **117**, 017202 (2016), arXiv:1602.06766 .

[156] H. Meer, F. Schreiber, C. Schmitt, R. Ramos, E. Saitoh, O. Gomonay, J. Sinova, L. Baldrati, and M. Kläui, "Direct Imaging of Current-Induced Antiferromagnetic Switching Revealing a Pure Thermomagnetoelastic Switching Mechanism in NiO," Nano Lett. **21**, 114–119 (2021), arXiv:2008.05219 .

[157] M. A. Brems, M. Kläui, and P. Virnau, "Circuits and excitations to enable Brownian token-based computing with skyrmions," Appl. Phys. Lett. **119** (2021), 10.1063/5.0063584, arXiv:2107.02097 .

[158] K. Raab, M. A. Brems, G. Beneke, T. Dohi, J. Rothörl, F. Kammerbauer, J. H. Mentink, and M. Kläui, "Brownian reservoir computing realized using geometrically confined skyrmion dynamics," Nat. Commun. **13**, 6982 (2022), arXiv:2203.14720 .

List of Figures

List of Tables